ISSN: 2764-5886
e-ISSN: 2764-622X

Volume 9· Nº 10 · October 2026

Journal of Bioengineering, Technologies and Health

An Official Publication of
SENAI CIMATEC

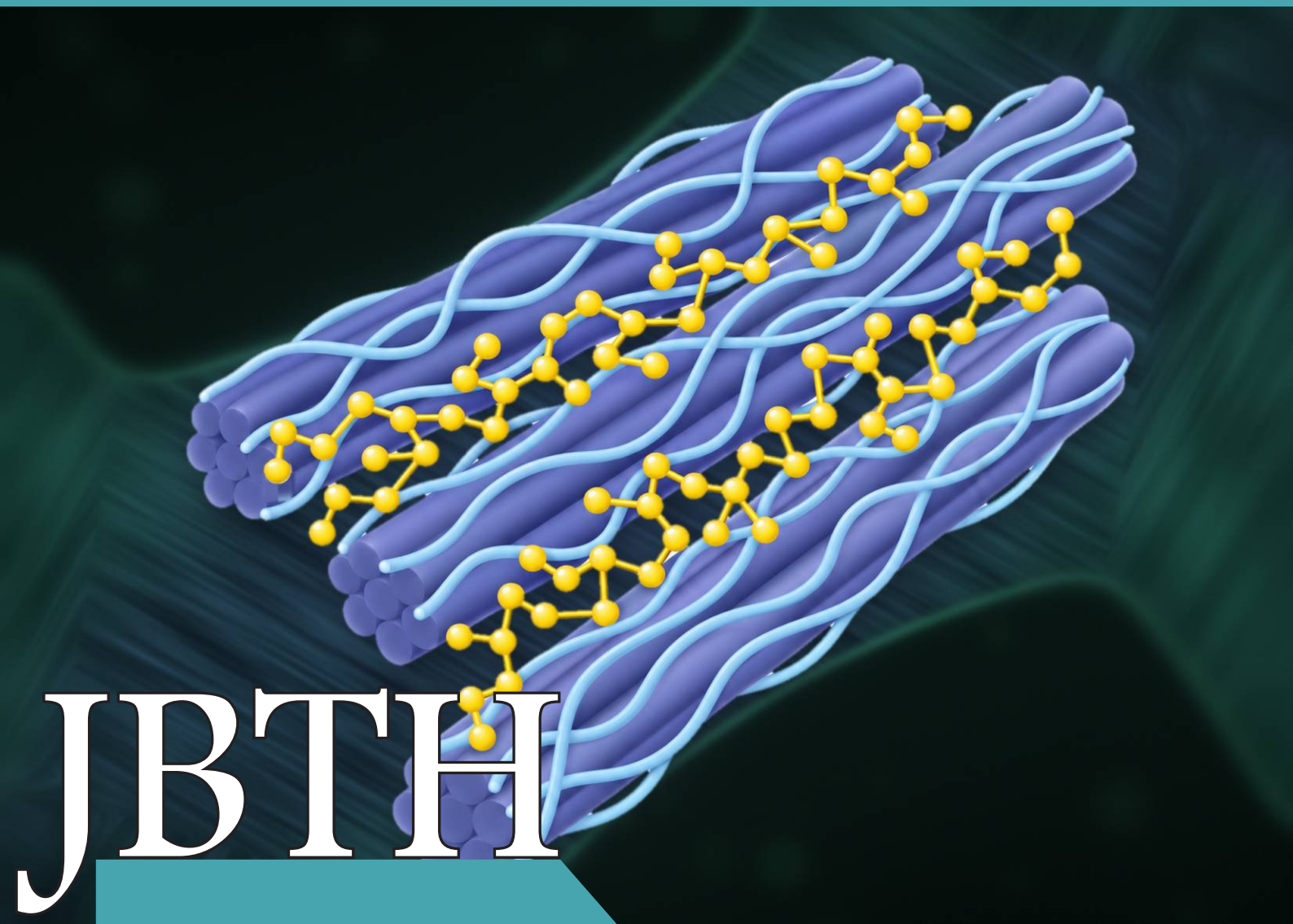

ISSN: 2764-5886 / e-ISSN 2764-622X

Volume 9 • Number 10 • October 2026

JOURNAL OF BIOENGINEERING TECHNOLOGIES AND HEALTH

An Official Publication of SENAI CIMATEC

EDITOR-IN-CHIEF
Alex Álisson Bandeira Santos

PUBLISHED BY SENAI CIMATEC

Sistema FIEB | SENAI CIMATEC
PELO FUTURO DA INOVAÇÃO

October 2026
Printed in Brazil

JOURNAL OF BIOENGINEERING TECHNOLOGIES AND HEALTH

An Official Publication of SENAI CIMATEC

EDITOR-IN-CHIEF

Alex Álisson Bandeira Santos

DEPUTY EDITOR

Roberto Badaró

ASSISTANT DEPUTY EDITORS

Josiane Dantas Viana Barbosa (BR)
Lilian Lefol Nani Guarieiro (BR)
Valéria Loureiro (BR)

ASSOCIATE EDITORS

Alan Grodzinsky (US)
Bruna Aparecida Souza Machado (BR)
Carlos Coimbra (US)
Eduardo Mario Dias (BR)
Frank Kirchner (DE)
Jorge Almeida Guimarães (BR)
Milena Soares (BR)
Preston Mason (US)
Sanjay Singh (US)
Steven Reed (US)
Valter Estevão Beal (BR)

STATISTICAL ASSOCIATE EDITOR

Valter de Senna (BR)

EDITORIAL BOARD

Carlos Augusto Grabois Gadelha (BR)
Durvanei Augusto Maria (BR)
Eliane de Oliveira Silva (BR)
Erick Giovani Sperandio Nascimento (BR)
Fernando Pellegrini Pessoa (BR)
Francisco Uchoa Passos (BR)
George Tynan (US)
George Tynan (US)
Gilson Soares Feitosa (BR)
Gisele Olímpio da Rocha (BR)
Hercules Pereira (BR)
Herman Augusto Lepikson (BR)
Hermano Krebs (US)
Idelfonso Bessa dos Reis Nogueira (NO)
Immanuel Lerner (IR)
Ingrid Winkler (BR)
James Chong (KR)
Jeancarlo Pereira dos Anjos (BR)
José Elias Matieli (BR)
Joyce Batista Azevedo (BR)
Larissa da Silva Paes Cardoso (BR)
Lusiada Portugal (PT)
Luzia Aparecida Tofaneli (BR)
Maria Lídia Rebello Pinho Dias (BR)
Mario de Seixas Rocha (BR)
Maximilian Serguei Mesquita (BR)
Regina de Jesus Santos (BR)
Renelson Ribeiro Sampaio (BR)
Roberto de Pinho (BR)
Rodrigo Santiago Coelho (BR)
Sanjay Mehta (US)
Vidal Augusto Zapparoli Castro Melo (BR)
Vilson Rosa de Almeida (BR)

PRODUCTION STAFF

Luciana Knop, Managing Editor

JOURNAL OF BIOENGINEERING TECHNOLOGIES AND HEALTH

Volume 9 • Number 10 **SUMMARY** *October 2026*

Original Articles

A Proposed Integration Framework for Underwater Robotic Simulation Using Gazebo and Unity3D 983
Anderson Lima, Herman Lepikson, Carlos Pereira

Degradation of Fluorophores in Hydraulic Fluids: Impacts on Fluorescence Intensity and Color Contrast for Underwater Leak Detection 990
Rafael Nascimento de Menezes, Rodrigo Dias Sarno, Bianca Kurihara Yoshii, Mariana Chagas Alcantara dos Santos, Lucas Cruz da Silva, Milena Ventura Castro Meira, Valéria Loureiro da Silva

Development and Validation of a Measurement System for Vehicle Infotainment Bluetooth Classic Performance 997
Milton Plinio Flores Porto, Helio Pio Correia Lima Junior, Thiago Barros Murari, Marcelo Albano Moret Simões Gonçalves

Evaluation of the Tensile Properties of LLDPE/Sisal Composites Produced by 3D Printing 1003
Ana Paula Gonçalves, Lucas Huriuchi, Mariana Souza, Vinícius Oliveira, Rodrigo Polkowski

Finite Element Analysis of a Polymeric Support with Metallic Internal Reinforcement for Carbon Steel Pipes ..1010
João Pedro Cheloni, Gabriel Aelo Ribeiro, Adriel da Anunciação Santana, Lucas Lincoln Fonseca Soares, Francisco Ferreira de Carvalho Júnior

Process Parameters Investigation of Lignin Content in Residual Biomass 1016
Davi Vieira Rosa, Diana Catalina Cubides Roman, Paulo Victor Rocha Brandao

Circular Innovation in Technical Education: A Design Thinking-Based Pedagogical Practice Using Reused Materials..... 1021
Clariane Teixeira Pessoa Mamona, Pietro Carlos Gonçalves Conceição

Overview of Physical Channel Modeling in CV-QKD Systems 1026
Davi Juvêncio Gomes de Sousa, Nelson Alves Ferreira Neto

Overview on Hardware Adaptation for Continuous-Variable Quantum Key Distribution Systems: Opportunities with RISC-V Architectures ... 1033
Glenda Barbosa do Nascimento, Linton Thiago Costa Esteves, Wagner Luiz Alves de Oliveira, Valeria Loureiro da Silva, Nelson Alves Ferreira Neto

Simulating the BB84 QKD Protocol: A QuTiP-Based Study in Ideal Quantum Channels ... 1040
Henrique Sobrinho Ghizoni, Anderson R. C. Buarque

Systematic Review

Biomethane Insertion in the Piped Natural Gas Network in the State of Bahia – Brazil 1047
Paulo Roberto dos Santos, Hugo Saba, Marcio L.V. Araújo

Instructions for Authors

Statement of Editorial Policy

Checklist for Submitted Manuscripts

The Journal of Bioengineering, Technologies and Health (JBTH) is an official publication of the SENAI CIMATEC University (Serviço Nacional de Aprendizagem Industrial - Universidade Centro Integrado de Manufatura e Tecnologia). It is published montly (January to December) in English by SENAI CIMATEC University – Avenida Orlando Gomes, 1845, Piatã, ZIP code: 41650-010, Salvador-Bahia-Brazil; phone: (55 71) 3879-5501. The editorial offices are at SENAI CIMATEC University.

Editorial Office

Correspondence concerning subscriptions, advertisements, claims for missing issues, changes of address, and communications to the editors should be addressed to the Deputy Editor, Dr. Roberto Badaró, SENAI CIMATEC University (Journal of Bioengineering, Technologies and Health – JBTH) – Avenida Orlando Gomes, 1845, Piatã, ZIP code: 41650-010, Salvador-Bahia-Brazil; phone: (55 71) 3879-5501; or sent by e-mail: jbth@fieb.org.br / jbth.cimatec@gmail.com.

Permissions

The permissions should be asked to the Ediot in Chief of the Journal of Bioengineering, Technologies and Health and SENAI CIMATEC University. All rights reserved. Except as authorized in the accompanying statement, no part of the JBTH may be reproduced in any form or by any electronic or mechanic means, including information storage and retrieval systems, without the publisher's written permission. Authorization to photocopy items for internal or personal use, or the internal or personal use by specific clients is granted by the Journal of Bioengineering, Technologies and Health and SENAI CIMATEC University for libraries and other users. This authorization does not extend to other kinds of copying such as copying for general distribution, for advertising or promotional purposes, for creating new collective works, or for resale.

Postmaster

Send address changes to JBTH, Avenida Orlando Gomes, 1845, Piatã, Zip Code: 41650-010, Salvador-Bahia-Brazil.

Information by JBTH-SENAI CIMATEC University
Address: Avenida Orlando Gomes, 1845, Piatã, ZIP code: 41650-010, Salvador-Bahia-Brazil
Home-page: www.jbth.com.br
E-mail: jbth@fieb.org.br / jbth.cimatec@gmail.com
Phone: (55 71) 3879-5501 / 3879-5500 / 3879-9500

DOI:10.34178

ISSN: 2764-5886 / e-ISSN 2764-622X

Copyright
© 2026 by Journal of Bioengineering, Technologies and Health
SENAI CIMATEC
All rights reserved.

COVER: Figure 1. Arrangement of cellulose, hemicellulose, and lignin in plant cell walls. "Process Parameters Investigation of Lignin Content in Residual Biomass" by Davi Vieira Rosa et al. J Bioeng. Tech. Health 2026;9(10):1016.

A Proposed Integration Framework for Underwater Robotic Simulation Using Gazebo and Unity3D

Anderson Lima[1,2]*, Herman Lepikson[1,2], Carlos Pereira[1]
[1]SENAI CIMATEC University, Robotics; [2]Federal University of Bahia, Program of Post Graduation in Mecathronic; Salvador, Bahia, Brazil

Simulation of robotic systems is a strategic approach for improving and developing new platforms, especially in underwater environments where access and testing conditions are limited. In early prototyping stages of unmanned underwater vehicles, conducting tests in real environments may not be convenient due to factors such as high costs, logistical difficulties, involved risks, and the need to save time and resources during design iterations. Using simulation tools makes it possible to test and validate a wide range of conditions and situations that a vehicle may encounter in its operation, including ocean currents, varying depths, obstacles, and different operation modes, requiring an accurate and realistic virtual representation of the underwater environment for effective development. Gazebo, integrated with ROS, is widely used in the robotics community for its high physical accuracy in modeling the dynamics, motion, and physical interactions of robotic systems within underwater environments. However, it provides limited visual realism and graphical fidelity for refined visual applications. On the other hand, Unity3D is a dedicated game engine that provides high-quality graphical rendering and realistic visual representations, ideal for immersive simulation and visual validation. Integrating Gazebo and Unity3D enables the creation of more realistic and reliable simulations that are useful for the design, development, and continuous improvement of robotic platforms. This research presents an approach on how to integrate Gazebo and Unity3D to achieve accurate pose correspondence of underwater robotic systems. The proposed approach uses ROS as middleware to enable communication and synchronization of data such as position and orientation, aiming for synchronized physical and visual simulations. This integration is envisioned to provide a flexible and scalable platform for developing and testing control and navigation algorithms in underwater robotic applications.
Keywords: Simulation. Underwater Robotics. ROS. Gazebo. Unity3D.
Abbreviations: ROS, Robot Operating System. URDF, Unified Robot Description Format.

The term simulation, meaning a test, experiment, or trial in which a situation or real-world conditions are artificially reproduced, emerges as a potential tool in the implementation of robotic systems, playing a role that can be significant in various stages of this process. Simulation has become a fundamental part of planning and executing specific tasks, such as accessing functionalities associated with hardware and testing algorithms related to localization, planning, navigation, and control of robotic systems. Moreover, it is not limited to testing the functioning of individual robots but also plays a role in the continuous integration and testing of complex robotic systems where multiple components must operate in harmony. Additionally, simulation enables the exploration of various scenarios and challenges that may be encountered in the real world, contributing to the development of more robust and effective algorithms. Conducting tests in the marine environment can present significant challenges involving difficulties, monotonous tasks, and, in some cases, potential risks. Furthermore, performing tests in real maritime environments can require additional efforts, significant time, and result in high costs. Thus, the development of applications and algorithms requires the availability of a reproducible and adequate virtual environment, with the main objective being to replicate the anticipated response to physical interactions. Simulation makes sense in these cases if it is accurate enough to allow the user to draw conclusions from the results. The effectiveness of simulators in robotics needs to be evaluated because, despite their widespread

Received on 16 April 2026; revised 22 September 2026.
Address for correspondence: Anderson Lima. Av. Orlando Gomes, 1845 - Piatã, Salvador – BA – Brazil, ZIP code: 41650-010. E-mail: anderson.lima@fieb.org.br.

J Bioeng. Tech. Health 2026;9(10):983-989
© 2026 by SENAI CIMATEC University. All rights reserved.

use, it is necessary to understand their limitations and performance to effectively use their results. Being aware of the degree of deviation from reality allows for reasonable interpretation of results, and evaluating the limitations and performance of simulators is a task strongly influenced by the configuration of the simulators and the physics engines integrated into them. Moreover, as some simulators are still under active development, the evaluation process becomes even more challenging. The integration of the Gazebo simulator with Unity3D will enable a more accurate and reliable representation of underwater robotic systems, resulting in more realistic and useful simulations for the development and improvement of these platforms. This collaboration between the two simulation platforms will lead to the creation of more realistic systems considering, for instance, the dynamic environment found in underwater robotic operations.

Motivation and Contributions

Conducting tests at sea poses significant technical challenges for direct observation, particularly in the case of autonomous underwater vehicles operating in their natural environment. Unlike most other mobile robots, these vehicles must function autonomously and without human intervention. This inherent inaccessibility greatly complicates the evaluation, diagnosis, and resolution of system failures. To ensure full reliability, both software and hardware must be thoroughly tested in laboratory conditions before deployment in real-world scenarios [1]. Environmental limitations and the substantial investment in time and resources required make the actual loss of a vehicle difficult to justify. Therefore, modeling and simulation play a crucial role in development, testing, and operator training. This approach enables cost-effective troubleshooting at both the component and system levels and facilitates more efficient mission planning [2]. In the field of autonomous underwater vehicles, computational modeling is essential for both design and control processes. As emphasized by Nahon [3], computational models provide designers with valuable tools to evaluate the inherent stability of a proposed vehicle prior to physical prototyping. This early-stage assessment helps reduce resource expenditure on physical prototypes and accelerates the development process. Beyond stability analysis, these models also support the development of controllers aimed at enhancing a vehicle's dynamic performance, underlining the importance of simulation not only for evaluation but also for active performance improvement of underwater robotic systems. However, the effectiveness of simulation results depends heavily on the accuracy of the vehicle model, especially when experimental data is limited. Nahon [3] outlines three key subtasks in the modeling process: deriving the mathematical equations that govern the vehicle's motion, determining the vehicle-specific hydrodynamic derivatives, and numerically solving the resulting system of equations using known control inputs. Within this comprehensive modeling framework, simulation emerges as a critical tool for predicting and optimizing underwater vehicles behavior. Stability concerns, controller optimization, and navigation through complex underwater environments can all be addressed more effectively through the careful integration of computational modeling and simulation. Simulating robotic systems in underwater environments is thus a foundational step in the prototyping of underwater vehicles. Early deployment of these platforms in real-world scenarios is often unfeasible, as they must operate independently, executing complex missions and responding to unexpected events such as system failures, obstacle avoidance, or battery depletion. Furthermore, AUVs must be robust and reliable, both electrically and mechanically, to perform effectively in such demanding conditions. Researchers have dedicated efforts to improving Unity3D's capability to simulate underwater conditions, incorporating aspects like buoyancy, drag, ocean currents, and other hydrodynamic effects. Tools such as URSim [4] and UWRoboticsSimulator [5] have been developed as open-source simulators to address

these needs. Despite these advancements, when comparing Unity3D-based solutions to Gazebo, it becomes evident that Gazebo inherently offers more comprehensive and precise hydrodynamic modeling. It particularly stands out in its representation of stability derivatives, which are vital for capturing how a vehicle reacts to complex forces and motions in fluid environments, including the effects of ocean currents. URSim and UWRoboticsSimulator implement simplified models for calculating forces like buoyancy and drag but lack explicit formulations for linear and quadratic stability derivatives. These derivatives are fundamental for accurately predicting how an object responds to forces from different directions under varying motion conditions. As a result, these Unity3D-based simulators have reduced accuracy in scenarios involving complex maneuvers or non-linear fluid-structure interactions, such as when ocean currents are present. In their comparative study, Platt and Ricks [6] point out key architectural differences between ROS-Gazebo and ROS-Unity3D. They observed that Unity3D generally demands more computational resources than Gazebo for small to medium-sized simulations. However, as the environment scale increases, Gazebo's resource consumption grows substantially, leading to longer startup times and slower user interface updates. Therefore, integrating Gazebo as a rendering engine for underwater visual simulations requires significant time and resource investments, while ROS-Unity3D tends to maintain stable performance regardless of scene size. Overall, although Gazebo is superior for underwater physics and fluid interaction simulations, it has limitations in terms of graphical fidelity [7]. Thus, combining Gazebo's robust physical modeling with Unity3D's advanced rendering capabilities could be a promising approach to achieving high-fidelity underwater simulations.

Proposed Approach

This work proposes an approach that leverages Gazebo's native functionalities to simplify the integration process between simulators. The system integrates Gazebo and Unity3D for the simulation of underwater vehicles, with Gazebo providing realistic physical simulation and Unity3D delivering an immersive graphical environment. By combining these two simulators, the integration seeks to harness Gazebo's physical accuracy alongside Unity3D's graphical quality, enabling both to operate synchronously so that vehicle poses and movements remain consistent across environments. The primary objective is to ensure accurate pose correspondence of the robotic system after integration. This involves understanding each simulator's capabilities, evaluating their performance in underwater scenarios, and assessing the feasibility of effective integration to exploit their specific strengths. To achieve this, matching algorithms will be used to compare robotic poses in both simulators, and simulation experiments will be conducted to analyze discrepancies and validate the results. Figure 1 illustrates a diagram summarizing the research objective, emphasizing the integration of Unity3D and Gazebo to establish a unified simulation environment.

System Architecture

The proposed architecture is designed to create a modular system for simulating the underwater vehicle. Within this architecture, ROS serves as the middleware, organizing and facilitating communication between components and simulation systems to ensure standardized and efficient data flow. Its primary objective is to integrate platforms such as Gazebo and Unity to simulate the vehicle's behavior and its interaction with the environment. For commanding and testing, inputs like forces, torques, and ocean currents are treated as dynamic variables applied to the system to replicate different physical conditions. These inputs are essential for validating the system's behavior. Initially, the robot_state_publisher package utilizes a preconfigured URDF file to describe the robot's configuration and parameters, publishing the

Figure 1. Research objective.

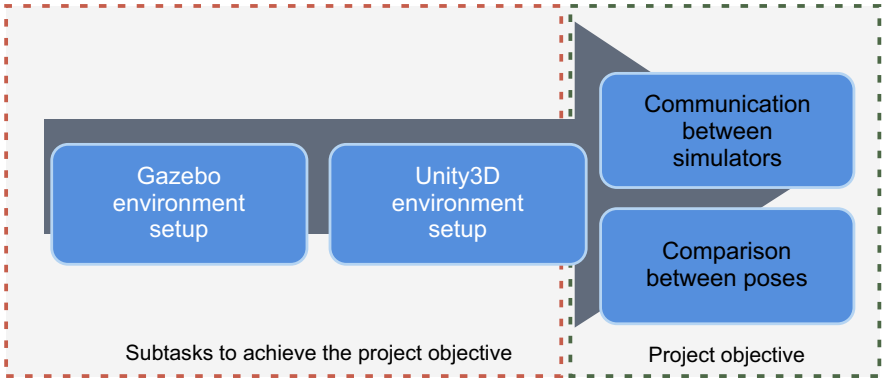

robot state information to the appropriate ROS topic. Using this information, the created node generates the simulated representation of the robot within Gazebo's virtual environment. This communication flow is illustrated in Figure 2, where nodes and topics interact to ensure the URDF-defined model is accurately instantiated in the simulator.

The parameter bridge node then acts as an interface between ROS and Gazebo (Figure 3). It converts topics and messages between Gazebo's native format and ROS-compatible topics, enabling integration of simulated data with other system components. This bridge ensures that information flows seamlessly between Gazebo and ROS.

In Unity, integration with ROS is achieved through the ROS TCP Endpoint component, which functions as a TCP server (Figure 4). This server, in conjunction with the ROS TCP Connector, translates ROS messages into a format interpretable by Unity3D, enabling data exchange between the simulation system and the graphics engine. The topics model_rov_pose and gui_camera_pose are processed by two scripts responsible for applying transformations from

Figure 2. Gazebo side architecture representation.

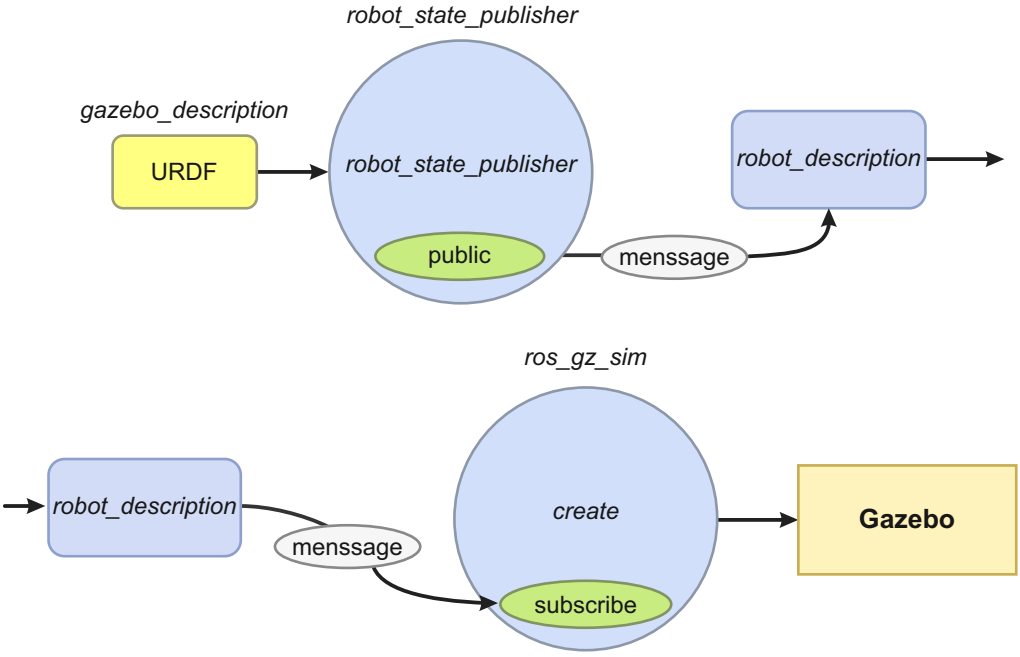

Figure 3. Gazebo topic transformation for ROS.

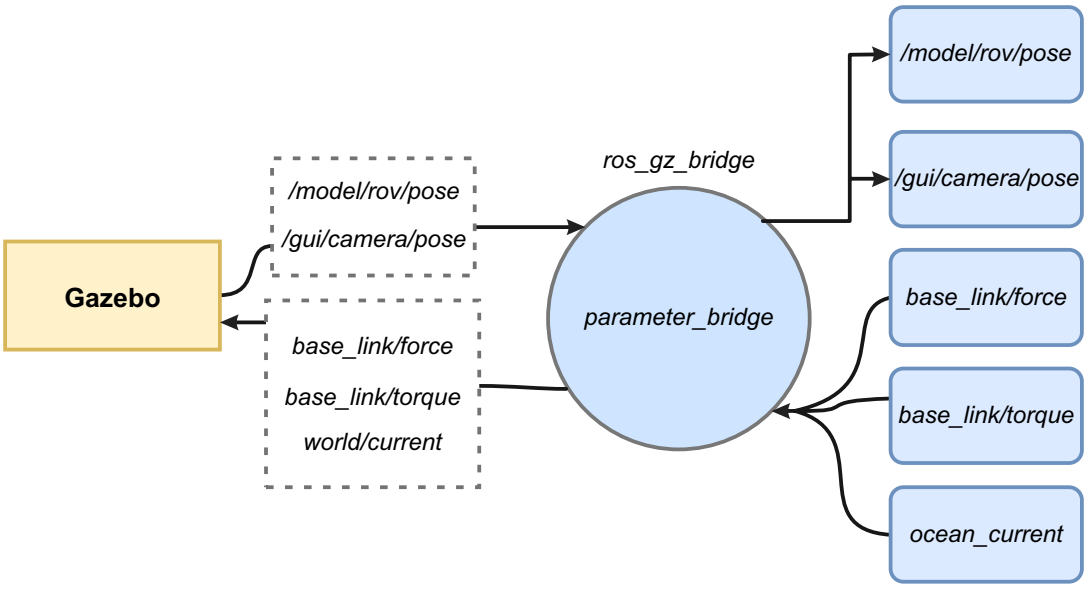

Figure 4. Unity ROS TCP integration.

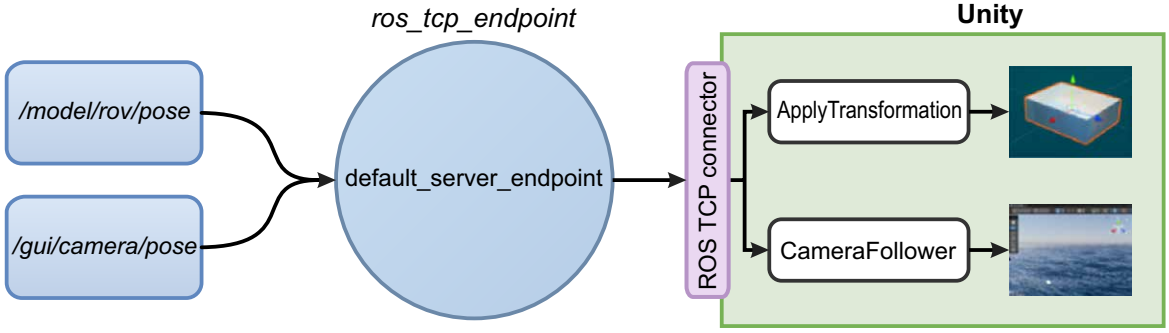

Gazebo to the vehicle and camera within the Unity environment.

Simulation Factors

To evaluate the behavior of the simulated system under different conditions, the simulation will be tested using an approach based on varying key input factors. By systematically adjusting these controllable variables, it is possible to analyze their impact on the underwater vehicle's performance and verify the consistency of results between the Gazebo and Unity3D simulators. The factors in this experiment are independent and controllable variables, adjusted to assess their influence on the simulated system's behavior. Specifically, the factors considered are:

- Applied Force (N): Directly affects the underwater vehicle's movement.
- Torque (Nm): Governs the vehicle's rotation and stability.
- Water Current (m/s): Models the effect of water flow on the vehicle's motion.

Selecting these factors enables the evaluation of how various operational conditions impact the simulators responses and whether the results remain consistent between Gazebo and Unity3D. In Figure 5, arrows connecting ellipsoidal nodes to rectangular topics illustrate the data flow from the simulation to the vehicle's navigation system. Some nodes publish messages, while others subscribe to these messages to execute specific functionalities.

Figure 5. Simulation data flow.

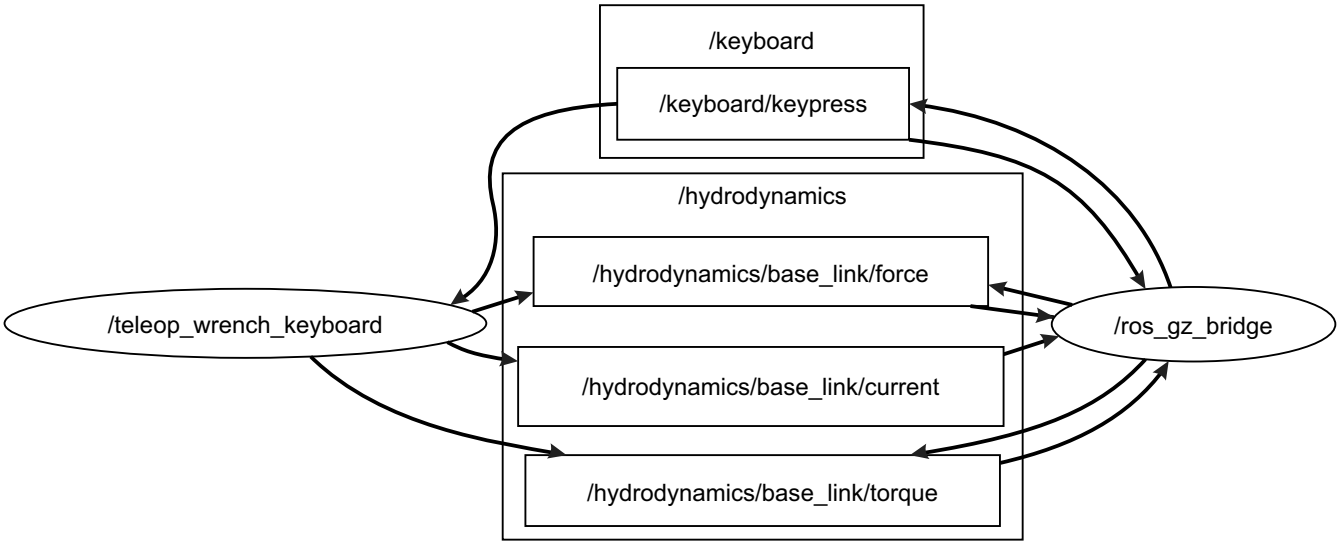

The teleop_wrench_keyboard node captures keyboard inputs corresponding to force, torque, and water current commands, publishing them to the relevant command topics. This node is used to apply the simulation factors during the experiment

Validation Methodology Proposal

Validating the integration concept between the Gazebo and Unity3D simulators for underwater robotics applications is essential to prove the proposed concept. The validation methodology comprises the following steps:

- Test Environment: Configure a default scene in both simulators containing the underwater vehicle positioned at the same starting point.
- Initialization: Initialize simulators and command interfaces.
- Execution: Perform vehicle navigation in the underwater environment using the teleop node from the teleop_wrench_keyboard package.
- Data: Collect and process pose data from Gazebo and Unity.
- Validation: Evaluate accuracy by comparing the data collected.

The evaluation of the accuracy and fidelity in synchronizing the position and orientation of the vehicle between the simulators is carried out using the following metrics:

- Absolute Error: Represents the direct difference between the values from Unity and Gazebo. It is useful for measuring the actual discrepancy between the data without considering the scale of the values.
- Mean Absolute Error (MAE): Indicates the average of absolute errors, smoothing out peaks and showing a general trend. This error is relevant for evaluating the overall accuracy of the simulators.
- Pearson Correlation Coefficient: Measures the linear relationship between Unity and Gazebo values, indicating the degree of synchronization between the simulators. A value close to 1 suggests high similarity, while values near 0 indicate lack of correlation. This metric is essential for verifying the fidelity of the integration between both environments.

Conclusion

This work emphasizes the importance of simulation as a practical and cost-effective tool for developing underwater robotic systems, particularly in scenarios where real-world testing presents logistical, safety, or financial challenges. The integration of Gazebo and Unity3D aims to combine Gazebo's

robust physical modeling with Unity3D's high-fidelity graphical rendering, enabling more realistic and immersive simulations. A critical stage in this process is the configuration of the simulators, which directly influences the accuracy and performance of the integrated system. Proper configuration involves defining the physical parameters, hydrodynamic properties, and communication interfaces within Gazebo to ensure that forces, torques, and environmental effects are realistically simulated. Likewise, configuring Unity3D requires setting up the ROS integration, graphical assets, and scripts that accurately interpret and apply the simulation data received from Gazebo. Careful attention to these configurations is essential to guarantee consistency between both environments, minimize errors, and ensure reliable data exchange during the experiments. The next steps involve conducting systematic simulation experiments by varying the identified input factors—applied force, torque, and water current—to evaluate the underwater vehicle's behavior under different operational conditions. These experiments will analyze the consistency and accuracy of the integration by comparing the vehicle's poses and movements across Gazebo and Unity3D. Finally, to validate the proposed model, results from these simulations will be assessed against theoretical expectations or experimental benchmarks, ensuring that the system replicates the anticipated physical responses with sufficient accuracy. Quantitative analysis will be performed to measure discrepancies between the two simulators, identifying any limitations or adjustments needed. This validation is fundamental to confirm that the integrated simulation environment can reliably support future development, testing, and refinement of underwater robotic algorithms and applications.

References

1. Brutzman DP, Kanayama Y, Zyda MJ. Integrated simulation for rapid development of autonomous underwater vehicles. In: Proceedings of the 1992 Symposium on Autonomous Underwater Vehicle Technology. IEEE; 1992. p. 3-10.
2. Song F, An PE, Folleco A. Modeling and simulation of autonomous underwater vehicles: design and implementation. IEEE J Ocean Eng. 2003;28(2):283-96.
3. Nahon M. Determination of undersea vehicle hydrodynamic derivatives using the USAF DATCOM. In: Proceedings of OCEANS '93. Vol. 2. IEEE; 1993. p. II283-8.
4. Katara P, et al. Open source simulator for unmanned underwater vehicles using ROS and Unity3D. In: 2019 IEEE Underwater Technology (UT). IEEE; 2019. p. 1-7.
5. Chaudhary A, et al. Development of an underwater simulator using Unity3D and Robot Operating System. In: OCEANS 2021: San Diego–Porto. IEEE; 2021. p. 1-7.
6. Platt J, Ricks K. Comparative analysis of ROS-Unity3D and ROS-Gazebo for mobile ground robot simulation. J Intell Robot Syst. 2022;106(4):80.
7. Allan M, et al. Planetary rover simulation for lunar exploration missions. In: 2019 IEEE Aerospace Conference. IEEE; 2019. p. 1-19.

Degradation of Fluorophores in Hydraulic Fluids: Impacts on Fluorescence Intensity and Color Contrast for Underwater Leak Detection

Rafael Nascimento de Menezes[1]*, Rodrigo Dias Sarno[1], Bianca Kurihara Yoshii[1], Mariana Chagas Alcantara dos Santos[1], Lucas Cruz da Silva[1], Milena Ventura Castro Meira[2], Valéria Loureiro da Silva[1]

[1]SENAI CIMATEC University, Optics and Photonics Engineering Laboratory; [2]Federal University of Bahia (UFBA), Institute of Physics; Salvador, Bahia, Brazil

Camera and lighting systems are widely used in underwater environments for research and inspection purposes. Many submerged machines use hydraulic fluids that contain luminescent markers. This characteristic can assist in visual detection through imaging systems. However, due to environmental conditions, these fluorophores undergo degradation, which affects fluorescence intensity. To study the effect of fluorophore degradation on color contrast in hydraulic fluids, color contrast and spectroscopy tests were conducted. This study is relevant for the development of image-based leak detection systems for fluids containing fluorescent markers.

Keywords: Fluorescence. Contrast. Spectroscopy. Degradation.

Abbreviations: WCAG, Web Content Accessibility Guidelines. RGB, Red Green Blue. SDK, Software Development Kit. LED, Light Emitting Diode.

Imaging and illumination systems designed for underwater environments have been the focus of intensive research since the early 20th century in order to improve visual performance under challenging optical conditions [1]. These technologies have found widespread application in marine life, and, more recently, in detection and monitoring of subsea fluid leakages [2,3].

Some of these fluids contain luminescent fluorophores, meaning that when they interact with photons of a specific energy level, they become excited and emit light, fluorescence, with photons of lower energy than those used for excitation. As a result, the fluo-rescence spectrum generally occurs at longer wavelengths than the absorption spectrum, following the Jablonski diagram and the Stokes shift for fluorescence (Figure 1) [4].

Previous studies on fluorescent hydraulic fluids have reported emission spectra ranging from 540 nm to 640 nm, with an emission peak centered around 580 nm. The emission intensity is proportional to the concentration of the fluorophore solution, providing a quantifiable optical signature [5]. This phenomenon can generate chromatic contrast between the leaking fluid and its surrounding environment, which can be quantified using color contrast calculation methods [6]. Such spectral distinction enhances the detectability of leaks, when captured by imaging systems equipped with color-sensitive sensors [7]. However, the optical behavior of these fluorophores is susceptible to degradation over time, which significantly affects both fluorescence intensity and spectral characteristics. This degradation arises from physicochemical processes such as fluorescence quenching, triggered by environmental parameters including temperature, pH and exposure to reactive species [2]. These alterations can be tracked through spectral analysis, which reveals both the reduction in emission intensity and potential bathochromic shifts of the fluorescence peak as the compound,like hydraulic oil, undergoes chemical aging [2,8]. This work investigates the degradation of the fluorophore within a hydraulic fluid sample over seven days and assesses its impact on the resulting color contrast between the fluid and a controlled background.

Received on 15 June 2026; revised 20 September 2026.
Address for correspondence: Rafael Nascimento de Menezes. com. SENAI CIMATEC University. Avenida Orlando Gomes, 1845, Piatã. Salvador – BA – Brazil, ZIP code: 41650-010. E-mail: rafael.menezes@fbter.org.br.

J Bioeng. Tech. Health 2026;9(10):990-996
© 2026 by SENAI CIMATEC University. All rights reserved.

Figure 1. Stokes shift graph example.

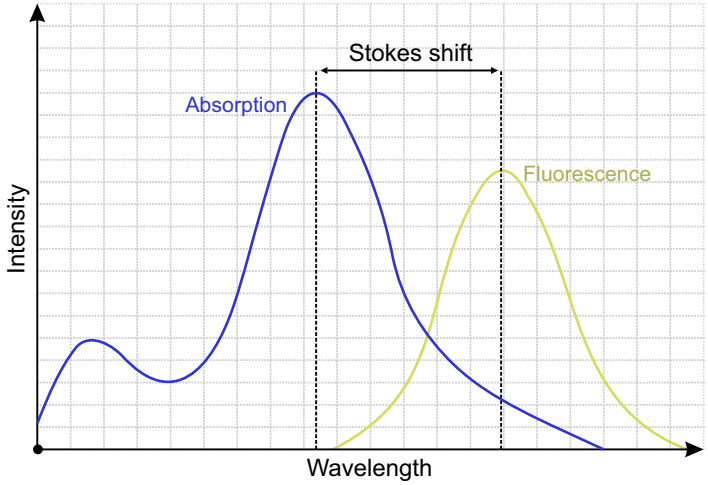

Materials and Methods

To assess the effect of a seven-day degradation period on the chromatic contrast generated by the fluorophore, two complementary experiments were performed. The first evaluates the color contrast between the hydraulic fluid and a background, using the contrast ratio metrics defined by the Web Content Accessibility Guidelines (WCAG) [6]. The second experiment employed spectroscopic analysis to characterize the extent of fluorophore degradation in the fluid sample.

To evaluate the change in color contrast due to fluid degradation under controlled lighting conditions, an experiment setup was assembled inside a compact photographic lightbox (Figure 2) that provided uniform illumination and eliminated the ambient light interference, which was composed by white light sources. The experiment occurred within a room with the air conditioner turned on and offering the temperature of 20°C. A glass tank, measuring 24.5 cm × 10 cm × 8 cm, was filled with approximately 1.7 L of water. A custom-built support structure was installed inside the tank to securely position the cuvette. A black background plate was placed directly behind the sample holder to simulate the low light conditions typical of deep-sea environments. The illumination source, a Thorlabs LED module, emitting in the blue spectral region, to provide uniform illumination across the entire cuvette volume.

Image acquisition was carried out using a camera connected to a computer via a GigE interface. The camera was externally mounted on the front facing side of the tank, with a lens attached to the camera and with careful precision to achieve the ideal focus on the cuvette through the water-filled aquarium precisely focused on the cuvette to ensure high-resolution imaging.

All of the equipment was fixed in the correct positions with the aid of small metal pipes, with the intuition of keeping everything held in place and still to avoid unwanted modifications in the optical alignment and images-gathering. The sample under investigation comprised a 3.5 mL solution containing 70% water and 30% hydraulic fluid, with a pH of 9.1 known to exhibit green fluorescence when exposed to radiation in the blue range.

The experimental procedure involved introducing the sample into the cuvette, activating the LED module, and maintaining a fixed optical power by limiting the supply current to 1 ampere (A). Image capture was then initiated through a custom code which allowed real-time control over individual RGB color gains, adjustment of exposure duration, image acquisition, and

execution of contrast analysis using WCAG and the camera manufacturer's Software Development Kit (SDK). Contrast evaluations were performed by systematically varying the Blue (B) and Green (G) gains parameters within the RGB model and setting the Red (R) gain and exposure time at 5000 ms.

In parallel with the color contrast test, a spectroscopy analysis was conducted to monitor the degradation of the same prepared sample. As shown in Figure 3, the optical setup incorporated two solarized optical fibers, Ocean Optics model QP600-2-SR, with a diameter of 600 micrometers. One end of each fiber was connected to an Ocean Optics CUV-FL-DA cuvette holder. Emitted fluorescence was collected orthogonally to the excitation beam and directed to a spectrometer for spectral analysis. This orthogonal geometry minimized the detection of scattered excitation light and enhanced the signal-to-noise ratio of the fluorescence measurements. Similar to the other experimental setup, this second experiment was built within the same room and with the same temperature (20°C), and the cuvette was closed with a lid, with the goal of minimizing evaporation from the water contained within the cuvette.

Results and Discussion

Figures 4 to 7 present the contrast level obtained in the first test conducted. The X and Y axes correspond, respectively, to the gain values to the blue and green channels, assigned by the RGB gain control algorithm implemented in the imaging system. The Z axis represents the computed contrast

Figure 2. Laboratory setup for contrast tests.

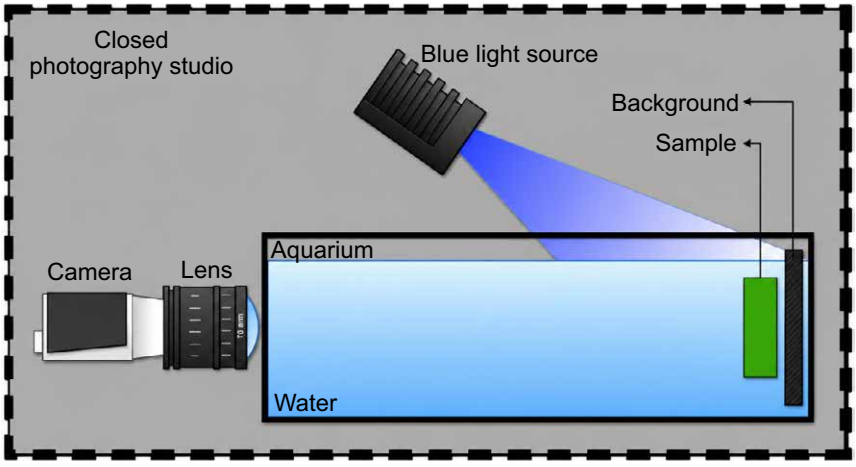

Figure 3. Laboratory setup for fluorescence tests.

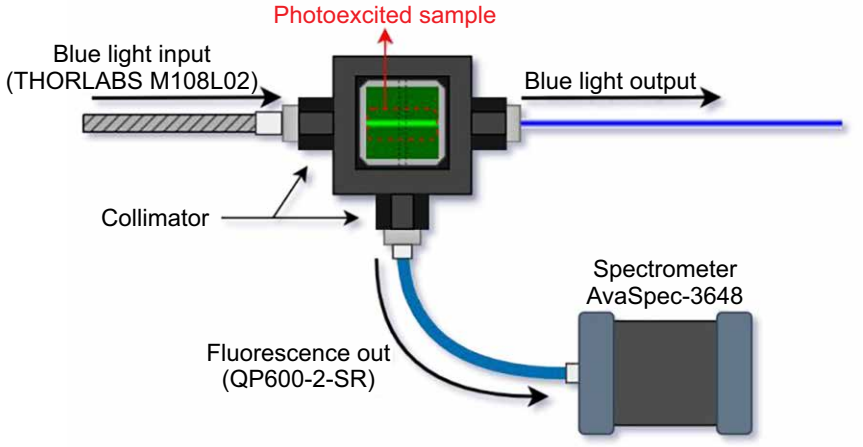

intensity for each configuration, quantifying the visual distinction between the hydraulic fluid and the background based on colorimetric analysis.

Specifically, Figure 4 shows the contrast distribution for a freshly prepared sample. Figures 2 to 4 illustrate the progressive contrast variations observed after 2, 4, and 7 days of sample aging, respectively.

The superficies profiles depicted in the graphs exhibit consistent topological patterns over time. However, a progressive decline in overall contrast intensity was observed upon examination of the data point distribution. As summarized in Table 1 the maximum contrast value decreased systematically with sample aging, culminating in an approximately 45% reduction after seven days.

Figure 8 displays the fluorescence spectrum acquired from the sample over seven days, beginning on the first day of degradation. A progressive decline in fluorescence intensity was observed throughout the week, with the emission signal gradually diminishing and ultimately reaching a minimum by the final day.

Figure 4. Contrast results from the first day.

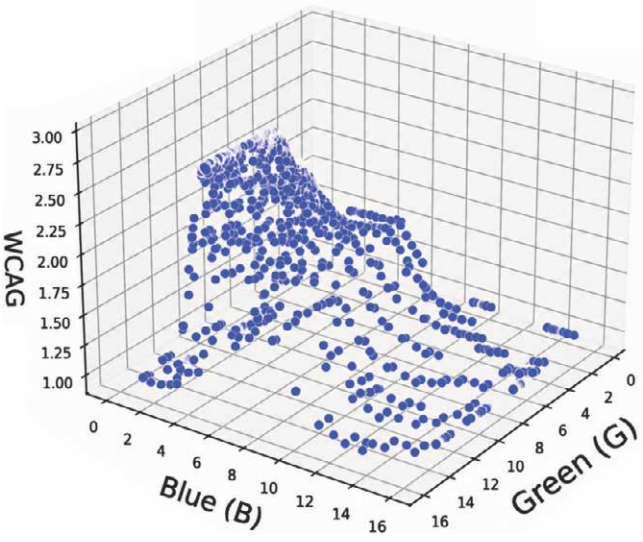

Figure 5. Contrast results from the second day.

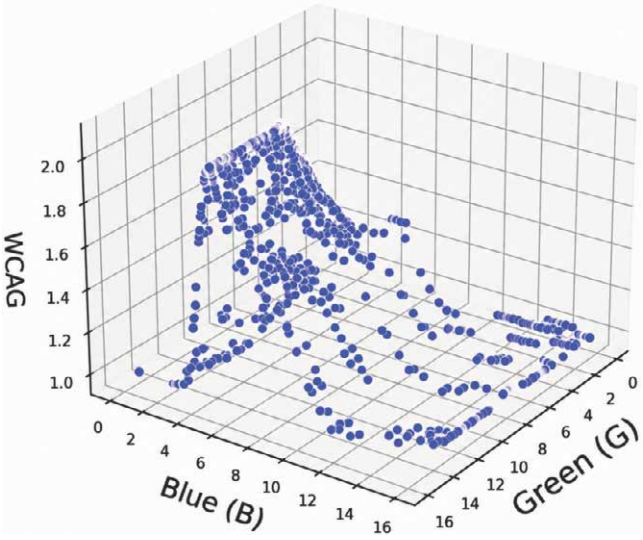

Figure 6. Contrast results from the fourth day.

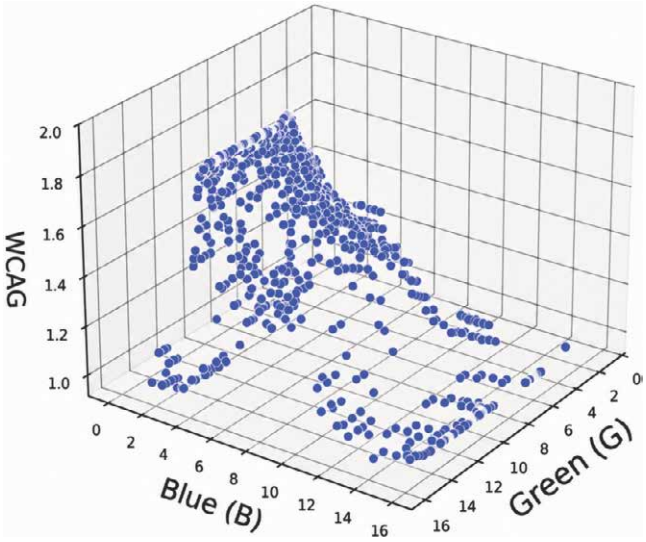

Figure 7. Contrast results from the seventh day.

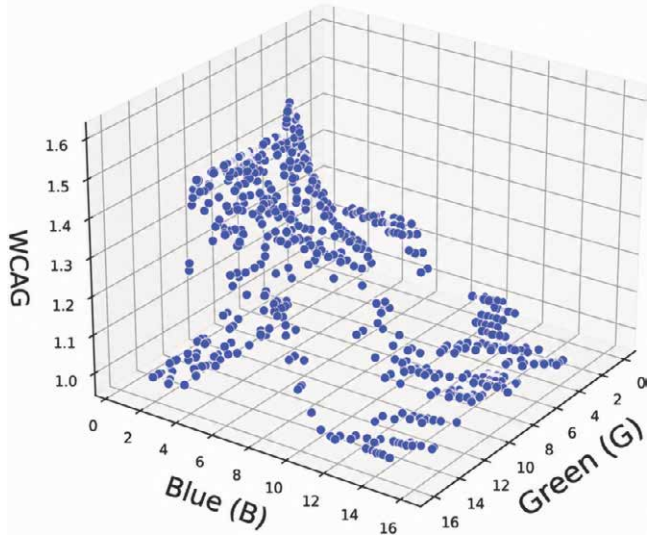

Table 1. Maximum WCAG values from each graph in the fluorescence test.

Day	WCAG Value
Day 1	2.91015625
Day 2	2.076171875
Day 4	1.931640625
Day 7	1.594726563

Table 2. Peak values from the fluorescence test on the vertical axis.

Day	Maximum ADC Value (a.u.)
One Day	62737
Three Days	51978
Seven Days	51863

Table 2 presents the maximum intensity values recorded. A pronounced decrease in intensity was observed between the first and third days. Beyond this point, the fluorescence amplitude stabilized.

The findings from both the contrast and spectroscopic analyses confirm that the temporal degradation of the sample adversely affects its fluorescence emission. In the first test, there was a total loss of 45.2% for the WCAG value over 7 days, while in the second test, there was a total loss of 17.3% for the maximum ADC value over 7 days. As the fluorophore deteriorates, the emitted intensity under constant excitation power diminishes, leading to a corresponding reduction in the color contrast between the sample and the background. In the contrast evaluation tests, the fluorescence phenomenon is responsible for generating a vivid green hue in the fluid, which, when placed against a black background is designed to maximize visual contrast. As fluorescence weakens over time, the loss of this characteristic green emission results in a measurable decline in contrast, impairing the visual differentiation between the fluid and its surroundings.

These conclusions are relevant to practical applications involving subsea inspections of oil and gas equipment. On the seafloor, light penetration is severely limited [9], which hinders the visual identification of fluids handled by these systems. Under such conditions, excitation at specific wavelengths permits the detection and distinction of those substances via their characteristic fluorescent emissions [10]; however, because emitted fluorescence light declines as fluorophores degrade over time, and even under constant excitation power, awareness of this temporal reduction, also known as photobleaching, is essential to avoid loss of fluid recognition during inspections [11].

Figure 8. Spectrometer results for the fluorescence test in graph format.

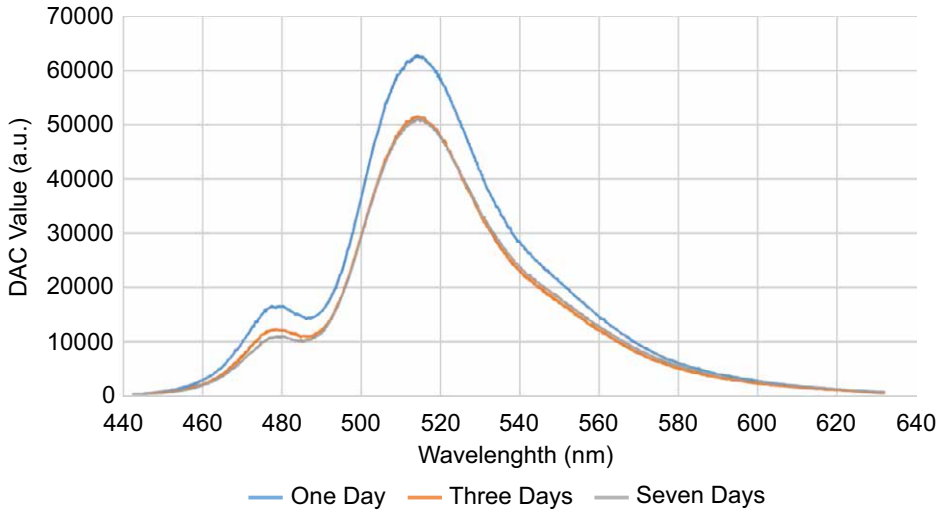

Conclusion

In the context of leak detection techniques for substances containing fluorophores, exploiting luminescence properties is an alternative approach to enhance visual contrast and facilitate identification. This study showed that the progressive degradation of the fluorophore present in a specific hydraulic fluid resulted in a reduction of fluorescence intensity, directly impacting the fluid's visibility against a black background. This decline in luminescent response over time constitutes a limitation for the reliability of fluorescence-based detection systems.

The observed decrease in emission intensity increases the likelihood of undetected leaks, environmental contamination and unplanned maintenance interventions. These challenges carry direct economic impacts: more frequent inspections may become necessary, and investments in advanced real-time monitoring and diagnostic systems may be required to maintain sensitivity and reduce detection latency. Without such measures, regulatory scrutiny and liability exposure are likely to increase. [12].

As a potential focus for future research and to mitigate these limitations future implementations could benefit from strategies such as, increasing the illumination intensity and positioning the light source closer to the fluorophores constitute viable measures to partially counteract the observed fluorescence decay. Moreover, while the experiments reported herein were limited to a seven-day observation window due to temporal restrictions during the study, extending the experimental period of analysis in future investigations would provide a more rigorous evaluation of long-term marker stability and operational viability. This methodology may be extended to other fluorescent fluids, such as Rhodamine WT [13], which emerges as a relevant candidate, since it exhibits a maximum fluorescence decay of 5% over 327 hours. This slower degradation rate and higher resilience to photobleaching directly contribute to maintaining fluorescence intensity over longer operational periods, thereby supporting more reliable visualization and contrast under field conditions.

Acknowledgement

The authors would like to thank Shell Brasil Petróleo LTDA, the Brazilian Company for Industrial Research and Innovation (EMBRAPII), the Brazilian National Agency for Petroleum, Natural Gas and Biofuels (ANP), the National Council for Scientific and Technological Development (CNPq), and SENAI CIMATEC for their support and investments in R&D&I.

References

1. Jaffe JS. Underwater optical imaging: the past, the present, and the prospects. IEEE J Oceanic Eng. 2015;40(3):683-700. doi:10.1109/JOE.2014.2350751.
2. Vogt A, D'Angelo C, Oswald F, Denzel A, Mazel CH, Matz MV, et al. A green fluorescent protein with photoswitchable emission from the deep sea. PLoS One. 2008;3(11):e3766. doi:10.1371/journal.pone.0003766.
3. Conmy RN, DiPinto L, Kukulya A, Garcia-Pineda O, Graettinger G, Sundaravadivelu D, et al. Advances in underwater oil plume detection capabilities. Int Oil Spill Conf Proc. 2021;2021(1). doi:10.7901/2169-3358-2021.1.1141330.
4. Lakowicz JR. Principles of fluorescence spectroscopy. 3rd ed. New York: Springer Science+Business Media; 2006.
5. Costello L, McStay D, Moodie D, Kane D. Permanent underwater leak detector. J Phys Conf Ser. 2009;178:012031. doi:10.1088/1742-6596/178/1/012031. Available from: https://www.researchgate.net/publication/243674456_Permanent_Underwater_Leak_Detector.
6. World Wide Web Consortium (W3C). Web Content Accessibility Guidelines (WCAG) 2.0: relative luminance [Internet]. W3C Recommendation; 2008 Dec 11. Available from: https://www.w3.org/TR/WCAG20/. Accessed 2025 Jul 24.
7. Zhou R, Liao X, Zhang Y, Zhang Z. Research on technique to identify and process the fluorescence picture by computer. Adv Mater Res. 2014;940:535-539. doi:10.4028/www.scientific.net/AMR.940.535.
8. Ossia CV, J, Lee A. Fluorescence sensor for characterization of hydraulic oil degradation. Int J Fluoresc. 2015. Available from: https://www.researchgate.net/profile/Cv-Ossia/publication/283153587_Fluorescence_Sensor_for_Characterization_of_Hydraulic_Oil_Degradation.

9. Wollschläger J, Tietjen B, Voß D, Zielinski O. An empirically derived trimodal parameterization of underwater light in complex coastal waters: a case study in the North Sea. Front Mar Sci. 2020;7:512. doi:10.3389/fmars.2020.00512.
10. Baszanowska E, Otremba Z. Seawater fluorescence near oil occurrence. Sustainability. 2020;12(10):4049. doi:10.3390/su12104049.
11. Benson DM. Digital imaging fluorescence microscopy: spatial heterogeneity of photobleaching rate constants in individual cells. J Cell Biol. 1985;100(4):1309-1323. doi:10.1083/jcb.100.4.1309.
12. Rahman MA, Barooah A, Khan MS, Hassan R, Hassan I, Sleiti AK, et al. Single and multiphase flow leak detection in onshore/offshore pipelines and subsurface sequestration sites: an overview. J Loss Prev Process Ind. 2024;90:105327. doi:10.1016/j.jlp.2024.105327.
13. Stanbro WD, Pyrch DA. Stability of Rhodamine WT in saline waters. Water Resour Res. 1979;15(6):1631-1632. doi:10.1029/WR015i006p01631.

Development and Validation of a Measurement System for Vehicle Infotainment Bluetooth Classic Performance

Milton Plinio Flores Porto[1,2]*, Helio Pio Correia Lima Junior[1,2], Thiago Barros Murari[1], Marcelo Albano Moret Simões Gonçalves[1]

[1]SENAI CIMATEC University, Stricto Sensu Department; [2]Ford Motor Company; Salvador, Bahia, Brazil

In-vehicle infotainment (IVI) systems are critical to the modern driving experience, with Bluetooth connectivity for smartphones being a key feature for both functionality and safety. This study proposes and validates a measurement system to quantify Bluetooth signal strength between a Ford SYNC3 IVI unit and an ESP32 microcontroller in a controlled, open-air environment. The goal is to establish a reliable performance baseline for future vehicle evaluation. The methodology emphasized reliability, repeatability, and reproducibility by employing two IVI modules, two ESP32 microcontrollers, and two operators to collect data at distances ranging from 0.01m to 10m. Results demonstrated a predictable signal attenuation conforming to the Log-distance Path Loss Model and confirmed the high consistency of the measurement system across different hardware and operators. This work provides a validated data baseline that can be used to create a model for defining design requirements and, as a practical application, to identify defective IVI units before vehicle assembly, thereby reducing potential manufacturing costs.

Keywords: Vehicle Infotainment. Bluetooth Classic. Performance. MSA. RSSI.

Abbreviations: MSA, Measurement System Analysis. RSSI, Received Signal Strength Indicator.

World car travel is expected to triple between 1990 and 2050. The experience of the car journey makes the other modes of travel inflexible and fragmented. Having a vehicle is the major item of individual consumption after housing. Vehicles provide autonomy to decide when and where to go that only a car can give [1].

An in-vehicle infotainment (IVI) is a system that integrates the entertainment system with the objective of facilitating a better form of driving experience. A typical infotainment system consists of audio as well as video interfaces and touchscreen [2]. In recent years the number of cars on the road with manufacturers installed IVI increased dramatically [3]. One of the main features of the IVI is to connect the user phone to the IVI through Bluetooth technology mainly to use the audio system of the vehicle to stream audio and make phone calls [4].

Received on 17 June 2026; revised 20 September 2026.

Address for correspondence: Milton Plinio Flores Porto. Av. Orlando Gomes, 1845 Piatã, Salvador - BA. Salvador, Bahia, Brazil. ZIP code: 41650-810. E-mail: milton.porto@ba.estudante.senai.br.

J Bioeng. Tech. Health 2026;9(10):997-1002

© 2026 by SENAI CIMATEC University. All rights reserved.

Bluetooth technology emerged from the need for small data exchange without using cables and with low power consumption. It has become widely adopted by vehicle manufacturers because of the low cost of the components and that almost every smartphone has this technology [5].

As smartphones features improve and expands, individuals are becoming ever more attached to their devices and the services they provide. This means that having access to those features through the IVI is extremely important to the consumer. By providing such interaction, car manufacturers play an active role in reducing the number of accidents associated with mobile phone usage while driving [6].

The present study proposes to measure and validate the Bluetooth signal strength between an IVI system and an ESP32 microcontroller in a controlled environment. The aim is for this data to serve as a baseline for subsequent measurements in vehicles to identify if Bluetooth is performing as expected by design.

Materials and Methods

An experiment was conducted to measure how the signal strength of a Bluetooth Classic

communication between an automotive infotainment unit (Ford SYNC3) and an ESP32-based receiver behaves in an environment with no significant physical barriers, though it may still contain electromagnetic interference.

To operate the IVI system outside of a vehicular environment, a Ford Motor Company SYNC3 Technical Development Kit (TDK) was used (Figure 1). It is possible to power on the TDK with the module outside of its standard enclosure, thus allowing the Bluetooth technology to operate in a free space environment.

Figure 1. Technical development kit.



To enable the ESP32 to communicate with the TDK, an algorithm was developed in the C language so that the microcontroller could capture the signal power level. For this, it was necessary to set up the software development environment from Espressif, the company responsible for the design of the open-source ESP32 device (Figure 2). To write an algorithm specific to Bluetooth Classic, it was also necessary to configure the open-source BTstack framework from the company BlueKitchen.

It is needed to provide reliability, repeatability and reproducibility to the data-generating process. Quantifying and reporting these three facets with appropriate confidence intervals provides an explicit gauge of how much trust can be placed in the observed values and the conclusions [7].

Since radio communication is highly sensitive to interference, the algorithm was enhanced to capture 30 signal strength samples; these samples were then averaged to obtain a reliable value. To ensure the repeatability and reproducibility of the measurement system, two SYNC3 modules (SYNC3 3.0 with software 18093_DEVTEST and SYNC3 3.4 with software 19101_DEVTEST), two ESP32 microcontrollers (rev.1 chip ID: 2809024 and rev.2 chip ID: 16545708), and two operators were used (Figure 3). Measurements were taken at a height of 1.4 meters and at straight-line distances of 0.01, 2.5, 5, 7.5, and 10 meters.

This resulted in 8 (2 x 2 x 2) independent combinations per distance and 1200 (8 x 5 x 30) total samples.

Figure 2. Process to install the framework software to the microcontroller.

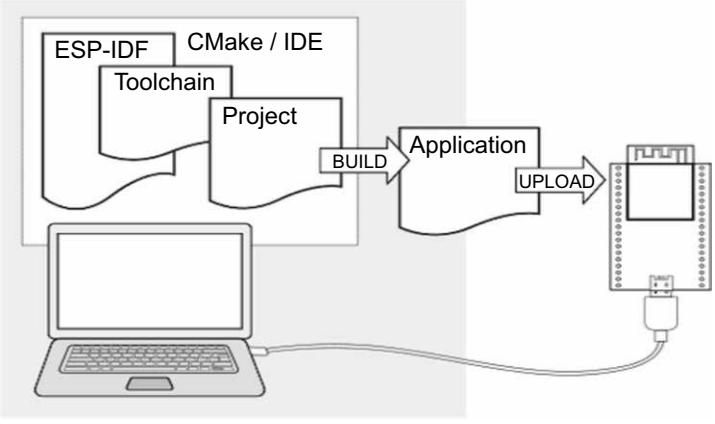

Figure 3. Modules and microcontrollers used in the experiment.



According to the manufacturer the ESP32's signal strength values can be from -10 (representing the strongest signal) to -100 (representing the weakest signal). To provide energy for the microcontroller it was connected to a laptop via a USB cable (Figure 4).

To have access to the collected data the terminal feature of the Arduino IDE software was utilized, with the data being sent through serial communication (Figure 5).

Figure 4. ESP32 connected to the laptop through the USB port.



Results and Discussion

Table 1 shows the summary of the data collected using the defined measurement system recording the maximum (Max), minimum (Min), and average signal strength (120 samples for each average) in dBm (decibel-milliwatts), along with the signal variance (Var in %). For each distance we have the combined values of measurements from person 1, person 2, ESP32 rev.1 and ESP32 rev.3.

At 10m the system is at its limits to start failing to deliver a good data exchange since it is expected to have a significant package loss below -70 dBm [8].

The variation at close range (less than 10%) compared with the other distances, except at 5m, (around 26%) show how sensitive to interference the radio wave is. At the distance of 5m the variation was higher (around 34%) because there was electric equipment (that it was not authorized to be removed) on the left side acting as a blocker for the correct propagation of the electromagnetic wave.

To estimate the RSSI at distances where direct measurements were not taken, it was used the Log-distance Path Loss Mode. The equation below demonstrates how the values are calculated:

$$RSSI(dBm) = RSSI_0(dBm) - 10 \cdot n \cdot \log_{10}\left(\frac{d}{d_0}\right) \quad (1)$$

As shown on Table 1, at the shortest distance of 0.01m, average signal strengths were relatively high, with SYNC 3.0 at -17.5 dBm and SYNC 3.4 at -17.0 dBm. As distance increased to 10m, the average signal strength significantly decreased, reaching -68.5 dBm for SYNC 3.0 and -69.3 dBm for SYNC 3.4. This demonstrates the typical path loss experienced by wireless signals.

The process begins with a calibration phase, where empirical RSSI values are collected at a set of known distances from the transmitter. These measurements are fitted to the model, which establishes a linear relationship between RSSI (in dBm) and the base-10 logarithm of the distance. This regression analysis determines the

Figure 5. Arduino IDE terminal output.

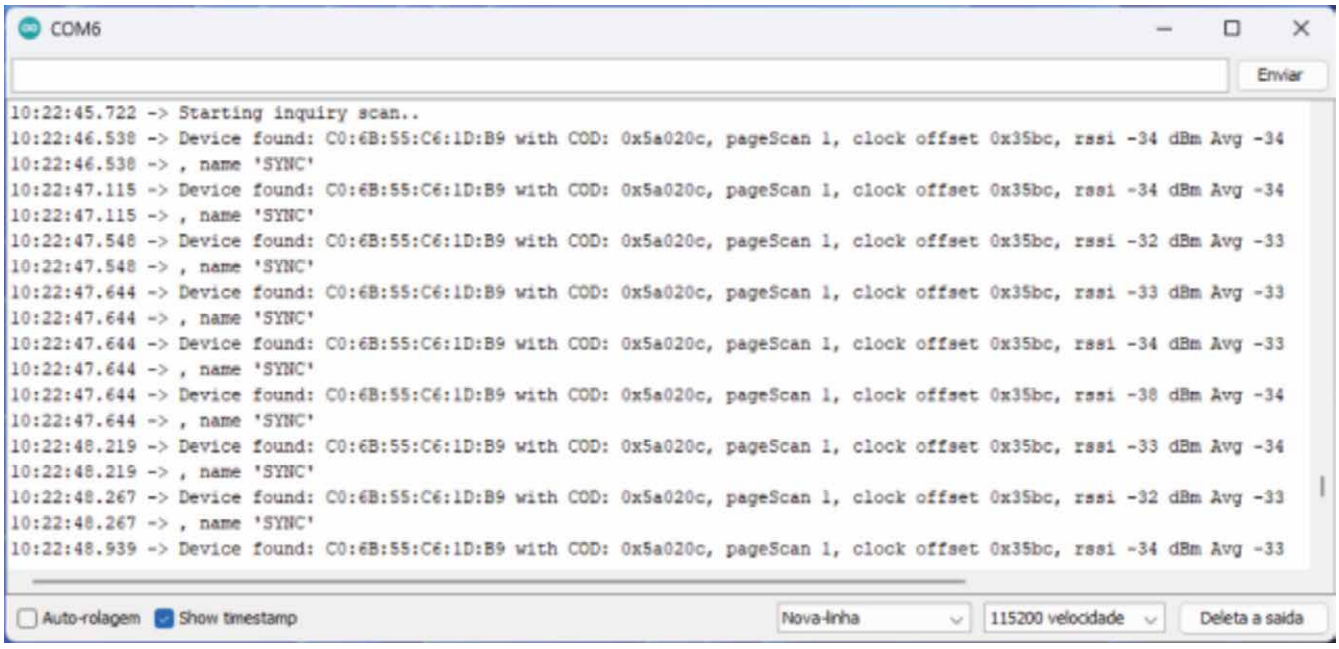

Table 1. Summary of the data collected.

	Distance (m)	Max (dBm)	Min (dBm)	Var (%)	Average (dBm)
SYNC 3.0	0.01	-14	-21	7.8%	-17.5
	2.5	-47	-70	25.6%	-58.5
	5	-52	-82	33.3%	-66.0
	7.5	-59	-84	27.8%	-67.3
	10	-60	-84	26.7%	-68.5
SYNC 3.4	0.01	-13	-21	8.9%	-17.0
	2.5	-50	-74	26.7%	-60.3
	5	-51	-83	35.6%	-64.8
	7.5	-59	-82	25.6%	-67.0
	10	-60	-84	26.7%	-69.3

key environmental parameters of the model: the path loss exponent (n), which describes the rate of signal decay, and the reference RSSI0 at a close-in distance (0.01m). The path loss exponent was calibrated for free space environment (n=2), the resulting equation provides a continuous function that can reliably interpolate or extrapolate to predict the expected RSSI value at any given distance within the model's effective range, thus enabling the creation of a complete signal coverage map from a limited set of empirical data points [9].

Measurements performed independently by two individuals, Person 1 and Person 2, produced results that were not statistically different, demonstrating

a high degree of consistency and minimizing the potential for operator-specific bias (Figure 6).

Data collected from two separate, but identical devices also showed equivalent results. This confirms the reliability measurement of the devices (Figure 7).

The data measured points for both SYNC 3.0 and SYNC 3.4 are nearly identical, indicating a highly comparable performance between the two systems (Figure 8). Although minor variations exist in the measured data at specific points, the overall signal behavior demonstrates that both SYNC versions exhibit predictable and consistent performance characteristics in a controlled environment.

Conclusion

The reliability and validity of the experimental methodology were successfully confirmed through a systematic comparison of data. Measurements performed independently by two individuals, Person 1 and Person 2, yielded statistically equivalent results. Concurrently, data collected from two separate but identical devices, ESP32 rev.1 and ESP32 rev.3, were also found to be in strong agreement. Both SYNC 3.0 and SYNC 3.4 modules demonstrate predictable signal attenuation with increasing distance. Their overall performance in terms of average, maximum, and minimum signal strength is highly comparable, with only minor deviations observed at specific distances that can be explained by the process variation of the build of the components/boards.

This work can be used to create a model that will help define the design to meet the requirements and customers' expectations. An application for this work would be to identify any problem with the Bluetooth system of the infotainment ECU while it is not assembled in the vehicle making a replacement of a defective module cost less.

Acknowledgement

The authors would like to thank Ford Motor Company for supporting this work.

Figure 6. Comparison of logarithmic regressions for RSSI *vs*. distance from person 1 and person 2.

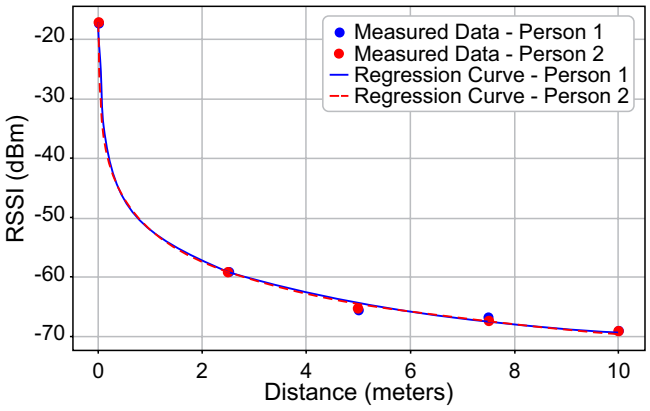

Figure 7. Comparison of logarithmic regressions for RSSI *vs*. distance from device 1 and device 2.

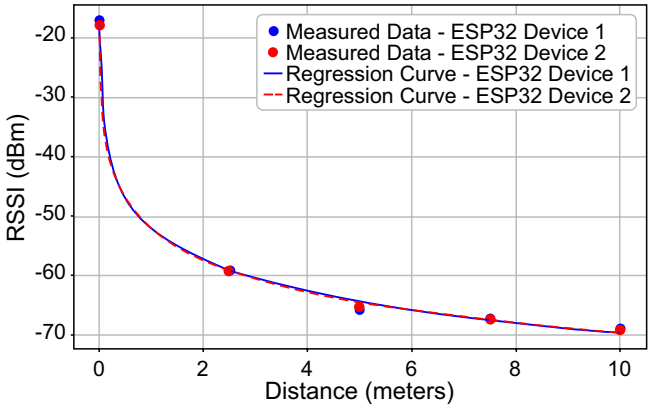

Figure 8. Comparison of logarithmic regressions for RSSI *vs*. distance from SYNC 3.0 and SYNC 3.4.

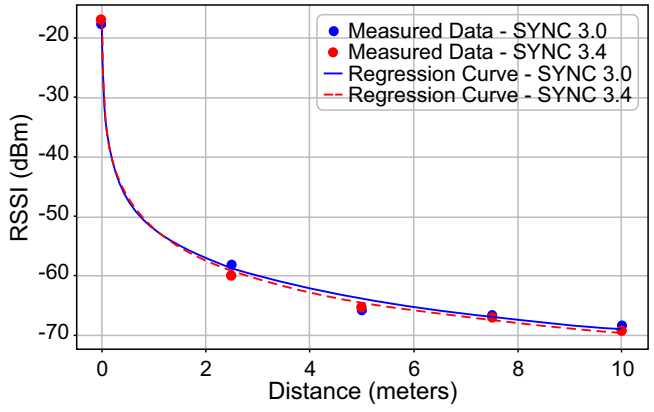

References

1. Urry J. The 'system' of automobility. Theory, culture & society. 2004;21(4-5):25-39.DOI: 10.1177/0263276404046059
2. Reshma S, Chetanaprakash C. Advancement in infotainment system in automotive sector with vehicular cloud network and current state of art. International Journal of Electrical and Computer Engineering. 2020;10(2):2077-2087.DOI: 10.11591/ijece.v10i2.pp2077-2087
3. Starkey NJ, Charlton SG. Drivers use of in-vehicle information systems and perceptions of their effects on driving. Frontiers in Sustainable Cities. 2020;2:39.DOI: 10.3389/frsc.2020.00039
4. Krstačić R, Žužić A, Orehovački T. Safety Aspects of In-Vehicle Infotainment Systems: A Systematic Literature Review from 2012 to 2023. Electronics. 2023;13:2563. DOI: 10.3390/electronics13132563
5. Muller, Nathan J. Bluetooth demystified. McGraw-Hill Professional; 2000.
6. Mourad, Alaa et al. On the performance of WLAN and Bluetooth for in-car infotainment systems. Vehicular Communications. 2017;10:1-12.DOI: 10.1016/j.vehcom.2017.08.001
7. Bartlett JW, Frost C. Reliability, repeatability and reproducibility: analysis of measurement errors in continuous variables. Ultrasound in obstetrics & gynecology. 2008;31(4):466-475. DOI: 10.1002/uog.5256
8. Allik K. RSSI-based Object Finding System [Bachelor's thesis]. Tartu: University of Tartu; 2016.
9. El Khaled Z, Ajib W, Mcheick, H. Log distance path loss model: Application and improvement for sub 5 GHz rural fixed wireless networks. IEEE Access. 2022;10:52020-52029. DOI: 10.1109/ACCESS.2022.3166895

Evaluation of the Tensile Properties of LLDPE/Sisal Composites Produced by 3D Printing

Ana Paula Gonçalves[1*], Lucas Huriuchi[1], Mariana Souza[1], Vinícius Oliveira[1], Rodrigo Polkowski[1]
[1]TRL9 LAB Testing and Technical Analysis; Salvador, Bahia, Brazil

This study evaluates the use of sisal residues as reinforcement in linear low-density polyethylene (LLDPE) composites produced by extrusion and 3D printing, with or without the compatibilizer Polybond™ 3029. The proposal is justified by the high volume of waste generated by the sisal industry, about 98% of the plant, corresponding to approximately 15 million tons annually worldwide, according to the FAO, and by the intrinsic advantages of plant fibers, such as low cost, low density, and wide availability. Three formulations containing 5% sisal residue (either in natura or treated with NaOH) and 17.5% Polybond™ were prepared and compared to a control consisting of pure LLDPE. Mechanical tests, conducted according to ASTM D638, revealed that the composite with Polybond showed tensile strength similar to that of the pure polymer but superior to the other formulations, indicating better fiber–matrix adhesion. The elastic modulus showed no statistically significant differences, and the elongation at break remained close to that of pure LLDPE. These results indicate that using untreated sisal residue can reduce production costs without compromising the material's ductility. It is concluded that incorporating sisal residues into LLDPE, especially with the addition of Polybond, adds value to an agricultural byproduct and fosters the development of sustainable composites with potential for diverse applications, such as packaging, consumer goods, and lightweight structures, including the possibility of customized production via 3D printing.
Keywords: Composites. Sisal. LLDPE. 3D Printing.

The increasing environmental concerns and the growing demand for sustainable materials have spurred interest in valorizing agricultural residues through the development of composite materials [1].

Currently, vegetal fibers, such as sisal, offer several advantages: low density, low cost, non-abrasiveness, and high modulus of elasticity. More importantly, they are abundant in nature, as they can be obtained through various cultivation methods. Both manufacturing methods and material selection play a crucial role in the development of polymer composites [2].

According to the FAO (Food and Agriculture Organization), the residual biomass after the extraction of sisal fiber accounts for about 98% of the plant, which amounts to approximately 15 million tons of waste per year worldwide [3].

Received on 18 June 2026; revised 21 September 2026.
Address for correspondence: Ana Paula Gonçalves. Parque Tecnológico da Bahia. Rua Mundo, nº 121, Ed. Tecnocentro, Trobogy, Salvador - Bahia, Brazil. ZIP code: 41745-715. E-mail: anapaula.goncalves@trl9.tech.

J Bioeng. Tech. Health 2026;9(10):1003-1009
© 2026 by SENAI CIMATEC University. All rights reserved.

Incorporating sisal residues as reinforcement into thermoplastics like linear low-density polyethylene (LLDPE) represents a compelling opportunity to create value-added composites with enhanced mechanical performance for various applications such as food packaging, grocery bags, industrial films, and tubes [4].

The processing route of compounding by extrusion followed by additive manufacturing (3D printing) enables precise control over fiber dispersion and part geometry. Recent studies on 3D-printed vegetal fiber composites, such as PLA reinforced with sisal strands have demonstrated notable improvements in tensile properties often outperforming conventional vegetable fiber composites [5].

This suggests that extrusion combined with layer-by-layer deposition can effectively integrate vegetable fibers into thermoplastics, enhancing interfacial bonding and mechanical integrity.

A critical factor in achieving robust tensile properties in such composites is the use of compatibilizers, such as Polybond, to improve adhesion between hydrophilic fibers and hydrophobic polymer matrices [6]. Using

compatibilizers or coupling agents is an effective approach to improving the interface between components [7]. These agents possess functional groups with affinity for both the fiber surface and the polymer matrix. One end of the coupling molecule reacts with groups on the reinforcement surface, while the other bonds with the functional polymer phase.

Polyethylene-grafted maleic anhydride (PE-g-MA) is a commonly used coupling agent to enhance compatibility between plant fibers and polymer matrices, as the maleic anhydride (MA) moiety interacts with the hydroxyl groups present in the fiber structure [7]. Although specific data on Polybond in LLDPE–sisal systems remain limited, literature indicates that compatibilizer-enabled surface modifications (e.g., alkali) substantially boost tensile strength, modulus, and impact resistance in sisal-reinforced composites [8].

Therefore, the addition of Polybond in LLDPE/sisal composites is expected to reinforce the fiber-matrix bond, which translates into superior tensile performance obtained by extrusion followed by 3D printing.

In summary, the combination of sisal residue valorization, extrusion compounding, Polybond compatibilization, and additive manufacturing fosters the development of sustainable LLDPE-based composites. These materials promise enhanced tensile properties and customisable geometries, with broad potential in automotive, consumer goods, and lightweight structural applications.

Materials and Methods

Materials

Sisal residue was supplied by the cooperative APAEB SISAL (Community Association for Sisal Production and Marketing) located in Valente. The polymer used to prepare the composites was LLDPE ML3602U from Braskem, with a density of 0.937 and a melt flow index (190 °C/2.16 kg) of 5.0.

Compatibilizing agent used was POLYBOND™ 3029 (SI Group). POLYBOND™ corresponds to HDPE modified with maleic anhydride (HDPE-g-MA) and is represented by the chemical structure in Figure 1.

Figure 1. Chemical structure of POLYBOND™

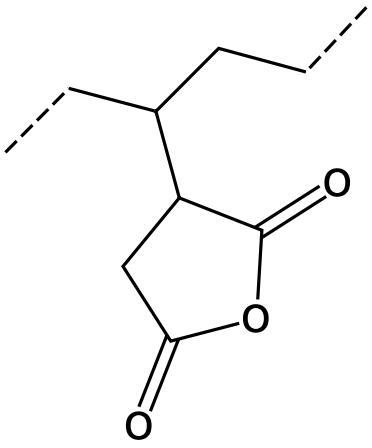

Fonte: Chloé Épinat, 2014.

Preparation of Composites

The sisal residue was oven-dried at 80 °C for 24 h and manually pre-mixed with the polymer. The composite pellets were prepared from three different formulations containing 5% sisal residue either in natura or subjected to alkaline treatment (5% (w/v) NaOH, 2 h, stirrer), and mixed with 17.5% POLYBOND™ 3029, as described in Table 1. In addition to these formulations, a control sample was produced, consisting of 100% LLDPE polymer.

Table 1. Composite formulations.

Sample	Descriptive
LLDPE	Pure LLDPE
LLDPE/5SN	LLDPE composite with 5% untreated sisal residue
LLDPE/5ST	LLDPE composite with 5% sisal residue treated with 5% NaOH
LLDPE/5SC	LLDPE composite with 5% sisal residue and Polybond compatibilizer

The composites were produced using a twin-screw extruder (L/D = 40 mm, AX-Plásticos, model DR1640, Brazil). The temperature profile and screw rotation speed were set to 100/150/170/180/190/190/195/200/195 °C and 120 rpm, respectively. After extrusion, the composites were granulated.

Filament Preparation

Filaments were produced using a Filmaq 3D screw extruder, operating at 185 °C and 18.5 rpm.

3D Printing

Prior to printing, the filaments obtained in the previous step were dried at 60 °C in a dryer. A Prusa Research MK3S+ printer was then used to fabricate the composite specimens under the following parameters: nozzle diameter: 0.6 mm; infill: 100%; print speed: 30 mm/s; printing temperature: 190 °C; bed temperature: 123 °C; orientation: 0°; infill pattern: rectilinear, layer height: 0.3 mm; substrate printing temperature: 255 °C.

Figure 2 shows the experimental scheme for sample preparation and Figure 3 shows the printed test specimens.

Tensile Testing

Test specimens were prepared according to ASTM D638, Type IV, and evaluated using an EMIC universal testing machine (model DL200MF) equipped with a 2 kN load cell. The tests were conducted at a crosshead speed of 50 mm/min, pulling each specimen until failure. Five specimens from each formulation were tested, and the following properties were determined: tensile strength (MPa), elongation at break (%), and tensile modulus (MPa).

Statistical Analysis

The Tukey test was applied to assess significant differences between mean values using the Statistica 7.0 software. Means followed by the same letters in the same column did not differ significantly at the 5% significance level (Tukey, $p < 0.05$).

Figure 2. Scheme for sample preparation.

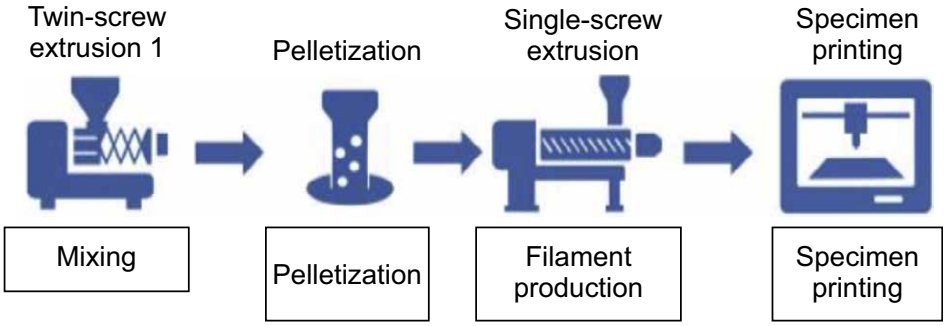

Figure 3. Printed test specimens.

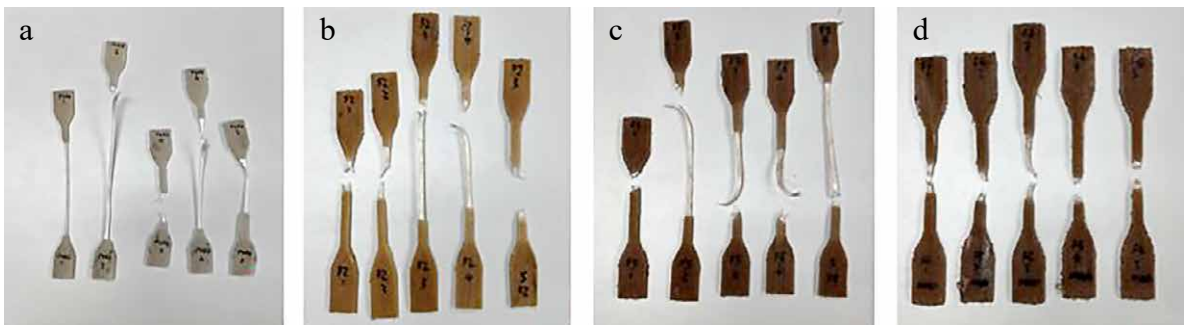

Results and Discussion

The stress–strain curves of the pure polymer and the composites are shown in Figure 4.

Based on the curve profile of the pure polymer, an elastic behavior followed by plastic deformation was observed, which is characteristic of a ductile material. A similar performance was observed for all three composites.

From Figure 4, it can be seen that the addition of sisal residue reduced the deformation of the LLDPE.

This behavior was expected, as it is associated with the higher stiffness and lower intrinsic elongation of the fibers compared to the polymer matrix. The fibers restrict the mobility of the polymer chains and introduce interfaces that can act as stress concentration points. As a result, the composite exhibits lower ductility and fractures at lower deformation levels compared to the pure matrix.

As previously mentioned, LLDPE exhibits ductile fracture, characterized by high deformation prior to failure, localized necking formation, and molecular alignment in the direction of the applied load. The fracture surface shows a smooth and elongated appearance, as illustrated in Figure 5.

Regarding the fracture mechanism, one hypothesis is that, in the plastic regime, molecular chains slide, the crystallites deform, and some partially break down. Thus, failure occurs when the elongated fibrillar structure can no longer sustain the load, leading to rupture by chain scission. In the case of a ductile matrix, there is no rapid crack propagation as observed in brittle fracture [9].

For the evaluated tensile properties, a Tukey test was performed to verify whether there were differences between the means of the pure polymer and the composites. Regarding the maximum stress values, shown in Table 2, it was observed that the pure polymer (LLDPE) and the composite (LLDPE/5SC), referring to the LLDPE composite containing 5% sisal residue with the compatibilizing agent POLYBOND, did not differ statistically from each other. However, they exhibited superior mechanical behavior compared to the other composites with untreated and NaOH-treated fibers.

This is possibly due to the improved adhesion at the fiber-matrix interface, resulting in more efficient load transfer and, consequently, enhanced mechanical properties. Maleic anhydride (MA),

Figure 4. Stress-strain curve of samples.

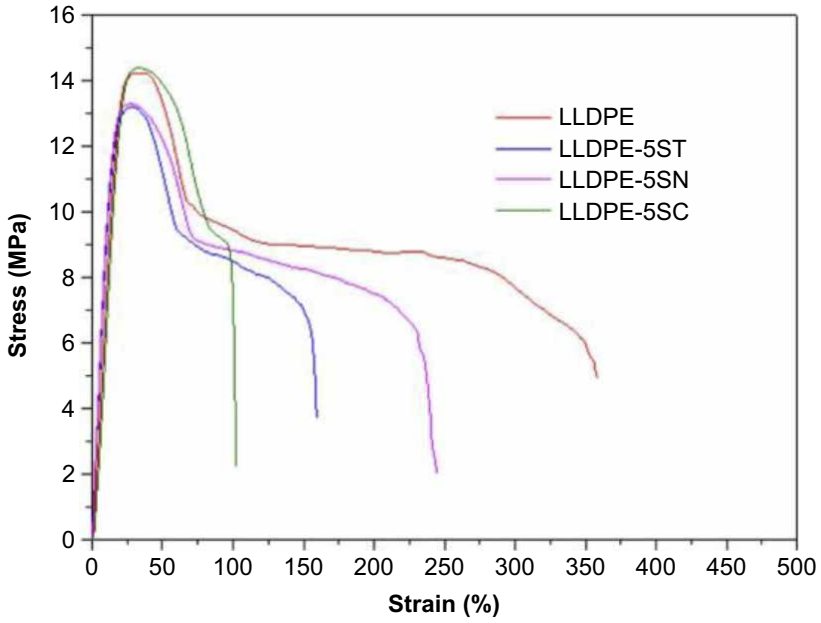

Figure 5. Test specimens after the tensile test.

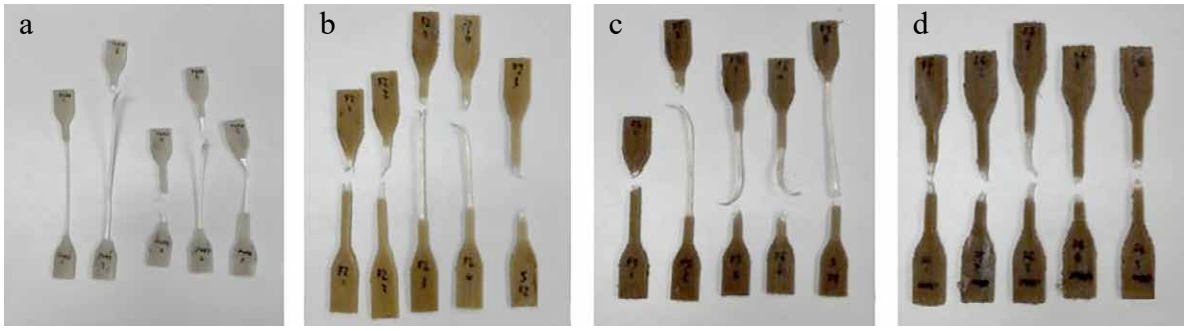

Table 2. Tensile strength (MPa) of pure polymer and composites.

Sample	Tensile strength (MPa)
LLDPE	14.82^{a}±0.77
LLDPE/5SN	13.56^{b}±0.43
LLDPE/5ST	13.50^{b}±0.50
LLDPE/5SC	14.57^{a}±0.30

present in POLYBOND™ 3029, reacts with the hydroxyl groups on the fiber surface. Through the formation of ester bonds between the MA groups and the fibers, the surface hydrophilicity is reduced, which in turn enhances the compatibility of the fibers with hydrophobic polymers [10].

Although NaOH removes impurities and increases fiber roughness, this treatment does not necessarily ensure strong chemical adhesion with the apolar LLDPE matrix. Moreover, even with such treatment, if the fibers are poorly dispersed, no significant improvement in tensile strength will be observed. Therefore, one possible reason why the NaOH chemical treatment did not improve the composite's maximum stress is the still limited interfacial adhesion between the fibers and the polymer matrix. Treatments often improve the adhesion between matrix and fiber; however, there is controversy in the literature regarding the effect of such treatments on the mechanical properties of the fibers and their reinforcing capability. Even when a more significant improvement is observed after chemical treatment, this enhancement is often within the variability of the results. In some cases, similar overall gains can be achieved by simply washing and drying the fibers prior to incorporation into the polymer matrix, which has the added benefits of being more economically viable and environmentally friendly than certain chemical treatments [11].

As observed in Table 3, an increase in the modulus of elasticity of the composites compared to the polymer matrix was expected, since the fiber interferes with the mobility of the polymer chains, leading to an increase in the modulus of elasticity [12]. However, based on the statistical evaluation using Tukey's test, the samples exhibited similar performance, with the exception of the LLDPE/5SC composite.

Mokoena and colleagues. (2004) studied composites of linear low-density polyethylene and short sisal fibers and observed an increase in the tensile strength of the polymer by adding 40% fiber, reaching approximately 22 MPa; with 10% sisal fiber, the tensile strength was about 17 MPa [13].

Table 3. Tensile modulus (MPa) of pure polymer and composites.

Sample	Tensile modulus (MPa)
LLDPE	83.28^{ab} ±4.65
LLDPE/5SN	108.22^{a}±16.69
LLDPE/5ST	100.67^{ab} ±17.24
LLDPE/5SC	82.22^{b}±7.51

Composites reinforced with vegetable fibers, such as sisal in LLDPE, may exhibit a modulus of elasticity similar to that of the pure polymer due to limited interfacial adhesion, low fiber volume fraction, and the presence of short or poorly dispersed fibers, factors that compromise efficient load transfer and the enhancement of the material's stiffness.

Strain at break is the measure of how much a material can elongate or deform before breaking during a tensile test. Expressed as a percentage, this property indicates the material's ductility, being high in ductile materials and low in brittle materials. Table 4 shows the deformation data of pure polymers and composites.

Table 4. Elongation at break (%) of pure polymer and composites.

Sample	Elongation at break (%)
LLDPE	81.87[a]±49.17
LLDPE/5SN	46.00[a]±22.30
LLDPE/5ST	36.83[a]±25.76
LLDPE/5SC	25.60[a]±8.85

Composites reinforced with vegetable fibers generally exhibit lower strain at break compared to the pure polymer, due to the higher stiffness of the fibers and the restriction of polymer chain mobility, resulting in reduced ductility. Table 4 shows the expected result of the decrease in this property when comparing the pure polymer to the composite.

Composites exhibit lower elongation at break than the pure polymer primarily due to the presence of rigid fibers that limit the material's elongation capacity. Vegetal fibers, such as sisal, have higher stiffness than the polymer matrix, which reduces the mobility of the polymer chains and consequently the plastic deformation before fracture. Moreover, the fiber-matrix interface can act as a stress concentration point, facilitating crack initiation. Imperfect adhesion may cause premature failures, while fiber breakage or slippage also contributes to the overall reduction in the composite's ductility. Thus, the combination of these factors results in lower strain at break in composites compared to the pure polymer.

The Tukey test showed that there was no difference between the pure polymer and the composites, nor among the different treatments applied to the composites. In this context, untreated sisal residue, for example, can be added to the polymer, reducing the material cost while maintaining the same strain at break as the polymer matrix.

Mokoena and colleagues (2004) studied composites of linear low-density polyethylene and short sisal fibers and evaluated the elongation at break, which was found to be lower (around 12%) compared to this work (46%). This difference may be related to the fiber content added as well as the type of linear low-density polyethylene used to prepare the formulations.

Preliminary Economic Assessment

For a preliminary economic assessment, the price of the composite components (untreated sisal waste and pure polymer) should be considered. Considering the commercial price per kilogram of each component, the composite containing 5% sisal (R$5.00) fiber and LLDPE (R$12.96) had a reduction of approximately R$0.40/kg, being around 3.1% cheaper than the pure polymer (LLDPE). It is worth noting that the absolute cost reduction or percentage reduction tends to increase as the fiber content increases. Thus, for example, a composite containing 50% sisal fiber would imply an absolute reduction of 3.98, corresponding to a percentage reduction of 30.72% when compared to the pure polymer.

Regarding sustainability, quantified sustainability metrics, such as carbon footprint reduction, are relevant. Reported information indicates that, on average, 1.205 kg of carbon dioxide equivalent is emitted into the atmosphere

when producing 1 kg of linear low-density polyethylene (LLDPE) [14], and the use of non-renewable energy in the production of sisal fiber is approximately 4.2 GJ/t of fiber, and greenhouse gases are approximately 270 kg of CO_2/t of fiber [15]. In a simplified way, it can be estimated that with 5% sisal, a modest reduction in emissions of approximately 0.02–0.05 kgCO_2e per kg of composite (or ~2–4%) was obtained.

Conclusion

For tensile strength, the sample prepared with POLYBOND™ 3029 showed superior performance compared to the other composites, possibly due to better adhesion at the fiber-matrix interface, resulting in more efficient load transfer. Based on the strain at break results, it was observed that the pure polymer and the composites exhibited the same mechanical performance. Thus, sisal residue can be added to LLDPE without any prior treatment, which reduces the material cost and adds value to a residue that can be used for multiple applications.

Acknowledgement

The authors are grateful to the TRL9 – LAB, Company, LAPESCA-UFBA and Brazilian Research Agency-CNPq.

References

1. Ganesan K, et al. Fatigue crack growth rate behaviour of aluminium matrix composites reinforced with hollow glass microsphere. Int J Fatigue. 2025;190.
2. Venkatesan K. Fatigue and creep behavior of abaca–sisal natural fiber–reinforced polymeric composites. Biomass Convers Biorefin. 2024;14:19961–19972.
3. FAO. Available from: https://www.fao.org/economic/futurefibres/fibres/jute/en/
4. Debabeche N, et al. Effect of fiber surface treatment on the mechanical, morphological, and dynamic mechanical properties of palm petiole fiber/LLDPE composites. Biomass Convers Biorefin. 2024;14:20699–20712.
5. Santos NV, et al. 3D printing of vegetable yarn-reinforced polymer components. J Clean Prod. 2023;415:137870.
6. Chen F, et al. Maleic anhydride-modified polyolefins as compatibilizer for lignin-reinforced polypropylene composites. Polym Compos. 2018.
7. Ustünta˘ S. Physico-mechanical characteristics of horsehair/jute fiber-based nonwoven fabric reinforced LLDPE composites: effect of alkali treatment and maleic anhydride. J Compos Mater. 2024;59:525–537.
8. Dun M, et al. Strategies for improving the strength, toughness, and winding properties of sisal fiber/polyethylene pre-preg tape. J Mater Res Technol. 2025;36:5675–5683.
9. Almomani et al. Recent advances in slow crack growth modeling of polyethylene materials. Mater Des. 2023;188:677–686.
10. De Carvalho, et al. Rice husk/poly(propylene-co-ethylene) composites: effect of different coupling agents on mechanical, thermal, and morphological properties. J Appl Polym Sci. 2012:3337–3344.
11. Amico SC. Materials Vegetable fibers as multifunctional. Revista Matéria. 2010;15:386–395.
12. D'Almeida JRM, et al. Tensile mechanical properties, morphological aspects and chemical characterization of piassava (Attalea funifera) fibers. Compos Part A Appl Sci Manuf. 2006;37:1473–1479.
13. Mokoena MA. Composites of linear low density polyethylene and short sisal fibres: the effects of peroxide treatment. J Mater Sci. 2004;39:3403–3412.
14. A decreasing footprint: a review of resin life cycle assessments. American Chemistry Council; 2020.
15. Sustainability assessment of the production of sisal fiber in Brazil. 2014.

Finite Element Analysis of a Polymeric Support with Metallic Internal Reinforcement for Carbon Steel Pipes

João Pedro Cheloni[1*], Gabriel Aelo Ribeiro[1], Adriel da Anunciação Santana[1], Lucas Lincoln Fonseca Soares[1], Francisco Ferreira de Carvalho Júnior[2]

[1]SENAI CIMATEC University, Development of Industrial Projects - DPI; Salvador, Bahia; [2]Mauari, Plastic Components Industry; Betim, Minas Gerais, Brazil

The proper storage of carbon steel pipes is a critical concern in various industrial sectors where structural integrity and corrosion resistance are essential to operational safety and longevity. Traditionally, metallic supports have been used due to their high strength. However, these supports can accelerate corrosion through galvanic coupling when in contact with carbon steel pipes, posing a significant long-term risk. To address this issue, this study investigates the feasibility of using polymeric supports internally reinforced with metallic tubes as an alternative design that maintains mechanical performance while mitigating galvanic corrosion. A methodology of numerical modeling was adopted to analyze the proposed support structures using Finite Element Analysis (FEA). Eight polymeric support models were designed, incorporating a square cross-section steel tube reinforcement, and adjusted to sustain loads of up to 8 tons. To understand the mechanical behavior of these hybrid supports, simulations were conducted with varying steel tube wall thicknesses. The failure criteria were analyzed for both metallic and polymeric materials, considering von Mises stress and maximum allowable stress values. The simulation results revealed that a minimum steel tube thickness of 8 mm is required to prevent structural failure in both the polymeric support and the metallic reinforcement. Thinner configurations led to stress concentrations that exceeded permissible limits, compromising safety. These findings underscore the necessity of tailored engineering solutions when dealing with polymeric structural elements and hybrid systems. Furthermore, the study demonstrates how the integration of informed material selection and numerical simulation can lead to safer, more cost-effective, and corrosion-resistant storage solutions for carbon steel piping systems.

Keywords: Carbon Steel Pipes. Polymeric Supports Strength. Finite Element Analysis. Failure Criteria.

Abbreviations: FEA, Finite Element Analysis; FEM, Finite Element Methods.

According to Gentil (1996) [1], a galvanic pile occurs when two metals are in contact and in the same environment. The use of traditional metallic supports for steel pipe, though robust, can accelerate pipeline corrosion due to galvanic effects, particularly in harsh environments. In this perspective, polymeric supports can be an alternative, offering advantages such as reduced weight, improved corrosion resistance, and the potential for tailored mechanical performance.

The use of polymers and composites for pipe corrosion prevention has been widely investigated in the scientific literature. Alabtah (2021) [2] demonstrated the effectiveness of fiberglass and Kevlar reinforced polymer coatings against corrosion using acids and corrosive solutions.

Farias (2016) [3] introduced the use of PA 12 in a three-layer coating system, which has high impact resistance and toughness.

To predict the mechanical behavior of this type of structure, the Finite Element Method can be used. In this method, a large problem is subdivided into smaller, simpler parts called finite elements. The simple equations that model these finite elements are then assembled into a larger system of equations that models the entire problem. The finite element method then uses techniques based on the calculus of variations to approximate a solution (for the displacement field of the geometry) by minimizing an associated error function Madier (2020) [4].

Received on 13 June 2026; revised 22 September 2026.

Address for correspondence: Milton Plinio Flores Porto. Av. Orlando Gomes, 1845 Piatã, Salvador - BA. Salvador, Bahia, Brazil. ZIP code: 41650-810. E-mail: joao.cheloni@fieb.org.br.

J Bioeng. Tech. Health 2026;9(10):1010-1015

© 2026 by SENAI CIMATEC University. All rights reserved.

This article presents a detailed analysis of the mechanical response of a polymeric support with internal metal reinforcement applied to carbon steel pipes, using three-dimensional modeling and computer simulations. The temperature at which simulations were performed was 25 °C (ambient temperature), but the influence of its variation was not investigated in this study. The objective is to validate the efficiency of the reinforcement, propose improvements in the design, and contribute to the advancement of hybrid solutions in pipeline engineering.

Materials and Methods

Materials and Geometry

In this study, eight polymeric supports internally reinforced with metallic tubes were developed. Two supports are combined to form a cradle, each designed to sustain a load of 8 tons attributed to the placement of metallic pipes above the cradle. To prevent sliding during load application, metallic plates were installed at the ends of the cradle assembly.

Figure 1 (a) illustrates the intended application of the polymeric supports in conjunction with the pipe arrangement, while Figure 1 (b) details the configuration, highlighting the eight supports, the internal reinforcement, and the steel plates at the ends. The internal reinforcing steel tube has a square cross-section of 70 × 70 mm and a wall thickness of 3 mm.

The materials employed were Nylon (PA 6) for the polymeric support and structural carbon steel for the steel tube and plates. Table 1 provides their respective properties used in this study.

Design Strategy

Figure 1. Analyzed geometry. (a) Schematic of the structure's application, and (b) CAD model of the support and reinforcement.

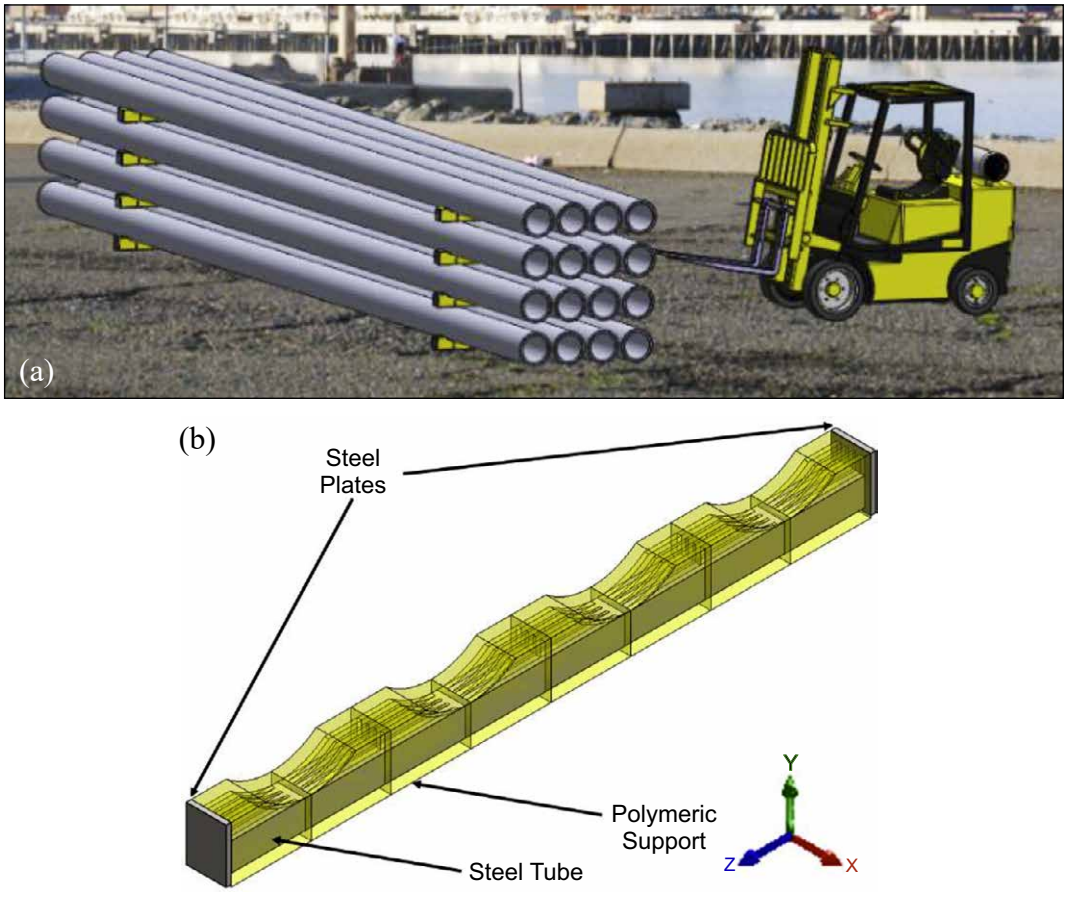

Table 1. Mechanical properties of the materials used in the analysis.

Component	Material	Elastic Modulus (GPa)	Poisson's Ratio	Yield Strength (MPa)
Polymeric Part	PA 6	0.12	0.35	43.13
Tube	Structural steel	200.00	0.30	250.00

The strategy adopted in the studies to design and simulate the components followed the flow diagram in Figure 2, and the steps taken are described in more detail below.

- Physical understanding of the problem: Understanding the physics of the problem and assessing considerations regarding the study conducted, in order to control the computational cost of the analysis.
- Geometry treatment: The geometry submitted had to be slightly modified to improve the generation of mesh elements assigned to the finite element method used.
- Assigning material properties: Definition of properties such as Modulus of Elasticity and Poisson's Ratio.
- Mesh generation: Partitioning of the continuous medium into subdomains called elements.
- Definition of contact surfaces: The analysis performed presents two bodies in contact, which requires reproducing the effects generated by this contact in the transmission of the load.
- Boundary conditions: Application of external forces and constraints of the problem.
- Analysis solution: Solving the equations that govern the previously defined numerical model using the programming language implemented in the software used.
- Analysis of results: In this step, the results obtained by the numerical model are critically studied.

Figure 2. Methodology applied in the study.

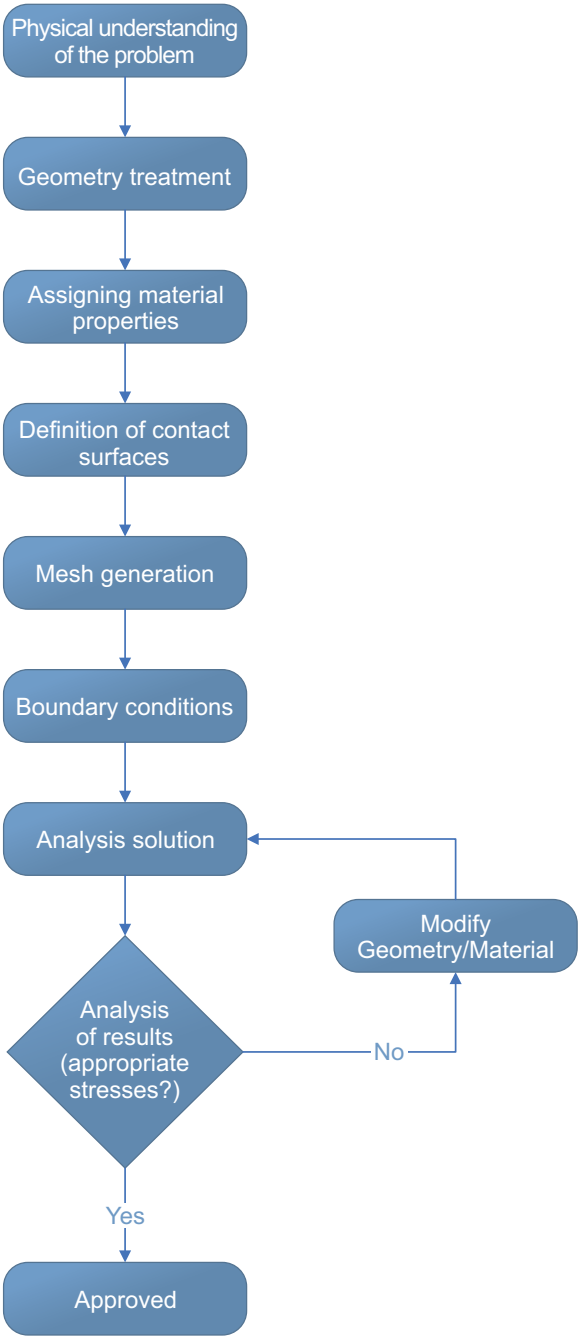

Numerical Simulation

Finite element (FE) models were developed using ANSYS Mechanical software, considering

different thicknesses for the inner steel tube, to analyze the von Mises stresses in the parts. The loads and boundary conditions were analyzed as shown in Figure 3. The load of 80 kN was applied over the upper surface of each support pair. Regarding movement constraints, displacement in the Y-direction was restricted on the bottom surface of the support simulating contact with a flat surface. Contact between the metal part and the polymer was modeled using a friction coefficient of 0.4. A mesh with 3D solid elements ranging from 1 mm to 20 mm was used to discretize the model.

Failure Criteria

The structural analyses developed are based on von Mises failure criterion for metallic materials, with stresses obtained using the Finite Element Method (FEM). A safety factor (SF) of 1.5 is adopted to account for uncertainties such as material impurities, assembly inaccuracies, and other potential defects that could lead to failure.

Accordingly, the stress-based failure criterion is defined as follows:

$$\sigma_{adm} = \frac{\sigma_{esc}}{SF} \quad (1)$$

Where σ_{adm} is the allowable stress for the problem, σ_{esc} is the material's yield strength and *SF* is the safety factor. The structure is considered structurally safe when: $\sigma_{misses} < \sigma_{adm}$ (2)

Considering yield strength for steel of 250 MPa and the specified safety factor of 1.5, the allowable stress is calculated to be 167 MPa.

Therefore, for a geometry to be approved, the von Mises stress (σ_{misses}) obtained from the simulations must not exceed this value.

The failure criterion for the polymeric material is given by Equation 3 according to Erhard (2006) [5]. This equation establishes the maximum permissible stress σ_{perm} given by:

$$\sigma_{perm} = \frac{K}{S} \cdot \frac{1}{A_T} \cdot \frac{1}{A_{st}} \cdot \frac{1}{A_{dyn}} \cdot \frac{1}{A_A} \cdot \frac{1}{A_W} \quad (3)$$

Where K (43.4 MPa) is characteristic strength, S (1.3) is safety factor for a 0.5% strain limit, A_T (1.0) is temperature factor, A_{st} (1.3) is static load factor, A_{dyn} (1.3) is dynamic load factor, A_A (1.0) aging factor and A_w (1.0) is water absorption factor.

Applying these parameters to Equation 3 results in a maximum permissible stress for the polymer of 19.71 MPa.

Figure 3. Loads and boundary conditions.

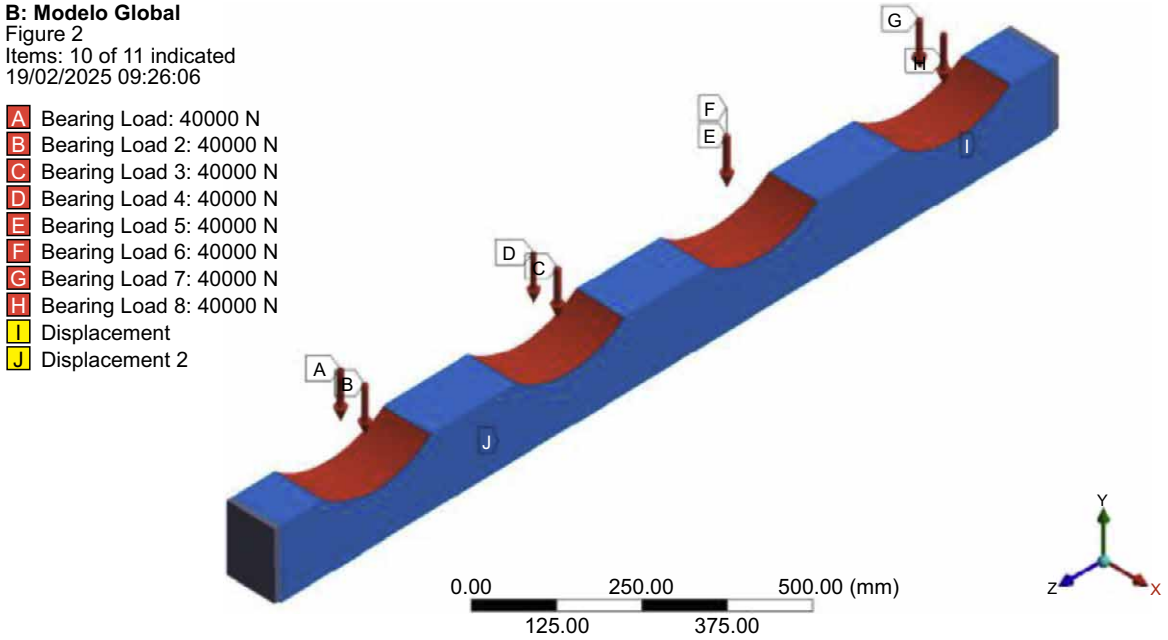

Results and Discussion

The results from the initial analysis are available in Figure 4. With a 3 mm-thick tube for reinforcement of the polymeric part, the maximum stress is way beyond the admissible 167 MPa as mentioned before in section 2.4.

Figure 4. Results from analysis of the assembly - 3 mm thick steel tube reinforcement: (a) Stresses in the tube reinforcement and (b) Stresses in the polymeric part.

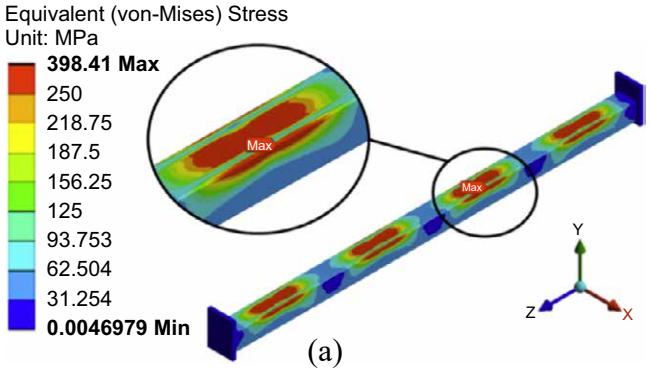

(a)

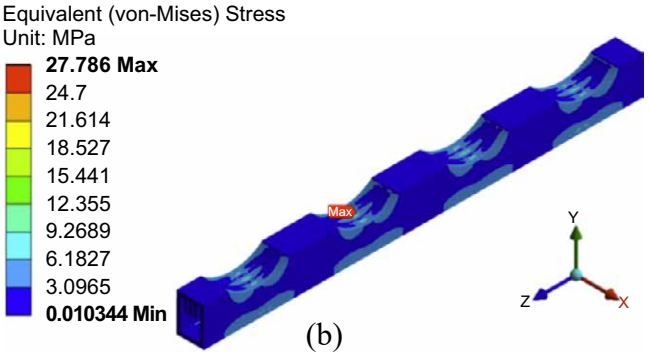

(b)

It was noted that most of the load is handled by the steel tube. The hypothesis that increasing the stiffness of the tube (i.e. increasing its thickness) would lead to a consequent decrease in the polymeric part stresses was tested. Table 2 summarizes the results obtained from analyses performed with varying tube thickness.

While the new analyses were being performed, the need to refine the mesh was identified. To save computational time, an approach of studying just a piece of the model was adopted since, as can be seen from the results of Figure 4, the behavior of the entire component follows a pattern. Figure 5 shows the boundary conditions adopted for the new studies.

Table 2. Analysis results from the variation of tube thickness.

Tube Thickness (mm)	Max. stresses in polymeric parts (MPa)	Max stresses in tube (MPa)
3	27.786	398.41
4.75	23.267	217.17
6.3	19.501	223.7
8	18.159	158.72

For the last result in Table 2, the approval criteria were met and the stress and displacement plots can be seen in Figure 6 (for the internal reinforcement) and Figure 7 (for the polymeric part).

Figure 5. New model for mesh refinement.

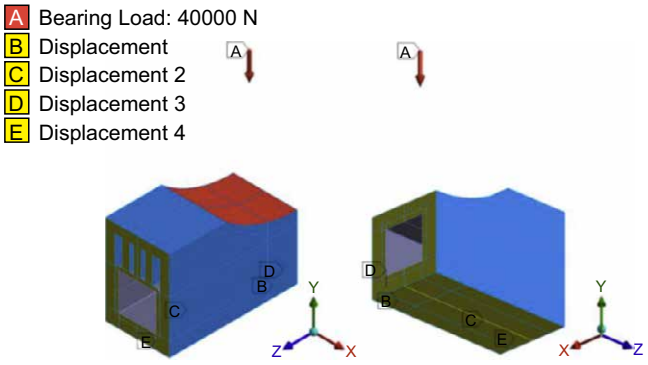

Figure 6. Analysis results for the internal reinforcement (with 8 mm thickness): (a) Total Displacement and (b) Von Mises Stresses.

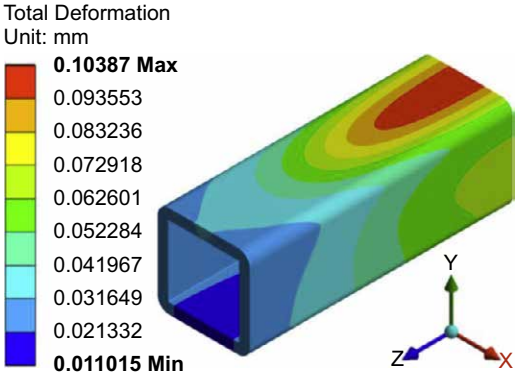

(a)

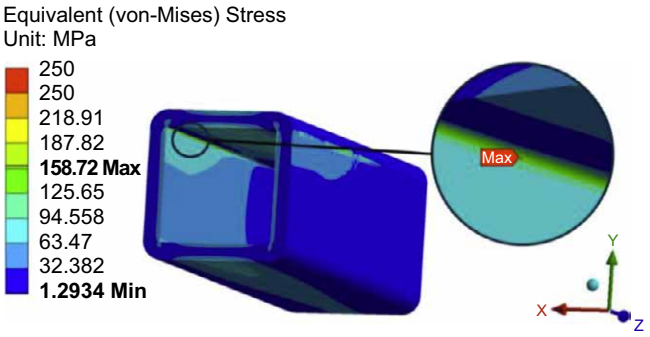

(b)

Figure 7. Analysis results for the polymeric part: (a) Total Displacement and (b) Von Mises Stresses.

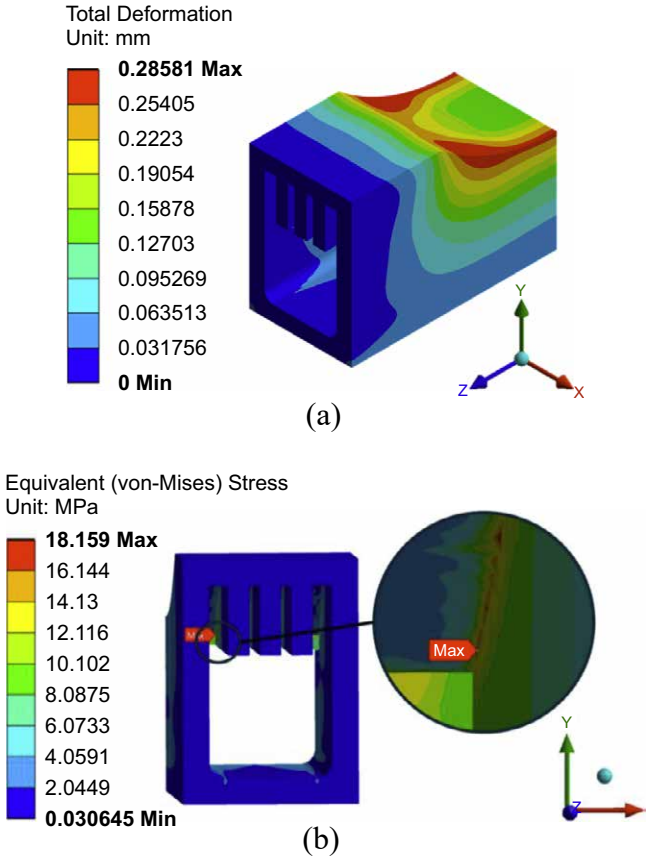

(a)

(b)

Conclusion

In this work, the geometry of a polymeric support reinforced internally with a metallic tube made from steel was investigated in terms of its structural strength. Initially, the 3 mm-thick steel tube was not enough to handle the load, causing failure in the polymeric support as well. Analysing the results globally, it was perceived that as the thickness of the tube was increased, the stresses in both parts decreased.

However, confronting the results of the maximum stresses in the component with 6.3 mm thick tube against the one with 4.75 mm, a slight increase of 3% occurred. This can be explained by the mesh refinement made in the studies from the 6.3 mm case onward, which converged the stresses and revealed some local effects not captured by the previous analysis.

As a final output from the analysis, it was possible to verify that the support can withstand the load applied if it is reinforced with an 8 mm-thick tube.

References

1. Gentil V. Corrosão. Rio de Janeiro: LTC – Livros Técnicos e Científicos Editora S.A.; 1996.
2. Alabtah FG, et al. Towards the Development of Novel Hybrid Composite Steel Pipes: Electrochemical Evaluation of Fiber-Reinforced Polymer Layered Steel against Corrosion. Qatar; 2021.
3. Farias CA, et al. Polyamide 12 in Extruded Coating Systems for Steel Pipe Protection. Búzios: ABRACO; 2016.
4. Madier D. Practical Finite Element Analysis for Mechanical Engineers. Canada: FEA Academy; 2020.
5. Erhard G. Designing with Plastics. Cincinati: Hanser Gardner Publications; 2006.

Process Parameters Investigation of Lignin Content in Residual Biomass

Davi Vieira Rosa[1*], Diana Catalina Cubides Roman[2], Paulo Victor Rocha Brandao[2]
[1]SENAI CIMATEC University, Chemistry, Petrochemistry, and Biotechnology; [2]SENAI CIMATEC University, Chemical Department, Petrochemical, and Refining Processes; Salvador, Bahia, Brazil

The pulping stage is critical for lignin removal in lignocellulosic biomass, directly influencing the efficiency of subsequent stages. In the case of residual biomass from already established production chains, its use represents a strategic alternative to add value to byproducts and reduce environmental liabilities. This exploratory study evaluated the influence of sodium hydroxide concentration and solid-to-liquid ratio on the residual lignin content. Trials were conducted at 80 °C for one hour, using NaOH at 4%, 8%, and 16%, with fiber-to-solution ratios of 1:10 and 1:20. Agitation was controlled and standardized for all samples, ensuring homogeneous mixing. Lignin quantification was performed using the Kappa number method (TAPPI T 236 om-22). The condition of 4% NaOH and a 1:20 ratio presented the lowest Kappa number, indicating high efficiency with lower reagent consumption. The results guide the definition of operational parameters that combine performance with rational use of inputs.

Keywords: Lignin. Pulping. Biomass. Kappa Number.

Abbreviations: NaOH – sodium hydroxide; $KMnO_4$ – potassium permanganate.

Lignocellulosic biomass is primarily composed of cellulose, hemicelluloses, and lignin, along with small fractions of extractives and minerals [1]. Cellulose is a fibrous polysaccharide with high crystallinity that provides mechanical strength; hemicelluloses are amorphous polymers that contribute to matrix flexibility; and lignin acts as a binding agent, imparting rigidity and impermeability to cell walls. This complex structure ensures plant stability but hinders separation processes and industrial utilization [2]. Proportions of these constituents vary according to plant species, age, and growth conditions, directly impacting the selection and optimization of treatments.

When this biomass originates from residues of other industrial processes, as in the case of this study, its utilization represents a strategic opportunity within the concept of a circular economy. The use of residual biomass reduces the need for virgin raw materials, mitigates the environmental impacts associated with disposal, and adds value to underutilized streams, aligning production with more sustainable practices [4].

Lignin, in particular, represents a physical and chemical barrier to reagent penetration, making its removal essential for fiber liberation. Pulping aims to break this barrier. It is one of the key stages

Figure 1. Arrangement of cellulose, hemicellulose, and lignin in plant cell walls.

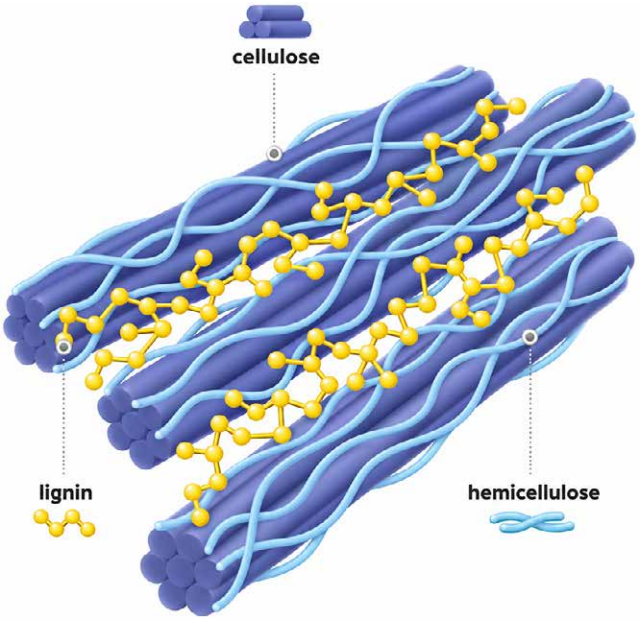

Source: Adapted from Hosokawa Alpine Group 2025 [3].

Received on 18 June 2026; revised 15 September 2026.
Address for correspondence: Davi Vieira Rosa. Av. Orlando Gomes, 1845 Piatã, Salvador - BA. Salvador, Bahia, Brazil. ZIP code: 41650-810. E-mail: davieiros@gmail.com.

J Bioeng. Tech. Health 2026;9(10):1016-1020
© 2026 by SENAI CIMATEC University. All rights reserved.

in the processing of lignocellulosic biomass, being responsible for fiber separation and lignin removal, with a direct impact on pulp quality and the performance of subsequent processes. In non-woody biomass, chemical composition and anatomical structure differ significantly from those of traditional woods, requiring the adaptation of operational parameters [1].

To evaluate lignin removal efficiency, the Kappa number is commonly employed. This method, based on oxidation titration, indirectly quantifies the fraction of residual lignin in the pulp. The reaction occurs predominantly with lignin but may also involve other non-lignin structures containing carbonyl groups or double bonds, such as α,β-unsaturated aldehydes and α-ketocarboxylic acids, which likewise consume potassium permanganate ($KMnO_4$) in an acidic medium [5]. Under specific conditions, the formation of oxidizable byproducts, such as hexenuronic acids (HexA), may contribute to an increase in the measured value, since they also react with the oxidant. Thus, although traditionally used in the pulp industry to estimate lignin content and determine reagent charges for subsequent stages, the Kappa number reflects the overall oxidant consumption by lignin and other compounds present in the biomass, providing a comprehensive indicator of pulp condition.

In this study, we investigated the influence of NaOH concentration and solid-to-liquid ratio on the reduction of lignin content, in a non-conventional lignocellulosic biomass, determined by the Kappa number, focusing on defining more efficient and economically viable conditions.

Materials and Methods

Pulping

Pulping was carried out at 80 °C for one hour, using different sodium hydroxide concentrations (4%, 8%, and 16%) and solid-to-liquid (s/l) ratios of 1:10 and 1:20. The biomass used was previously dried to a moisture content of approximately 15%, milled, and sieved through a 40-mesh screen to standardize particle size. The process consisted of heating and controlled, standardized agitation for all samples, sufficient to maintain a homogeneous mixture throughout the treatment. After draining the black liquor, an intermediate washing of the fibers with distilled water was performed to remove liquor residues and prepare the sample for subsequent stages.

Kappa Number Determination

The residual lignin content was estimated using the Kappa number method (ANSI/TAPPI T 236 om-22). This titration method indirectly quantifies lignin by measuring the consumption of potassium permanganate ($KMnO_4$) in an acidic medium. Initially, the sample is weighed considering its moisture content and mechanically dispersed in distilled water to ensure complete fiber separation. Subsequently, 4N sulfuric acid is added to provide the acidic conditions required for the reaction, followed immediately by the addition of a 0.1N $KMnO_4$ solution. The mixture is kept under constant stirring for 10 minutes. The reaction is then stopped by adding 1N potassium iodide solution, which releases iodine proportional to the remaining permanganate. This iodine is titrated with 0.1N sodium thiosulfate until a pale-yellow color is reached, at which point a starch solution is added as an indicator. The titration continues until the disappearance of the blue color, indicating the endpoint. The Kappa number calculation considers the volume of reagent consumed, its normality, the dry mass of the sample, and temperature and calibration correction factors.

$$K = \frac{p * f}{w} = \frac{f * (b - a) * N}{w * 0.1} \quad (1)$$

The parameters used in Equation (1) are defined as follows: K represents the Kappa number (dimensionless); f is the correction factor for 50% permanganate consumption (dimensionless); w is the oven-dried pulp weight of the specimen, expressed in grams (g); p corresponds to the volume of 0.1 N potassium permanganate actually consumed by the test specimen, in milliliters (mL);

b is the volume of sodium thiosulfate consumed in the blank determination, in milliliters (mL); a is the volume of sodium thiosulfate consumed by the test specimen, also in milliliters (mL); and N is the normality of the sodium thiosulfate solution (N).

Results and Discussion

Solid-to-Liquid Ratio 1:10

It was observed that the Kappa numbers remained higher under this condition, with variations among concentrations indicating a partial reduction when the NaOH content was increased. Table 1 presents the Kappa number values and the percentage of residual lignin obtained for the 1:10 ratio at all concentrations evaluated.

Table 1. NaOH concentration – Kappa number and residual lignin (1:10 S/L).

NaOH Concentration (w/v)	Kappa Number	% Residual Lignin
4%	64.45	9.7
8%	67.67	10.2
16%	78.89	11.8

It is evident that the decrease in Kappa number with increasing NaOH concentration does not follow a linear relationship. Between 4% and 8%, there is a more pronounced drop, attributed to the greater availability of OH^- ions to break ester and ether bonds between lignin and carbohydrates. Above 8%, the effect becomes less significant, possibly due to the saturation of the liquor with reaction products, reducing the chemical gradient necessary for diffusion. Thus, the magnitude of the decrease was modest, suggesting that liquor availability was a limiting factor for hydroxide ion diffusion and for the solubilization of lignin and hemicelluloses. This effect is consistent with scenarios in which the liquor rapidly becomes saturated with extractives and solubilized products, reducing concentration gradients and hindering further lignin removal. Figure 2 shows the behavior of these values as a function of alkaline concentration.

The percentage of residual lignin presented in tables and figures is inversely related to the efficiency of the pulping process. Higher values indicate lower lignin removal during treatment, as they represent a greater fraction of the component remaining in the biomass, which translates into poorer performance in the delignification stage. Lower percentages of residual lignin reflect more efficient conditions and favor subsequent processes.

In addition, the Kappa reading may have been influenced by the formation of non-lignin oxidizable species. Nevertheless, the overall trend observed in Figure 2 confirms that increasing NaOH improves the response up to a point at which further gains become negligible under the 1:10 ratio, as shown by the near-asymptotic profile of the graph.

Figure 2. Residual lignin (%) for different NaOH concentrations (1:10 S/L).

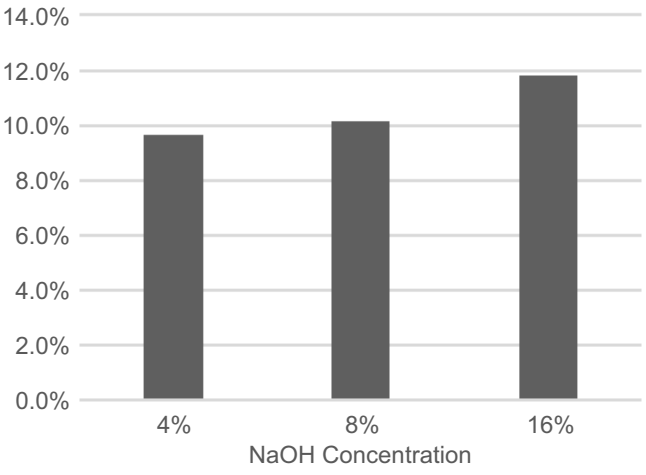

Solid-to-Liquid Ratio 1:20

For the 1:20 solid-to-liquid ratio condition, it was observed that the Kappa number was consistently reduced, and consequently, the percentage of residual lignin, when compared to the previous condition. This is evidenced in Table 2.

Table 2. NaOH concentration – Kappa number and residual lignin (1:20 S/L).

NaOH Concentration (w/v)	Kappa Number	% Residual Lignin
4%	49.09	7.4
8%	51.62	7.7
16%	56.05	8.4

The condition with 4% NaOH stands out not only for presenting the lowest Kappa number in the entire study but also for achieving results very close to those obtained at higher concentrations, despite using the smallest amount of reagent, as shown in Figure 3. This reinforces its advantage both in terms of efficiency and reagent economy. At higher concentrations, the additional gains were limited, possibly due to the formation of oxidizable groups that also consume permanganate during titration.

As in the 1:10 ratio, an inverse relationship between residual lignin and pulping efficiency is also observed here, but with slightly more favorable results. In other words, lower percentages of lignin indicate more effective removal, while higher values signal lower efficiency in the delignification stage. This pattern reinforces that liquor availability plays a central role in process effectiveness and prepares the pulp for subsequent stages such as bleaching and hydrolysis.

Figure 3. Residual lignin (%) for different NaOH concentrations (1:20 S/L)

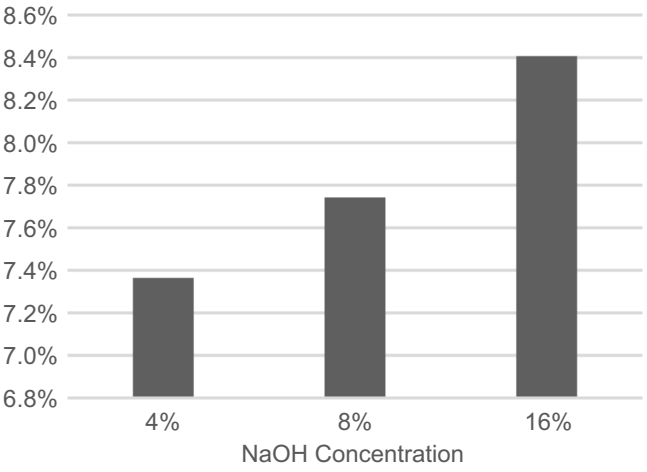

A combined analysis of the Kappa numbers and residual lignin percentages shows that, although both solid-to-liquid ratios present a tendency toward reduced values as alkaline concentration increases, the 1:20 ratio stands out for achieving lower levels of residual lignin without the need for extreme NaOH concentrations. This performance reinforces that adjusting liquor availability can be as or more effective than simply increasing the alkaline charge, since the larger solution volume favors hydroxide ion diffusion, lignin solubilization, and the removal of other compounds present in the biomass. Compared with the 1:10 ratio, the 1:20 ratio showed consistent reductions in the Kappa number at all concentrations evaluated, demonstrating that increasing liquor volume provides a less saturated reaction medium and maintains delignification reaction efficiency for longer.

Furthermore, it is noted that, beyond a certain point, increasing alkaline concentration results in more limited gains, indicating the existence of a technical limit at which excess reagent does not translate into a proportional increase in lignin removal. These findings reinforce the importance of balancing the solid-to-liquid ratio and NaOH concentration, seeking conditions that maximize efficiency without waste of inputs, with direct implications for the optimization of industrial processes aimed at reducing operational costs and environmental impacts.

Conclusion

The condition of 4% NaOH and a 1:20 solid-to-liquid ratio balances efficiency and reagent economy, making it the most promising. The solid-to-liquid ratio exerts a strong influence on delignification, and the gains from increasing alkaline concentration become limited beyond a certain point. It is recommended that future studies explore complementary methods to quantitatively confirm these results, assess the economic impact of reagent use, and extend the study to other biomasses, thereby consolidating robust

parameters. It is also important to explore other temperatures and pressures in the pulping process.

Acknowledgement

We thank SENAI CIMATEC for the technical support and infrastructure that enabled the execution and analysis of this study, Embrapii, Green Coco Europe GmbH and Dicoco Agroindustrial for the financial support and fiber supply, and the project team for conducting the experiments and analyzing the results.

References

1. Poornachandra C, Jayabalakrishnan RM, Balasubramanian G, Lakshmanan A, Selvakumar S, Maheswari M, et al. Coconut husk fiber: a low-cost bioresource for the synthesis of high-value nanocellulose. Biomaterial Research in Applied Chemistry. 2023;13(6):504.
2. Pirah S, Wang X, Javed M, Simair K, Wang B, Sui X, et al. Lignocellulose extraction from sisal fiber and its use in green emulsions: a novel method. Polymers (Basel). 2022;14(11):2299.
3. Hosokawa Alpine Group. Lignin [Internet]. Available from: https://www.hosokawa-alpine.com/powder-particle-processing/industries/chemicals/lignin
4. Forcelini F, Domingos AN, Carneiro LM. Fibras naturais vegetais e desenvolvimento sustentável: extração, beneficiamento e aplicação no design de produtos [Plant-based natural fibers and sustainable development: extraction, processing, and application in product design]. In: Anais do 13º Encontro de Sustentabilidade em Projeto (ENSUS 2025); 2025; Florianópolis, Brasil. Florianópolis: Universidade Federal de Santa Catarina; 2025.
5. Correia FM, D'Angelo JVH, Silva Júnior FG. Revisitando número kappa: conceitos e aplicações na indústria de celulose [Revisiting the Kappa number: concepts and applications in the pulp industry]. O Papel. 2019 Jul;80(7):77-89.
6. TAPPI. T 236 om-22: Kappa number of pulp. Atlanta (GA): Technical Association of the Pulp and Paper Industry; 2022.

Circular Innovation in Technical Education: A Design Thinking-Based Pedagogical Practice Using Reused Materials

Clariane Teixeira Pessoa Mamona[1*], Pietro Carlos Gonçalves Conceição[2]
[1]SENAI CIMATEC University, NEPE; Salvador, Bahia, Brazil

This paper presents a pedagogical practice developed with technical education students, aiming to foster sustainability, creativity, and social engagement through the reuse of disposable materials in the construction of functional objects. The activity was structured around the five stages of Design Thinking, providing students with an active, problem-centered learning experience. Throughout the process, students transformed solid waste—such as PET bottles and cardboard—into toys and utensils, combining technical knowledge, ecological awareness, and innovation. The project culminated in an exhibition open to the institution's internal public, during which students showcased their prototypes and explained their creative solutions. Simultaneously, a solidarity initiative was promoted through the collection of non-perishable food items for donation to a local charity. The results indicate that the adopted approach significantly contributed to the development of socio-environmental competencies and to the advancement of the Sustainable Development Goals, highlighting the potential of interdisciplinary pedagogical strategies in strengthening both technical and civic education. The experience proved to be low-cost, replicable, and highly effective in integrating theory, practice, and social responsibility.

Keywords: Pedagogy. Recycling. Sustainability. Innovation. Prototyping.

The global environmental crisis, intensified by rampant consumption and improper disposal of solid waste, has heightened the demand for educational practices that promote sustainability and circular economy principles. In this context, education plays a strategic role in forming critical and conscious citizens capable of proposing innovative solutions to contemporary socio-environmental challenges [1,2].

Among the most promising strategies is the use of disposable materials in practical and creative pedagogical activities. Transforming solid waste into functional objects—such as toys, artworks, or technological devices—not only reduces environmental impact but also fosters creativity, autonomy, and critical thinking [3,4]. Such practices have been successfully integrated across educational levels, from basic to technical and higher education, promoting both material reuse and meaningful learning. Studies indicate that recycling workshops—including those reusing 3D printing waste—develop technical and entrepreneurial skills while engaging students in circular economy logic [5]. In design and engineering, active methodologies such as Industry 4.0 technologies demonstrate the potential of Education for Sustainable Development (ESD) to change behaviors [6]. Furthermore, educational experiences focused on upcycling and green prototyping positively impact students' environmental attitudes, strengthening ecological awareness and social engagement [7]. Integrating sustainable practices into technical curricula enables students to act as transformative agents, connecting theory and practice through projects that combine creativity, socio-environmental responsibility, and innovation [8]. The Design Thinking methodology, a human-centered and iterative approach, offers a structured framework for tackling such complex problems. By following its stages—empathize, define, ideate, prototype, and test—students engage in a hands-on process that fosters empathy, collaboration, and innovative solution development [9].

Received on 9 June 2026; revised 6 September 2026.
Address for correspondence: Clariane Teixeira Pessoa Mamona. Av. Orlando Gomes, 1845 Piatã, Salvador - BA. Salvador, Bahia, Brazil. ZIP code: 41650-810. E-mail: clariane.pessoa@fieb.org.br.

J Bioeng. Tech. Health 2026;9(10):1021-1025
© 2026 by SENAI CIMATEC University. All rights reserved.

This paper presents a pedagogical practice developed with technical education students, structured around the Design Thinking framework. The objective of this work was to promote sustainability, creativity, and social engagement through the transformation of disposable materials like PET bottles into functional objects. This approach encouraged ecological awareness, innovative thinking, and active learning. Aligned with circular economy principles and the Sustainable Development Goals (SDGs), the proposal integrated education, innovation, and social responsibility into a practical and meaningful experience.

Materials and Methods

The methodology of this study was based on the principles of Design Thinking, a human-centered approach that encourages creative problem-solving through an iterative and collaborative process [9].

The proposed activity involved the construction of functional objects or toys from disposable materials (with emphasis on plastics, such as PET bottles), combined with a solidarity initiative to collect non-perishable food items. The activity was structured around the five stages of Design Thinking: Empathize, Define, Ideate, Prototype, and Test, as illustrated in Figure 1.

Stage 1 – Empathize

The initial stage aimed to raise student awareness across two complementary dimensions:

- Environmental awareness: By proposing the reuse of disposable materials, students were encouraged to reflect on the environmental impact of consumption and waste, as well as on the principles of the circular economy.
- Social solidarity: The voluntary donation of one kilogram of non-perishable food fostered empathy with vulnerable communities,

Figure 1. Design Thinking stages applied to the pedagogical practice.

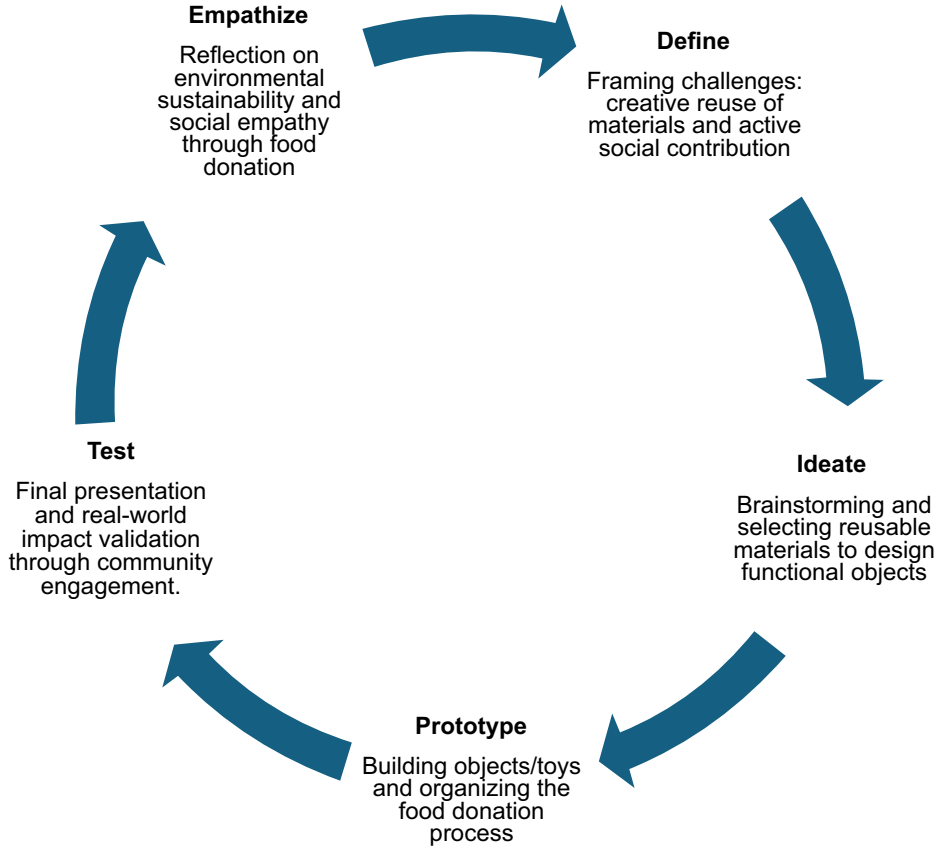

encouraging civic engagement and collective responsibility.

Stage 2 – Define

Based on the initial reflections, two core challenges were defined:

- Ecological challenge: "How can we transform waste into functional objects or creative toys, adding value and extending their life cycle?"
- Social challenge: "How can we contribute to a charity institution through the collection and donation of food?"

These challenges guided the following stages, even if not explicitly framed as formal problem statements.

Stage 3 – Ideate

At this stage, students were invited to freely explore ideas based on the materials available:

- They conducted brainstorming sessions on transformation possibilities, considering functional, aesthetic, and social aspects.
- They generated multiple design alternatives and selected the most feasible idea for implementation.
- Creative freedom was essential to stimulate divergent thinking and innovation.

Stage 4 – Prototype

Prototyping was carried out through:

- The physical construction of the objects/toys, applying manual skills and basic techniques for assembling, cutting, and adapting reused materials.
- The organization of the food donations, also treated as a symbolic prototype of a concrete act of solidarity.

During this stage, students encountered and solved real execution challenges, such as ensuring structural stability and adapting shapes.

Stage 5 – Test

Finally, the validation of the prototypes occurred through practical activities:

- In-class presentations, during which peers and the instructor assessed creativity, functionality, and aesthetics.
- Real use of the toys, which were donated to children in a charity institution—serving as a field test in an authentic context.
- Delivery of food donations, completing the social impact cycle and reinforcing the collective value of the actions developed.

Results and Discussion

The culmination of the project took place through an interactive exhibition of the toys and functional objects created by students using reusable materials such as PET bottles, cardboard, plastic caps, and fruit nets. The exhibition was held in an internal circulation area of the institution, ensuring high visibility and promoting spontaneous engagement from students, teachers, and passersby.

As illustrated in Figure 2, the diversity and quality of the presented items were noteworthy: board games, stylized cars, airplanes, lanterns, and various toys were crafted with creativity and technical skill. The reuse of materials that would otherwise be discarded not only demonstrated students' manual and technical abilities but also fostered socio-environmental competencies such as ecological responsibility and innovative thinking. This aligns with the findings of Siqueira and Arrial [4], who highlighted how the creation of toys from solid waste serves as a powerful tool to stimulate creativity and environmental commitment among elementary school children.

The exhibition was designed as a space for dialogue and student protagonism. During the event, students were responsible for presenting their creations, explaining the materials used, the construction process, and the challenges faced during prototyping. This approach reinforced active learning and oral communication while also encouraging critical thinking about consumption, waste, and reuse—core elements for fostering circular citizenship and environmental responsibility [1,2].

Figure 2. Exhibition of objects produced by students using reusable materials.



In addition to its pedagogical focus, the project was enriched by a solidarity initiative: a collection box was placed beside the exhibition to gather non-perishable food items. The integration of environmental practice with social action gave the activity a broader formative dimension, promoting empathy, citizenship, and collective responsibility—a strategy aligned with sustainable education principles oriented toward community engagement and behavioral change. Nagatomo [6] similarly advocates for the integration of circular economy strategies with open technologies and social action. The exhibition and food collection represented the final stages of the Design Thinking process: testing and validation. The "test" phase was fulfilled through the presentation of the prototypes to the school community and the reception of direct feedback. The "validation" occurred both through the functional success of the objects and the social impact generated by the donations. This experience resonates with the work of Flowers and colleagues [7], who emphasized how practical activities using post-consumer waste can foster not only technical development but also shifts in attitudes toward sustainability. The experience also aligned with circular economy principles by giving new life to materials regarded as waste. This perspective echoes Bremgartner and colleagues (2024), who describe how educational workshops involving 3D printing waste contribute to cultivating a sustainable maker mindset and promoting material reuse as both an educational and ecological strategy [5].

By transforming discarded items into useful products, students demonstrated that sustainable innovation can be implemented in everyday school settings with low cost and high educational value. This finding is supported by Çebi [3], who shows how the reuse of materials in art education enhances not only creative expression but also a broader aesthetic and ecological awareness.

Conclusion

The pedagogical experience described in this study proved to be an effective strategy for integrating the concepts of sustainability, circular economy, and active learning within the context of technical education. By transforming waste into functional objects while simultaneously engaging in socially impactful actions, students were encouraged to reflect on their role as agents of change, promoting values such as empathy, environmental responsibility, and creativity.

The method based on Design Thinking proved appropriate for structuring the activity, as it allowed students to experience all stages of the creative process—from identifying challenges to delivering tangible solutions. The exhibition of prototypes and the solidarity initiative contributed to the consolidation of learning and strengthened

the bond between school and community, expanding the scope of traditional technical training.

The proposed practice was shown to be replicable, low-cost, and highly didactic, standing out as a promising approach for interdisciplinary teaching and for promoting the Sustainable Development Goals (SDGs) within educational practices.

Acknowledgement

The authors would like to express their sincere gratitude to University SENAI CIMATEC for the institutional support and for fostering an educational environment that encourages innovation, sustainability, and social responsibility. This work was made possible thanks to the infrastructure and encouragement provided by the institution, which continuously promotes interdisciplinary and impactful teaching practices.

References

1. Kosta AD, Keramitsoglou KM, Tsagarakis KP. Circular economy and sustainable development in primary education. Frontiers in Sustainability 2025;6. https://doi.org/10.3389/frsus.2025.1414055.
2. Nguyen TPL. Integrating circular economy into STEM education: A promising pathway toward circular citizenship development. Front Educ (Lausanne) 2023;8. https://doi.org/10.3389/feduc.2023.1063755.
3. Çebi S. From Waste to Art: A Study on Student Creativity and Creative Expression through Recycled Materials in Art Education. Art Vision 2025;31:59–70. https://doi.org/10.32547/artvision.1542477.
4. Siqueira V, de Arrial L. Educação ambiental através da reutilização de resíduos sólidos para a elaboração de brinquedos. Revista Thema 2018;15:927–42. https://doi.org/10.15536/thema.15.2018.927-942.865.
5. Bremgartner JL, Bremgartner V, Manzatol L, Santos J. Promovendo a sustentabilidade por meio de uma oficina de reciclagem de resíduos de impressão 3D. Revista Ibero-Americana de Estudos Em Educação 2024;19:e024064.https://doi.org/10.21723/riaee.v19iesp.1.18341.
6. Nagatomo D. Research on Education for Sustainable Development with Design-Based Research by Employing Industry 4.0 Technologies for the Issue of Single-Use Plastic Waste in Taiwan. Sustainability 2024;16:9832. https://doi.org/10.3390/su16229832.
7. Flowers J, Rauch C, Wierzbicki A. Teaching Upcycling to Impact Environmental Attitudes. Journal of Technology Education 2019;30:30–45. https://doi.org/10.21061/jte.v30i1.a.2.
8. Chatzopoulos A, Tzerachoglou A, Priniotakis G, Papoutsidakis M, Drosos C, Symeonaki E. Using STEM to Educate Engineers about Sustainability: A Case Study in Mechatronics Teaching and Building a Mobile Robot Using Upcycled and Recycled Materials. Sustainability 2023;15:15187. https://doi.org/10.3390/su152115187.
9. Brown T. Design Thinking. 2008.

Overview of Physical Channel Modeling in CV-QKD Systems

Davi Juvêncio Gomes de Sousa[1*], Nelson Alves Ferreira Neto[1]
[1]QuIIN - Quantum Industrial Innovation, EMBRAPII CIMATEC Competence Center in Quantum Technologies, SENAI CIMATEC University; Salvador, Bahia, Brazil

Continuous-Variable Quantum Key Distribution (CV-QKD) is a promising solution for secure quantum communication, offering compatibility with standard optical components and potential for high key generation rates. However, practical deployments face critical challenges due to imperfections in the physical communication channel. These include optical attenuation, excess noise, polarization disturbances, residual phase noise, and crosstalk from coexisting classical channels, all of which impact the system's secure key rate (SKR). This work provides a comprehensive analysis of physical channel modeling in CV-QKD systems, focusing on how different models capture transmittance degradation and excess noise. We begin with the standard lossy bosonic channel and extend the discussion to more specific models addressing polarization effects, nonlinear interference in DWDM networks, phase fluctuations in LLO-based architectures, propagation impairments in free-space optical (FSO) links, and modulation-induced distortions, including discretized Gaussian modulation and multi-carrier OFDM schemes. We further examine the limitations and applicability of these models in realistic scenarios, considering finite-size effects, time-varying channel conditions, and calibration inaccuracies. These insights contribute to the development of more accurate security analyses and performance optimization strategies for CV-QKD systems deployed in practical environments.
Keywords: Physical Channel Modeling. Quantum Communication Channels. Continuous-Variable Quantum Key Distribution.

The security of modern communications, traditionally based on the computational hardness of mathematical problems, faces a critical challenge with the advent of quantum computing and algorithms such as Shor's algorithm [1]. In this emerging context, Quantum Key Distribution (QKD) has become a foundational technology, offering information-theoretic security grounded in the fundamental principles of quantum mechanics, particularly the Heisenberg Uncertainty Principle and the No-Cloning Theorem [2].

QKD enables two legitimate parties, commonly referred to as Alice and Bob, to establish a shared secret key that can subsequently be used for encrypted communication with perfect secrecy, such as through the One-Time Pad protocol [3,4].

Received on 17 June 2026; revised 20 September 2026.
Address for correspondence: Davi Juvêncio Gomes de Sousa. Av. Orlando Gomes, 1845 Piatã, Salvador - BA. Salvador, Bahia, Brazil. ZIP code: 41650-810. E-mail: juvencio@fieb.org.br.

J Bioeng. Tech. Health 2026;9(10):1026-1032
© 2026 by SENAI CIMATEC University. All rights reserved.

Among the various QKD implementations, Continuous-Variable Quantum Key Distribution (CV-QKD) has received considerable attention [5]. Unlike discrete-variable QKD (DV-QKD), which typically requires single-photon detectors—often costly and inefficient—CV-QKD encodes information in the continuous quadratures of the optical field (e.g., amplitude and phase), leveraging coherent detection methods compatible with commercially available optical components [4]. This compatibility offers several practical advantages, including high quantum efficiency, the potential for elevated secret key rates over short distances, and the ability to coexist with classical communication systems on a single fiber through Wavelength Division Multiplexing (WDM) [6].

The robustness and practical performance of a CV-QKD system are critically dependent on the accuracy of the physical channel model and the effectiveness of strategies for mitigating the imperfections introduced by the channel [7]. The coherent optical channel—whether implemented via fiber or free-space optics (FSO)—is inherently non-ideal and introduces various disturbances

that can adversely affect the Secure Key Rate (SKR), thereby compromising the system's security [4,6].

This paper aims to present a comprehensive analysis of physical channel models used in CV-QKD systems, with a particular focus on coherent optical communication channels. We investigate how different physical and mathematical formalisms describe the behavior of these channels, accounting for critical effects such as attenuation, thermal noise, Gaussian excess noise, and optical losses. Furthermore, the study evaluates the capacity of these models to effectively capture and manage such imperfections, thereby providing a solid theoretical foundation for the design and optimization of practical CV-QKD systems.

Coherent Optical Channels in CV-QKD

At the core of Continuous-Variable Quantum Key Distribution (CV-QKD) lies the encoding of secret information onto the quadratures of a quantum state of light, typically coherent states that resemble high-quality laser light [8]. The most widely studied encoding scheme is Gaussian Modulated Coherent States (GMCS), in which the position ($\hat{X}$) and momentum ($\hat{P}$) quadratures follow a Gaussian distribution with zero mean and variance V_A [9].

To decode these states, the receiver (Bob) employs coherent detection techniques—namely, homodyne or heterodyne detection [2]. Both methods require a strong local oscillator (LO) to interfere with the weak quantum signal, amplifying it and enabling quadrature measurements limited only by shot noise [8]. The method by which the LO is delivered to the receiver represents a critical architectural choice in system design.

Transmitted Local Oscillator (TLO)

In the TLO scheme, the LO is generated by Alice and transmitted alongside the quantum signal over the same public optical channel. This approach ensures phase stability between the signal and LO, which is essential for coherent detection [10,11]. However, transmitting a strong classical LO introduces potential security vulnerabilities. Notably, it enables side-channel attacks such as LO calibration attacks or manipulations of the LO's intensity and polarization, which adversaries can exploit to extract information or destabilize the system [10].

Local Local Oscillator (LLO)

In contrast, the LLO scheme generates the LO locally at Bob's side using an independent laser [9]. This architecture eliminates the attack surface associated with LO transmission, making it more secure and suitable for practical applications [10].

However, it also introduces technical challenges, primarily the need to compensate for phase noise and frequency drift between the independent lasers of Alice and Bob. These factors are a significant source of excess noise and may affect the system's overall performance [10].

Critical Channel Parameters

The performance of a Continuous-Variable Quantum Key Distribution (CV-QKD) system, typically quantified by the Secure Key Rate (SKR), is fundamentally constrained by two critical channel parameters: channel transmittance (T) and excess noise (ε) [12]. The SKR denotes the amount of secure key material that can be generated per unit time, usually expressed in bits per symbol or bits per second [12].

The relationship between the transmitted and received signals in a CV-QKD channel can be approximated by a simplified linear model:

$$y = tx + n,$$

where y denotes the received signal, x is the transmitted signal, t represents the channel transmittance, and n accounts for both channel-induced noise and intrinsic system noise [5].

Channel Transmittance (T)

Channel transmittance characterizes the efficiency with which the quantum signal propagates through the transmission medium. It is influenced by the physical properties of the medium—such as the quality and length of optical fibers—or, in the case of free-space optics (FSO), by atmospheric conditions (e.g., fog, rain, and turbulence) and alignment precision [12]. Lower transmittance implies greater signal attenuation, reducing the amount of quantum information reaching Bob and consequently diminishing the SKR.

In optical fiber channels, transmittance is often modeled as:

$$T = 10^{-\alpha d/10},$$

where α is the attenuation coefficient in dB/km and d is the transmission distance in kilometers [10].

Excess Noise (ε)

Excess noise encompasses all noise contributions beyond the fundamental quantum shot noise [12]. This includes technical imperfections, environmental fluctuations, and possible eavesdropping strategies. Minimizing excess noise is critical for CV-QKD performance, as it can be exploited by an eavesdropper (Eve) to extract information from the quantum channel [5]. Therefore, accurately estimating and mitigating excess noise is essential for maintaining system security and achieving a positive SKR.

Sources of Physical Channel Imperfections

Several physical-layer imperfections contribute to excess noise and affect channel transmittance in CV-QKD systems. These impairments originate from both quantum and classical sources and must be carefully modeled and mitigated to ensure reliable and secure operation.

Optical Losses

Optical losses are intrinsic to any transmission medium. In fiber-optic systems, they are primarily caused by absorption and scattering. In free-space optical (FSO) channels, atmospheric attenuation—due to fog, rain, snow, and molecular absorption—can be significant [13].

Electronic Noise

Receiver-side electronic components, such as photodetectors and amplifiers, introduce electronic noise (V_{el}), which adds to the quantum signal and contributes to excess noise [7].

Shot Noise and Thermal Noise

Shot noise is a fundamental quantum noise arising from the discrete nature of photons and serves as a reference level for CV-QKD system sensitivity. Thermal noise, generated by thermal agitation of electrons in electronic components, can also degrade system performance [14]. Any noise above the shot noise level is typically categorized as excess noise.

Temporal and Spectral Leakage

Imperfect modulators and synchronization mechanisms can cause time-domain diffusion and spectral leakage. These imperfections manifest as unintended residual modulation and photon leakage, resulting in measurable excess noise [12].

Polarization Disturbance

In fiber-based systems, random birefringence in standard single-mode fibers (SSMF) causes unpredictable variations in the state of polarization (SOP) of the quantum signal. These fluctuations can introduce cross-polarization interference and increase noise [12].

Photon Leakage

Photon leakage occurs when photons from high-power channels—such as the local oscillator

(LO) or reference tones—leak into the low-power quantum signal path. This leakage introduces noise and potential crosstalk, particularly in shared-fiber architectures [6].

Crosstalk in Coexisting Networks

Coexistence of CV-QKD with high-power classical channels in dense wavelength-division multiplexing (DWDM) networks introduces significant challenges. Classical signals, with photon flux orders of magnitude higher than quantum signals, can induce nonlinear effects such as four-wave mixing (FWM) and stimulated Raman scattering (SRS), leading to crosstalk and fluctuations in LO power [15]. These phenomena directly impact the SKR [15].

Phase Noise

In local oscillator-based (LLO) CV-QKD systems, where the LO is generated locally at the receiver, phase and frequency offsets between Alice's and Bob's lasers introduce residual phase noise. This is a major source of excess noise and must be carefully modeled [10].

Modulation-Induced Noise

In multi-carrier schemes such as orthogonal frequency division multiplexing (OFDM), practical limitations like IQ imbalance and intermodulation distortion can degrade quantum state preparation [14]. Additionally, discretization of ideal Gaussian modulation—commonly implemented as Discretized Polar Modulation (DPM)—may introduce parameter estimation bias, leading to overestimation of excess noise and underestimation of SKR if not properly calibrated [16].

Physical Channel Modeling in CV-QKD

Accurate mathematical modeling of the physical channel is essential for the analysis, simulation, and optimization of CV-QKD systems. Channel models aim to capture how the imperfections described earlier affect the propagation of quantum signals and ultimately the secure key rate (SKR).

Lossy Bosonic Channel

The most fundamental and widely adopted model for representing optical channels in CV-QKD is the lossy bosonic channel, often referred to as a linear attenuation channel. This model assumes that the optical signal undergoes linear attenuation, while the added noise is Gaussian and originates from either vacuum fluctuations or a thermal reservoir [5]. The simplified linear relation $y = tx + n$ underpins most security and performance analyses in CV-QKD.

Channel impairments are modeled via perturbations to the annihilation operators of the quantum signal and reference tones. For example, after channel propagation, the annihilation operators of the reference tone ($\hat{\alpha}'_{ref}$) and the quantum signals ($\hat{a}'_{s1}$, $\hat{a}'_{s2}$) are expressed in terms of leakage factors (h) and temporal/frequency dispersion parameters (q_{1s}, q_{2s}), allowing detailed analysis of how transmittance and excess noise are impacted [12].

Excess Noise-Specific Models

To capture the diversity of excess noise sources, specialized models are developed for distinct physical effects:

Polarization Perturbation

Channel-induced polarization rotation degrades both transmittance and excess noise performance. Dual-polarization division multiplexing (DPDM) models allow quantitative analysis of polarization extinction ratio (PER) impacts. Photon leakage between polarization modes is modeled using modified annihilation operators affected by time and frequency diffusion [12].

DWDM-Induced Crosstalk

In networks where CV-QKD coexists with classical dense wavelength-division multiplexing (DWDM) channels, nonlinear effects such as stimulated Raman scattering (SRS) and four-wave mixing (FWM) introduce stochastic fluctuations in the local oscillator (LO) power [15,17]. Modeling these effects involves deriving the LO power evolution under fiber attenuation and classical channel interference. These fluctuations affect Bob's measurement statistics and post-processing parameter estimation, degrading SKR.

Phase Noise Modeling

Residual phase noise is a major performance-limiting factor in LLO-based CV-QKD systems. Phase noise models incorporate contributions from detector electronics, the monitored intensity of the phase reference, and the measurement noise from phase tracking [10]. Kalman filters, particularly vector Kalman filters, are commonly used to estimate and compensate for both slow and fast phase drifts and laser frequency offsets [18]. These techniques improve signal recovery under time-varying channel conditions [19].

Modulation Noise: Discretization and Multi-Carrier Effects

Discretized Gaussian Modulation (DPM): Practical implementations often discretize Gaussian modulation, introducing modulation-induced fluctuations in the quadratures. These preparation noises are misattributed to channel parameters, leading to overestimation of excess noise and underestimation of SKR if not properly calibrated. The bias depends on the resolution of modulation levels [16].

Multi-Carrier OFDM Systems: Imperfections such as in-phase/quadrature (IQ) imbalance and intermodulation distortion degrade the fidelity of multi-carrier quantum state preparation. Systematic models have been proposed to assess the impact of these modulation-induced impairments [14].

Model Limitations and Applicability Conditions

The accuracy and applicability of these models are bounded by several practical considerations:

Finite-Size Effects

Security proofs often assume an asymptotic regime with an infinite number of exchanged signals. However, practical implementations involve a finite number of signals, which imposes stricter requirements on block size and excess noise control [10]. Composable security analysis is essential in such scenarios [8].

Time-Variant Channels

Environmental disturbances in LLO-based CV-QKD systems can induce time-varying channel behavior, particularly over long acquisition blocks. Accurate estimation and compensation of time-varying parameters are necessary to maintain system performance [19].

Calibration Accuracy

Discretization-induced noise (e.g., from DPM) and other imperfections require precise calibration procedures. Overestimating the homodyne detection efficiency may lead to an overestimated SKR and reduce the system's secure transmission distance [20].

Conclusion

The security and practical performance of CV-QKD systems are deeply influenced by the characteristics of the physical communication channel. This paper presented a comprehensive overview of the critical parameters and

imperfections that affect channel transmittance and excess noise, both of which directly impact the achievable SKR.

We examined the standard lossy bosonic channel model and extended the discussion to include more specific modeling approaches tailored to polarization effects, nonlinear crosstalk in DWDM networks, residual phase noise, and modulation-induced distortions. These models help to quantify how physical-layer impairments influence system security and performance under practical conditions.

Furthermore, we discussed the limitations and applicability of these models in the context of finite-size effects, time-varying channels, and calibration inaccuracies. These factors are critical when designing CV-QKD systems intended for real-world deployment, where idealized assumptions do not hold.

Looking forward, accurate and adaptive modeling of quantum channels remains an essential component in the advancement of CV-QKD technologies. Future research should focus on the integration of machine learning techniques for real-time channel estimation, robust calibration under non-stationary conditions, and composable security proofs tailored to time-dependent and discretized systems.

Ultimately, a solid understanding of physical channel behavior—supported by reliable mathematical models—is a key enabler for the secure, scalable, and efficient deployment of quantum communication systems.

Acknowledgement

This work was fully funded by the project HW DSP: Development and Prototyping of Multicore SoC with Dedicated Accelerators and RISC-V DSP, supported by QuIIN – Quantum Industrial Innovation, the EMBRAPII CIMATEC Competence Center in Quantum Technologies, with financial resources from the PPI IoT/Industry 4.0 of the MCTI, grant number 053/2023, signed with EMBRAPII.

References

1. Vu MQ, Le HD, Pham TV, Pham AT. Design of satellite-based fso/qkd systems using geo/leos for multiple wireless users. IEEE Photonics J. 2023;15(4):1–14.
2. Srisiri G, Lokesh N, Sravan T, Valiveti HB, Swaraja K, Suseela MSU. Deep learning-based channel estimation for continuous variable quantum cryptography in free-space optical (fso) communication. In: 2025 6th International Conference on Inventive Research in Computing Applications (ICIRCA). p. 203–207. IEEE; 2025.
3. Alshaer N, Ismail T. Performance evaluation and security analysis of uav-based fso/cv-qkd system employing dp-qpsk/cd. IEEE Photonics J. 2022;14(3):1–11.
4. Liu J, Cao Y, et al. Impact of homodyne receiver bandwidth and signal modulation patterns on the continuous-variable quantum key distribution. Opt Express. 2022;30(15):27912–27925.
5. Dong J, Wang T, et al. Effective excess noise suppression in continuous-variable quantum key distribution through carrier frequency switching. Entropy. 2023;25(9):1286.
6. Zhang S, Pan Y, et al. An orthogonal dual-polarization and time multiplexing scheme of continuous-variable quantum key distribution. In: 2023 21st International Conference on Optical Communications and Networks (ICOCN). p. 1–3. IEEE; 2023.
7. Cheng D, Guo Y, Dai J, Wu H, Guo Y. Neural network method: withstanding noise for continuous-variable quantum key distribution with discrete modulation. J Opt Soc Am B. 2024;41(4):879–886.
8. Wang Y, Li Y, Jiang W, Guo Y. Defending against the homodyne detector-blinding attack on continuous-variable quantum key distribution using an adjustable optical attenuator. Entropy. 2025;27(6):631.
9. Li H, Song H, Liu X, Wen J, Sun S, Li S. Reliable synchronization technology for continuous variable quantum key distribution system. In: 2022 International Conference on 6G Communications and IoT Technologies (6GIoTT). p. 35–41. IEEE; 2022.
10. Shao Y, Wang H, et al. Phase noise model for continuous-variable quantum key distribution using a local local oscillator. Phys Rev A. 2021;104(3):032608.
11. Shao Y, Huang W, et al. Practical intensity attack on continuous-variable quantum key distribution with a true local oscillator. In: Quantum and Nonlinear Optics VIII; 11905. p. 63–67. SPIE; 2021.
12. Zhang S, Wang H, et al. A novel continuous-variable quantum key distribution scheme based on multi-dimensional multiplexing technology. Appl Sci. 2024;14(2):934.
13. Nguyen TV, Le HT, Pham HT, Mai V, Dang NT. Enhancing design and performance analysis of satellite

entanglement-based cv-qkd/fso systems. IEEE Access. 2023;11:112097–112107.
14. Wang H, Pan Y, et al. Performance analysis for ofdm-based multi-carrier continuous-variable quantum key distribution with an arbitrary modulation protocol. Opt Express. 2023;31(4):5577–5592.
15. Chu B, Zhang Y, et al. Crosstalk-induced impact of coexisting dwdm network on continuous-variable qkd. In: 2020 16th International Conference on the Design of Reliable Communication Networks DRCN 2020. p. 1–5. IEEE; 2020.
16. Wang T, Li M, Wang X, Hou L. Parameter estimation calibration of discretized polar modulation continuous-variable quantum key distribution. Opt Express. 2023;31(13):21014–21024.
17. Ware C, Aymeric R, Zidi C, Lourdiane M. Potential impact of cv-qkd integration on classical wdm network capacity. IEEE Photonics Technol Lett. 2022;34(18):957–960.
18. Huang B, Huang Y, Peng Z. Tracking reference phase with a kalman filter in continuous-variable quantum key distribution. Opt Express. 2020;28(19):28727–28739.
19. Xu Y, Wang T, et al. Robust continuous-variable quantum key distribution in the finite-size regime. Photonics Res. 2024;12(11):2549–2558.
20. Zou M, Mao Y, Chen T. Rigorous calibration of homodyne detection efficiency for continuous-variable quantum key distribution. Opt Express. 2022;30(13):22788–22797.

Overview on Hardware Adaptation for Continuous-Variable Quantum Key Distribution Systems: Opportunities with RISC-V Architectures

Glenda Barbosa do Nascimento[1,2,3*], Linton Thiago Costa Esteves[1], Wagner Luiz Alves de Oliveira[4], Valeria Loureiro da Silva[1,3], Nelson Alves Ferreira Neto[1]

[1]QuIIN - Quantum Industrial Innovation, EMBRAPII CIMATEC Competence Center in Quantum Technologies, SENAI CIMATEC; Salvador, Bahia; [2]Federal University of Recôncavo da Bahia, Center for Exact and Technological Sciences; Cruz das Almas, Bahia; [3]Graduate Program in Computational Modeling and Industrial Technology (PPGMCTI), SENAI CIMATEC University; [4]Graduate Program in Electrical and Computer Engineering, Federal University of Bahia; Salvador, Bahia, Brazil

Continuous-variable quantum key distribution (CV-QKD) enables secure key exchange by exploiting the quantum properties of optical field quadratures. While CV-QKD protocols offer strong potential due to their compatibility with existing optical infrastructure, their practical deployment is limited by the high computational complexity of digital signal processing (DSP) and post-processing tasks. Operations such as low-density parity-check (LDPC) decoding for information reconciliation (IR), privacy amplification (PA), carrier recovery (CR), phase recovery (PR), and statistical estimation must be performed under stringent real-time, energy, and security constraints. Conventional programmable hardware platforms comprising general-purpose central processing units (CPUs) and graphics processing units (GPUs) often lack the efficiency required for secure and efficient CV-QKD processing in embedded or resource-constrained environments. In contrast, hard-coded application-specific integrated circuit (ASIC) solutions do not provide the flexibility demanded by evolving protocols. This paper provides an overview of a hardware adaptation strategy based on the open fifth-generation Reduced Instruction Set Computing (RISC-V). By leveraging its modularity and extensibility, we explore the design of custom instruction sets and dedicated co-processors to accelerate critical CV-QKD operations. This includes architecture-level enhancements for DSP and post-processing modules, such as CR, PR, IR, PA, and parameter estimation. The proposed approach facilitates co-design between evolving QKD protocols and hardware implementations, enabling transparent, efficient, and scalable solutions. The RISC-V-based methodology addresses CV-QKD challenges through specialized instruction extensions for dedicated processing and custom co-processors for real-time operations. Furthermore, RISC-V can enhance energy efficiency via dynamic voltage scaling and low-power modes, while its open-source nature ensures cryptographic transparency and security verification. Ultimately, this work establishes a foundation for energy-efficient and quantum-secure processor architectures capable of meeting CV-QKD demands and advancing cryptographic hardware.

Keywords: Quantum Key Distribution. Hardware Acceleration. RISC-V Architecture. Post-Processing. Secure Communication.

Designing secure, efficient, and reconfigurable hardware for next-generation cryptographic systems has become a critical task [1]. In this context, open and modular architectures such as RISC-V offer a unique opportunity to rethink how computing platforms are tailored to quantum communication protocols, enabling hardware/software co-design that aligns with both flexibility and long-term trust [2].

This discussion becomes even more relevant when applied to CV-QKD systems [3]. While CV-QKD protocols offer significant advantages, such as compatibility with existing optical infrastructures and higher key generation rates, they impose substantial computational demands during the post-processing phase. Tasks such as LDPC [4], used in IR,, parameter estimation [5], and Toeplitz hash for PA require high throughput, numerical precision, and efficient memory usage, often in real-time or embedded environments [6]. Traditional programmable platforms, such as general-purpose CPUs [7], DSPs [8], and

Received on 5 June 2026; revised 8 September 2026.
Address for correspondence: Glenda Barbosa do Nascimento. Universidade PolAv. Orlando Gomes, 1845 Piatã, Salvador - BA. Salvador, Bahia, Brazil. ZIP code: 41650-810. E-mail: glenda.nascimento@fbter.org.br.

J Bioeng. Tech. Health 2026;9(10):1033-1039
© 2026 by SENAI CIMATEC University. All rights reserved.

GPUs [9], face limitations in terms of energy consumption and scalability. In contrast, hard-coded ASICs do not provide flexibility for long-term protocol adaptation. This exposes a clear gap: developing secure quantum protocols is not sufficient on its own, as the supporting hardware must also be adapted accordingly [10].

In light of this challenge, this work proposes a theoretical approach for hardware adaptation using the RISC-V architecture to support CV-QKD systems. The central research question is: how can RISC-V be tailored to meet the specific computational requirements of quantum key distribution based on continuous variables, while ensuring energy efficiency, hardware-level security, and architectural flexibility? The hypothesis is that through custom instruction extensions, dedicated functional units, and secure hardware mechanisms, it is possible to design computing platforms optimized for CV-QKD DSP and post-processing tasks such as IR, PA, CR, PR, and parameter estimation, all within an auditable and customizable framework [11]. The objective of this article is to explore a conceptual overview of how RISC-V can serve as an option for hardware platforms specialized in quantum cryptographic applications, with a focus on CV-QKD. By identifying the computational bottlenecks in the post-processing pipeline, and mapping them to architectural opportunities within the RISC-V ecosystem, this work outlines a direction for the development of open, efficient, and secure quantum hardware platforms, suitable for real-time operation and embedded deployment [1].

The structure of this paper is organized as follows: Section 2 presents the fundamental concepts of Continuous-Variable Quantum Key Distribution (CV-QKD) systems, emphasizing the post-processing algorithms and their associated computational challenges. Section 3 introduces the RISC-V philosophy, providing the necessary architectural background to understand its potential for domain-specific customization. Section 4 explores the opportunities of leveraging RISC-V architectures to address the identified performance, flexibility, and security gaps in CV-QKD implementations. Section 5 discusses the expected benefits, open challenges, and potential research directions. Finally, Section 6 concludes the paper by summarizing the contributions and reinforcing the role of hardware adaptation in advancing secure quantum communication.

Fundamentals of CV-QKD Systems

CV-QKD protocols rely on the transmission of quantum states encoded in the conjugate quadratures of the electromagnetic field. These quadratures, denoted as $\hat{X}$ and $\hat{P}$ (representing the amplitude and phase quadrature operators), correspond to orthogonal components of the optical field. Unlike discrete-variable QKD (DV-QKD), which encodes information in discrete degrees of freedom such as photon polarization or arrival time, CV-QKD leverages continuous quadrature measurements, enabling the use of standard telecommunications components like coherent detectors [11].

Transmission with Alice and Bob

A typical implementation of a CV-QKD system involves a transmitter (Alice) and a receiver (Bob), as shown in Figure 1. Alice prepares coherent states by modulating the amplitude and phase quadrature operators ($\hat{X}$ and $\hat{P}$) of a laser beam using Gaussian-distributed random numbers with electro-optic modulators. The modulated light is then sent through a quantum channel, which can be either an optical fiber or a Free-Space Optics (FSO) link [12].

Bob receives the optical signal and performs quadrature measurements using either homodyne detection, randomly selecting to measure either X *or* P quadrature per measurement interval; or heterodyne detection, simultaneously measuring both quadratures. Both methods require a local oscillator phase-synchronized with Alice's laser. The measurement results are continuous values

Figure 1. Schematic diagram of the CV-QKD system.

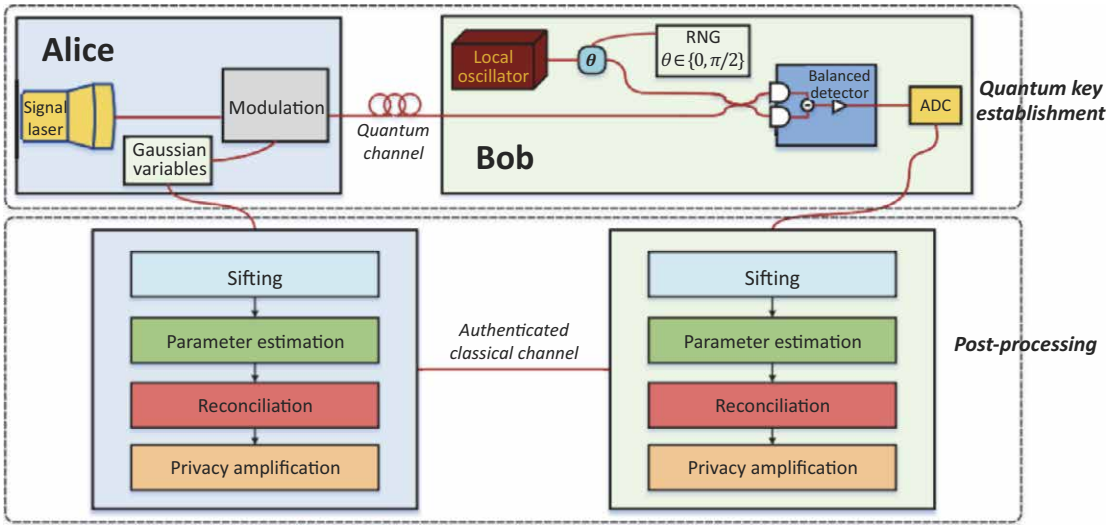

Source: Based on Wen and colleagues [13].

(not binary) that are later discretized during post-processing. This process is highly sensitive to channel loss and noise, meaning not all data is useful for key generation [3].

It is assumed that a potential eavesdropper (Eve) may intercept and resend the signal transmitted through the quantum channel. When performing quantum measurements, Eve introduces disturbances detectable as excess noise in Bob's measurements due to the quantum no-cloning theorem and uncertainty principle.

Using parameter estimation techniques, Alice and Bob analyze the transmittance (T) and excess noise (ξ) to quantify Eve's potential information and ensure key security [14].

Information Reconciliation

IR is a critical stage in CV-QKD systems, where the continuous-variable measurements from Alice and Bob are discretized into binary sequences using quantization techniques such as *slicing*. This process divides the continuous signal range into defined regions (bins), each assigned a bit value. However, due to channel noise and measurement imperfections, Alice's and Bob's sequences exhibit discrepancies [13].

Through classical communication techniques, both parties perform reconciliation using error-correcting codes, most notably LDPC codes. While LDPC coding achieves near-capacity correction with minimal information leakage to eavesdroppers, it introduces significant computational burdens. High-performance LDPC decoding requires large block sizes (> 10^6 bits), parallel processing, and precision arithmetic (floating-point or fixed-point), particularly under low signal-to-noise ratio (SNR) conditions. Implementing such algorithms efficiently on general-purpose CPUs is often impractical for real-time operation. Accelerators like GPUs can address throughput demands but face limitations in energy efficiency and flexibility for embedded or edge deployments [15].

Privacy Amplification

PA is the final post-processing step in CV-QKD systems. Its role is to reduce any residual information potentially acquired by an eavesdropper during transmission and reconciliation to a negligible level. This is achieved using cryptographic hash functions from the universal class, such as Toeplitz matrices, which compress a long, partially secure key to a shorter, information-theoretically secure key.

From a hardware perspective, PA presents significant computational challenges. Operations involve large matrix multiplications (e.g., Toeplitz-vector products) that can be optimized through fast Fourier transforms (FFT), requiring both high throughput (>10 Gbps) and bit-accurate precision [16].

The RISC-V Philosophy

RISC-V is an open standard instruction set architecture (ISA) based on Reduced Instruction Set Computing (RISC) principles. It prioritizes hardware efficiency through a minimal base instruction set of simple, frequently used operations [1]. This deliberate minimalism enables inherently simple, compact, and fast hardware for instruction decoding and pipeline implementation [2].

The architecture minimizes complexity by maintaining a small core instruction set, reducing silicon area, power consumption, and design verification overhead. While complex instructions in other ISAs may be used infrequently, they introduce pervasive control logic overhead that impacts even basic operations [2].

RISC-V's extensible modular design embodies this philosophy, organizing functionality into optional standard extensions. Far from limiting capability, this simplicity enables complex operations through optimized instruction sequences while avoiding unnecessary hardware complexity penalties. This combination of efficiency and customizability makes RISC-V particularly suitable for domain-specific systems like CV-QKD processors.

Opportunities with RISC-V Architectures

The evolution of CV-QKD systems demands adaptable and efficient hardware solutions capable of handling challenging post-processing tasks and stringent security requirements. In this context, RISC-V architectures stand out as a strategic opportunity, offering an open and flexible platform. Its core features align well with the implementation challenges of such systems [17].

Customization for QKD Post-Processing

One of RISC-V's most significant advantages lies in its modular and open-source architecture, which enables a high degree of customization. In the context of CV-QKD, this flexibility allows the development of processor cores specifically optimized for control and coordination tasks during the post-processing phase, without incurring the overhead typically associated with proprietary architectures. As shown in Figure 2, such processor cores can be designed with a lightweight and efficient microarchitectural structure, tailored precisely to the application's performance and resource constraints.

RISC-V also supports the integration of custom instruction set extensions (ISA extensions), such as those for 32-bit integer operations (RV32I) and partial support for multiplication and division (RV32M) [2]. This enables the RISC-V core to efficiently execute the arithmetic and logical operations required for post-processing, while maintaining a lightweight hardware structure. Furthermore, native support for interrupt handling mechanisms is another strong point, ensuring fast responses to external events or system requests [13].

Heterogeneous Architectures

The true potential of the RISC-V architecture for CV-QKD lies in its ability to act as the central controller in heterogeneous architectures, where the most demanding computational tasks are offloaded to dedicated hardware accelerators [18]. This approach frees the RISC-V core to focus on control and decision-making operations, while specialized modules handle intensive processing. Examples of how this is applied include:

1. **Optimized Information Reconciliation:** Dedicated modules can be designed to process

Figure 2: RISC-V CPU Interface [1].

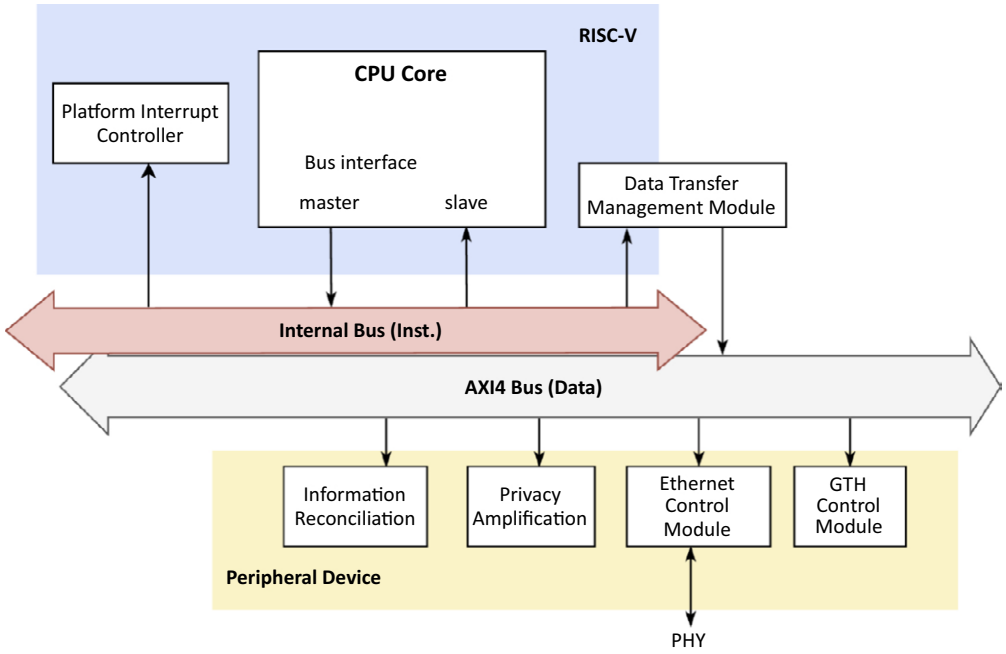

Source: Based on Wu and colleagues [1].

the LDPC parity-check matrix, using compact representations that drastically reduce storage requirements (as demonstrated by Xuan Wen and colleagues [13], where reconciliation protocols achieve near-optimal efficiencies, this approach can reduce storage by up to 99% for long codes). Modularity enables the implementation of LDPC decoders with parallel submodules and fixed-point arithmetic, optimizing throughput and resource usage, thus overcoming the typical complexity bottleneck of this stage.

2. **Accelerated Privacy Amplification:** Multiply-Accumulate (MAC) units specialized in Galois Fields GF(2) can be developed to speed up privacy amplification operations, efficiently transforming the reconciled key into a highly secure final key [16].
3. **Data Transfer Management (DTM):** The RISC-V architecture greatly benefits from integration with data transfer management modules based on protocols such as AXI. These modules can act as independent bus masters, managing large volumes of data between peripherals without constant CPU intervention. This frees the RISC-V core for critical control tasks, improving responsiveness and overall system efficiency [1].

High-Performance Bus and Modularity

The adaptability of RISC-V facilitates the implementation of split-bus architectures, separating instruction and data traffic. This is crucial for CV-QKD systems, as it allows:

1. **Bandwidth Optimization:** Different bandwidth requirements for instructions and data can be handled independently, avoiding bottlenecks and contention.
2. **High-Speed Data Transmission:** As presented and discussed by Wu and colleagues. [1], the use of high-performance data buses, such as AXI4-full (running at 200 MHz with 128-bit width), enables efficient bulk data transfer, essential for the throughput required in QKD post-processing. This capability supports task-level pipelining for computational modules, ensuring continuous and uninterrupted data flow.

Adhering to a modular design philosophy is fundamental to the RISC-V paradigm. This means peripherals can be designed to be seamlessly integrated, with memory-mapped data buffers at module interfaces. Such standardization not only simplifies the integration of new modules but also ensures system compatibility and upgradeability regardless of future internal algorithmic optimizations. High-speed communication interfaces, such as Gigabit Ethernet and GTH (Giga-Transceiver High-speed), can be easily integrated, ensuring the necessary connectivity for raw key flow and post-processing data [19].

Conclusion

CV-QKD systems present significant computational challenges in post-processing, particularly during information reconciliation and privacy amplification. These operations demand high computational performance, numerical precision, and energy efficiency, which limits the adoption of generic architectures or commercial platforms in real-time and embedded quantum communication applications.

RISC-V's open and extensible ISA enables hardware specialization through custom instructions and dedicated co-processors for CV-QKD-specific tasks, such as FFT-accelerated matrix operations for PA, parallel LDPC decoding for IR, and cryptographic hashing. This customization capability facilitates domain-optimized processors that simultaneously achieve adaptability, scalability, and energy efficiency for quantum-secure networks.

As next steps, we propose FPGA-based prototyping of RISC-V cores with CV-QKD instruction extensions, focusing on quantitative evaluation of throughput (Gbps), power efficiency (μW/bit), and protocol adaptability across diverse quantum channel conditions.

Acknowledgement

This work has been partially funded by the project "HW DSP: Desenvolvimento e Prototipagem de SoC Multicore com Aceleradores Dedicados e DSP RISC-V" supported by QuIIN - Quantum Industrial Innovation, EMBRAPII CIMATEC Competence Center in Quantum Technologies, with financial resources from the PPI IoT/Manufatura 4.0 of the MCTI grant number 053/2023, signed with EMBRAPII. The authors would also like to acknowledge the financial support provided by MCTI/SENAI CIMATEC, CNPq and CAPES.

References

1. Wu X, Liao L, Fan X, Chen Y, Huang J, Liu M, Tian Z, Mu T, Guo J, Liu B, et al. A flexible SoC for quantum key distribution post-processing based on RISC-V processor. Quantum Sci Technol. 2025;10(3):035027.
2. Harris D, Harris S. Digital design and computer architecture. Morgan Kaufmann; 2013.
3. da Silva VL, Dias MA, Ferreira Neto NA, Tacla AB. From coherent communications to quantum security: modern techniques in CV-QKD. In: 2024 SBFoton International Optics and Photonics Conference (SBFoton IOPC); 2024. IEEE. p. 1–5.
4. Ferreira Neto NA, de Oliveira JRS, de Oliveira WLA, Bittencourt JCN. VLSI architecture design and implementation of a LDPC encoder for the IEEE 802.22 WRAN standard. In: 2015 25th International Workshop on Power and Timing Modeling, Optimization and Simulation (PATMOS); 2015. p. 71–76.
5. Galvão LQ, de Sousa DJG, Dias MA, Ferreira Neto NA. Neural network for excess noise estimation in continuous-variable quantum key distribution under composable finite-size security. 2025.
6. Gallager R. Low-density parity-check codes. IRE Trans Inf Theory. 1962;8(1):21–28.
7. Höller R, Haselberger D, Ballek D, Rössler P, Krapfenbauer M, Linauer M. Open-source RISC-V processor IP cores for FPGAs—overview and evaluation. In: 2019 8th Mediterranean Conference on Embedded Computing (MECO); 2019. p. 1–6.
8. Gholizadehazari E, Ayhan T, Ors B. An FPGA implementation of a RISC-V based SoC system for image processing applications. In: 2021 29th Signal Processing and Communications Applications Conference (SIU); 2021. p. 1–4.
9. Han R, Tine B, Lee J, Sim J, Kim H. Supporting CUDA for an extended RISC-V GPU architecture. arXiv preprint arXiv:2109.00673. 2021.
10. Baseri Y, Chouhan V, Hafid A. Navigating quantum security risks in networked environments: a

comprehensive study of quantum-safe network protocols. Comput Secur. 2024;142:103883.
11. Zhang Y, Bian Y, Li Z, Yu S, Guo H. Continuous-variable quantum key distribution system: past, present, and future. Appl Phys Rev. 2024;11(1).
12. Brunner HH, Fung CHF, Peev M, Méndez RB, Ortiz L, Brito JP, Martín V, Rivas-Moscoso JM, Jiménez F, Pastor AA, et al. Demonstration of a switched CV-QKD network. EPJ Quantum Technol. 2023;10(1):38.
13. Wen X, Li Q, Mao H, Wen X, Chen N. An improved slice reconciliation protocol for continuous-variable quantum key distribution. Entropy. 2021;23(10):1317.
14. How Alice Outwits Eve. A talk on quantum cryptography. In: Coding theory and cryptography: from Enigma and Geheimschreiber to quantum theory. Springer Science & Business Media; 2012. p. 144.
15. Daneshgaran F, Mondin M, Olia K. Permutation modulation for quantization and information reconciliation in CV-QKD systems. In: Quantum Communications and Quantum Imaging XV. Vol. 10409. SPIE; 2017. p. 61–70.
16. Wang X, Zhang Y, Yu S, Guo H. High-speed implementation of length-compatible privacy amplification in continuous-variable quantum key distribution. IEEE Photonics J. 2018;10(3):1–9.
17. Cui E, Li T, Wei Q. RISC-V instruction set architecture extensions: a survey. IEEE Access. 2023;11:24696–24711.
18. Silvano C, Ielmini D, Ferrandi F, Fiorin L, Curzel S, Benini L, Conti F, Garofalo A, Zambelli C, Calore E, et al. A survey on deep learning hardware accelerators for heterogeneous HPC platforms. ACM Comput Surv. 2025;57(11):1–39.
19. Greengard S. Will RISC-V revolutionize computing? Commun ACM. 2020;63(5):30–32.

Simulating the BB84 QKD Protocol: A QuTiP-Based Study in Ideal Quantum Channels

Henrique Sobrinho Ghizoni[1*], Anderson R. C. Buarque[1]
[1]QuIIN - Quantum Industrial Innovation, EMBRAPII CIMATEC Competence Center in Quantum Technologies, SENAI CIMATEC; Salvador, Bahia, Brazil

This work presents a simulation of the BB84 Quantum Key Distribution (QKD) protocol using QuTiP, an open-source Python framework for quantum system modeling. The protocol is implemented in an ideal noise-free quantum channel, enabling a clear analysis of its fundamental stages, including state preparation, basis selection, key sifting, error estimation, and privacy amplification. The simulation reproduces the expected behavior of BB84 and allows the investigation of eavesdropping effects through the Quantum Bit Error Rate (QBER) and mutual information between communicating parties. Results show that increasing the eavesdropping interception rate reduces the mutual information shared between Alice and Bob while increasing the information available to Eve. The analysis indicates that both quantities become comparable at approximately EIR ≈ 0.59, providing a quantitative criterion for assessing the impact of eavesdropping on BB84 security. In addition, computational performance measurements demonstrate that the proposed implementation can be executed efficiently on conventional personal computers, reinforcing its suitability for educational and research applications. The results highlight the potential of QuTiP-based simulations as an accessible and reproducible framework for studying the security principles underlying quantum key distribution.

Keywords: Quantum Key Distribution (QKD). BB84 Protocol. Quantum Cryptography. QuTiP. Quantum Education.

Abbreviations: QKD, Quantum Key Distribution. P&M, Prepare and Measure. HWP, Half-Wave Plate. PBS, Polarized Beam Splitter. RNG, Random Number Generation. SP, Single Photon. PP, Post-Processing. RKL, Raw Key Length. kB, Kilobytes. B, Bytes. ms, milliseconds. s, seconds.

Classical cryptography relies on the computational difficulty of efficiently solving problems such as integer factorization or discrete logarithms and underpins widely used protocols such as RSA and Diffie–Hellman. The advancement of quantum computing and the existence of algorithms such as Shor's threaten this traditional framework, making it urgent to seek solutions based on physical principles [2].

In this context, quantum cryptography emerges as a secure alternative. The BB84 protocol, conceived by Bennett and Brassard in 1984 [1], introduces a paradigm that exploits non-orthogonal quantum states distributed in conjugate bases to share secret keys. The protocol relies on two fundamental principles of quantum mechanics: the no-cloning theorem, which prevents copying unknown quantum states, and the unavoidable disturbance caused by any measurement, which introduces detectable errors. This approach grants BB84 physical security and enables the detection of intrusions that cannot be concealed, an advantage that classical cryptography does not offer.

This work presents simulations performed with QuTiP, a Python library dedicated to modeling quantum systems, which enables the step-by-step implementation of the BB84 protocol. The implementation was carried out over an ideal, noise-free quantum channel, in order to clearly observe each stage of the protocol, from preparation and measurement to post-processing. This controlled setting not only facilitates a detailed analysis of BB84's operation but also makes it a valuable tool for educational purposes, supporting the teaching and understanding of fundamental concepts in quantum cryptography. Finally, the work investigates how eavesdropping on the quantum channel can be detected through the estimation of the QBER parameter and/or the

Received on 7 June 2026; revised 24 September 2026.
Address for correspondence: Henrique Sobrinho Ghizoni. Av. Orlando Gomes, 1845 Piatã, Salvador - BA. Salvador, Bahia, Brazil. ZIP code: 41650-810. E-mail: hsghizoni@gmail.com.

J Bioeng. Tech. Health 2026;9(10):1040-1046
© 2026 by SENAI CIMATEC University. All rights reserved.

analysis of the mutual information between the parties involved in the protocol.

Quantum Key Distribution-BB84

The BB84 protocol, proposed by Charles Bennett and Gilles Brassard in 1984 [1], is the first and most well-known QKD protocol. It enables two parties, traditionally named Alice (sender) and Bob (receiver), to establish a shared secret key with security guaranteed by the laws of quantum mechanics. The protocol leverages fundamental quantum principles such as the no-cloning theorem and the fact that quantum measurements disturb the system, thereby making any eavesdropping attempt detectable [2,7].

To implement these principles in practice, BB84 relies on two types of communication channels: a quantum channel, inherently vulnerable to eavesdropping, used for transmitting quantum states, and a classical public channel that, despite being unsecured, requires authentication to prevent attacks.

While the quantum channel ensures the uniqueness and non-replicability of the transmitted qubits, the classical channel is used for basis reconciliation and error correction. By monitoring the quantum bit error rate, the protocol allows the detection of potential eavesdropping attempts, thereby ensuring the integrity and confidentiality of the final secret key.

BB84: Protocol Essential Parts

The protocol operationalizes three essential needs: a quantum channel for transmitting qubits encoded in photon polarization states; an authenticated classical channel for public communication; and trust in the validity of quantum mechanical postulates, especially the no-cloning theorem, superposition, and measurement-induced collapse.

In practical implementations, BB84 uses the polarization states of single photons to encode information [2]. The protocol employs two conjugate bases. The rectilinear basis, $\boldsymbol{B_z}$, consists of the horizontal (0°), $|\boldsymbol{H}\rangle$, and vertical (90°), $|\boldsymbol{V}\rangle$, polarization states,

$$\boldsymbol{B_z} = \{|\boldsymbol{H}\rangle, |\boldsymbol{V}\rangle\}, \quad (1)$$

while the diagonal basis, $\boldsymbol{B_x}$, consists of the diagonal (45°), $|\boldsymbol{D}\rangle$, and the anti-diagonal (-45°) polarization states,

$$\boldsymbol{B_x} = \{|\boldsymbol{D}\rangle, |\boldsymbol{A}\rangle\} \quad (2)$$

where

$$|\boldsymbol{D}\rangle = \frac{|\boldsymbol{H}\rangle+|\boldsymbol{V}\rangle}{\sqrt{2}}, \quad (3)$$

$$|\boldsymbol{A}\rangle = \frac{|\boldsymbol{H}\rangle-|\boldsymbol{V}\rangle}{\sqrt{2}} \quad (4)$$

Shannon entropy [6] quantifies the uncertainty associated with a random variable and is given by

$$\boldsymbol{H(X)} = -\sum_i \boldsymbol{p(x_i) log_2[p(x_i)]}, \quad (5)$$

where $\boldsymbol{p(x_i)}$ represents the probability of occurrence of event $\boldsymbol{x_i}$. In the context of quantum key distribution, entropy measures the unpredictability of the generated keys and serves as a key parameter for assessing security and the rate of useful information transmitted.

Closely related to this concept is mutual information, defined between two random variables $\boldsymbol{X}$ and $\boldsymbol{Y}$ as

$$\boldsymbol{I(X:Y) = H(X) + H(Y) - H(X,Y)}, \quad (6)$$

where $\boldsymbol{H(X,Y)}$ is the joint entropy between the X and Y variables [6]. The mutual information, $\boldsymbol{I(X:Y)}$, quantifies how much information is shared between the random variables X and Y. In the context of quantum key distribution, mutual information is used to quantify the information shared between the legitimate users (Alice and Bob) and compare it with the information potentially accessible to an eavesdropper (Eve).

Prepare and Measure

The P&M operation of the BB84 protocol can be divided into a few main steps:

P&M-I. Alice generates two uniformly random bit strings:

$$a = (a_1, \ldots, a_{4n}), \quad (7)$$

$$b = (b_1, \ldots, b_{4n}), \quad (8)$$

where $a_i \in \{0,1\}$ denotes the bit value and $b_i \in \{0,1\}$ determines the basis ($0: B_z, 1: B_x$). The use of an oversized block (e.g., 4n) anticipates the need for sifting and error estimation.

For each pair (a_i, b_i) Alice prepares a qubit:

$$|\psi_i\rangle = \begin{cases} |\mathrm{H}\rangle, & a_i = 0,\ b_i = 0; \\ |\mathrm{V}\rangle, & a_i = 1,\ b_i = 0; \\ |A\rangle, & a_i = 0,\ b_i = 1; \\ |D\rangle, & a_i = 1,\ b_i = 1. \end{cases} \quad (9)$$

She then sends the sequence of 4n qubits to Bob via the quantum channel. The no-cloning theorem ensures that any attempt by Eve to duplicate these states will fail [2-3].

P&M-II. Bob independently chooses a random basis string, given by

$$b' = (b'_1, \ldots, b'_{4n}) \quad (10)$$

and measures each incoming qubit in the corresponding basis. He records the outcomes a_i. If $b_i = b'_i$, then Bob retrieves a_i with certainty (ignoring noise); otherwise, the outcome is statistically uncorrelated with a_i.

Post-Processing

The post-processing operation of the BB84 protocol can be divided into a few main steps:

PP-I. Alice divulges her basis string b_i over the authenticated classical channel. Bob compares with his b'_i and retains only those indices where $b_i = b'_i$. The remaining bits, roughly 2n in number, form the sifted key. As shown by [2], the expected matching probability is 0.5 due to the uniform random choice of bases.

PP-II. Alice and Bob publicly sample a subset of the sifted key to estimate the Quantum Bit Error Rate (QBER):

$$QBER = {}^{N_b}/_{L_{Sk}}, \quad (11)$$

where N_b is the number of bit mismatches observed in the subset of sifted-key bits, and L_{Sk} is the size of this subset, used to estimate the QBER. An intercept-resend attack introduces a theoretical QBER of 25%, since Eve's random basis choice leads to a 50% error rate half the time [2-3].

PP-III. Provided the QBER is below a critical threshold (typically $\sim 11\%$ for individual attacks) [5], Alice and Bob engage in an error correction protocol (e.g., Cascade or LDPC codes) to reconcile discrepancies in their sifted keys.

PP-IV. To remove any partial knowledge Eve may have acquired, Alice and Bob apply a privacy amplification procedure, compressing the reconciled key into a shorter string of length L_{Rk}. A simplified estimate of the secret key fraction can be expressed as:

$$r = 1 - H(QBER) - I(A:E), \quad (12)$$

where $H(p)$ is the binary entropy function and $I(A:E)$ is Eve's estimated mutual information. This ensures a secure final key under general attacks.

Eve's Attack

There are different types of attacks [2,7] that Eve can perform against the BB84 protocol, including Intercept-Resend (IR), Photon Number Splitting (PNS), and Blinding Attacks. In the intercept-resend attack, Eve intercepts the quantum states transmitted through the quantum channel between Alice and Bob, randomly chooses a basis to measure each qubit, b''_i, and then prepares and retransmits a new quantum state to Bob according to the measurement outcome. Because Eve does not know the basis originally selected by Alice, her measurements inevitably introduce detectable errors into the key generation process, which can be quantified during the parameter estimation stage through metrics such as the Quantum Bit Error Rate (QBER). The objective of this attack is to acquire as much information as possible about the secret key while remaining undetected. As one of the most fundamental and pedagogically relevant attacks in quantum key distribution, the Intercept-Resend strategy is adopted in this work as the primary model for eavesdropping analysis.

There are more sophisticated attacks, such as the Photon Number Splitting (PNS) attack [2,7], in which Eve exploits multi-photon pulses emitted by a non-ideal photon source. By selectively splitting and storing one of the photons in a quantum memory while allowing the remaining photons to continue

to Bob, Eve can postpone her measurement until basis information becomes available during the classical communication stage. Another well-known attack is the Blinding Attack [2,7], which exploits vulnerabilities in avalanche photodiode (APD) detectors. In this attack, Eve manipulates Bob's detector behavior using bright light pulses, allowing her to influence detection events and potentially gain information without introducing a significant increase in the QBER.

Implementation

The BB84 protocol was designed to be implemented in photonic systems, ideally operating in the Single-Photon (SP) regime. Figure 1 illustrates a possible implementation of the protocol, where the quantum channel may be established through free-space links or optical fibers. The Classical Authenticated Channel (CAC) may be public and fully observable by Eve, provided that authentication mechanisms prevent message forgery and message tampering.

In the context of BB84, the presence of an eavesdropper, conventionally called Eve, must always be considered. In this work, we focus on the Intercept-Resend attack, in which Eve can access all information disclosed through the classical channel, without being able to modify it. Additionally, Eve intercepts the quantum channel, measures the quantum state transmitted by Alice, $|\psi_A\rangle$, and then prepares and retransmits to Bob a new quantum state, $|\psi_E\rangle$, consistent with the measurement outcome. It is worth noting that, due to the no-cloning theorem [2], Eve cannot create a perfect copy of Alice's quantum state.

Figure 1. (Color online) Schematic representation of one possible implementation of the BB84 protocol. Alice randomly selects a basis and a bit value to prepare a quantum state by encoding the polarization of a laser-generated photon using a Half-Wave Plate (HWP). The encoded state is then transmitted to Bob through the quantum channel. Bob independently and randomly selects a measurement basis and configures his receiver accordingly. A Polarizing Beam Splitter (PBS) maps the photon's polarization onto distinct propagation paths, which are associated with detectors D_0 and D_1, corresponding to the binary outcomes 0 and 1. In the Intercept-Resend attack model considered in this work, Eve employs the same measurement apparatus as Bob and the same state-preparation apparatus as Alice, allowing her to intercept, measure, prepare, and retransmit quantum states through the channel.

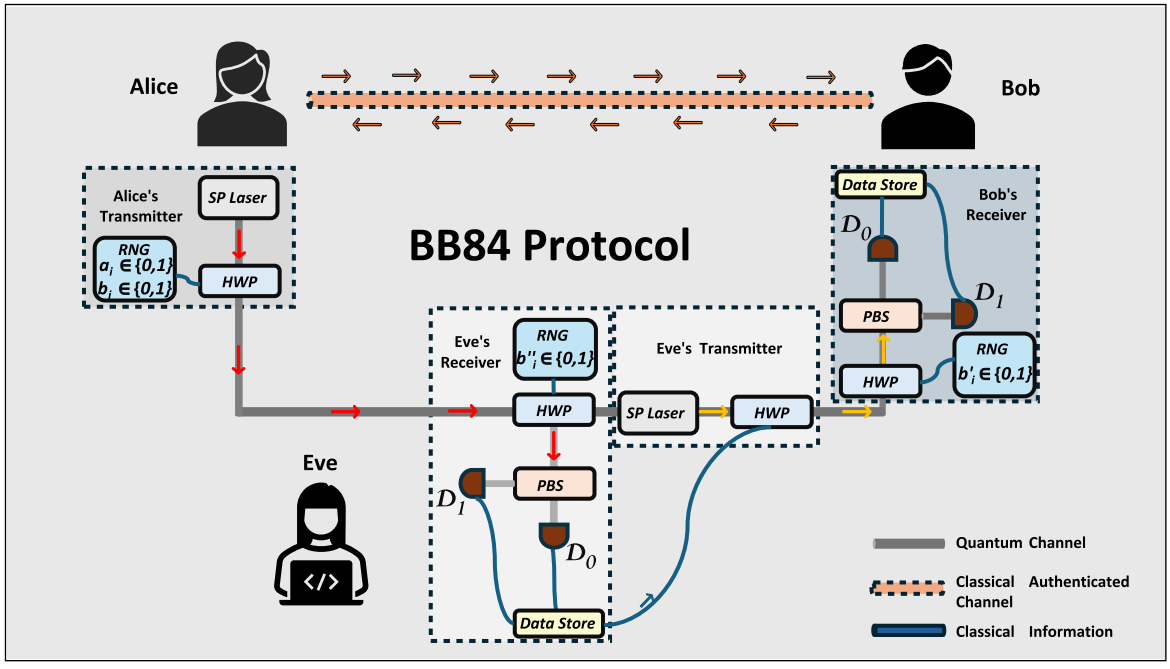

As shown in Figure 1, Alice prepares the state using three main components: a random number generator (RNG), used to generate the bit to be sent a_i, and the basis chosen to encrypt the bit, b_i; a single-photon laser; and a Half-Wave Plate (HWP), responsible for generating polarization in the photon, which can be 0°, 90°, -45°, or 45°. Alice prepares the state $|\psi_A\rangle$ using these tools and sends it to Bob through the quantum channel.

Bob's and Eve's measurements rely on essentially the same optical components: a Random Number Generator (RNG) to select the measurement basis, a Polarizing Beam Splitter (PBS) to map the photon's polarization onto distinct propagation paths, two detectors, D_0 and D_1, associated with the binary outcomes 0 and 1, and a memory unit to store the measurement results. While Bob performs measurements as part of the legitimate protocol execution, Eve uses the same measurement procedure during the Intercept-Resend attack. After measuring Alice's transmitted quantum state, Eve prepares a new quantum state, $|\psi_E\rangle$, consistent with the measurement outcome and retransmits it to Bob through the quantum channel. This strategy allows Eve to gain information about the key while inevitably introducing errors that may reveal her presence.

Simulation Methodology

The primary objective of the BB84 protocol is to establish a secure key between Alice and Bob while enabling the detection of potential eavesdropping attempts. If Eve intercepts the quantum channel, her presence can be detected during the post-processing stage, particularly in the parameter estimation and privacy amplification steps, through the estimation of the Quantum Bit Error Rate (QBER) and the subsequent decision to either continue or abort the protocol. To simulate the BB84 protocol depicted in Figure 1, this work employs QuTiP [4], a Python framework for quantum system simulation and analysis.

Two complementary analyses are performed in this work. The first investigates the impact of Eve's interception on protocol reliability by considering fixed Eavesdropping Interception Rates (EIRs) of 0.5 and 1.0 over different numbers of protocol rounds. This analysis focuses on the relationship between the Quantum Bit Error Rate (QBER) and the size of the generated raw key. The second analysis evaluates how different EIR values affect the information shared among the communicating parties by examining the mutual information between Alice and Bob, $I(A:B)$, the mutual information between Alice and Eve, $I(A:E)$, and the difference between these quantities, defined as $\Delta I = I(A:B) - I(A:E)$.

Results

The Quantum Bit Error Rate (QBER) is a key metric in the BB84 protocol, as it enables the detection of potential eavesdropping attempts during protocol execution. Figure 2 contains the QBER results for 20 independent protocol executions for three Raw Key Length (RKL) values, namely 64 B, 0.25 kB, and 16 kB, and for two Eavesdropping Interception Rates (EIRs), 0.5 and 1.0, corresponding to 50% and 100% interception of the transmitted quantum states, respectively. The results reveal a clear relationship between the size of the generated raw key and the statistical stability of the QBER estimation. As the RKL increases, fluctuations in the estimated QBER decrease, leading to more stable and accurate measurements. This behavior indicates that larger key sizes improve the reliability of parameter estimation and, consequently, the effectiveness of eavesdropping detection, which is particularly relevant for practical QKD implementations.

The mutual information between Alice and Bob, $I(A:B)$, quantifies the amount of information shared between the legitimate users and therefore provides a useful metric for evaluating the effectiveness of a QKD protocol. Similarly, the mutual information between Alice and Eve, $I(A:E)$, represents the amount of information potentially accessible to the eavesdropper and can be used to assess the effectiveness of an attack.

Figure 2. (Color online) The QBER rate vs round in the BB84 protocol simulation using QuTiP. The orange, red, and light blue curves correspond to EIR = 1.0, for three key sizes, 64 B, 0.25 kB, and 16 kB, respectively. The green, dark blue and black curves correspond to EIR = 0.5, for three key sizes, 64 B, 0.25 kB, and 16 kB, respectively. The larger the key size, the smaller the variation in the QBER value.

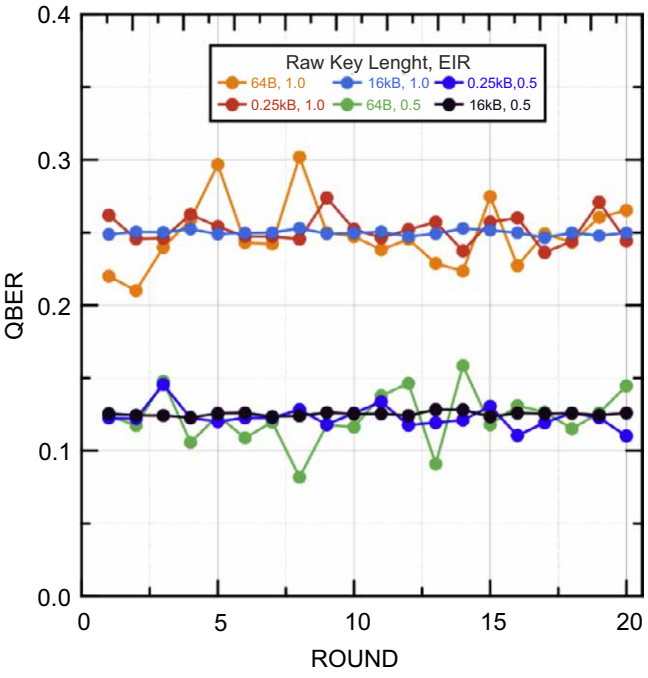

Figure 3 presents the relationship between the Eve Interception Rate (EIR) and the mutual-information quantities $\boldsymbol{I(A:B)}$, $\boldsymbol{I(A:E)}$ and $\boldsymbol{\Delta I}$, considering a Raw Key Length (RKL) of 64 kB. The results reveal a strong dependence of these quantities on the interception rate. As EIR increases, $\boldsymbol{I(A:B)}$ and $\boldsymbol{\Delta I}$ decrease, while $\boldsymbol{I(A:E)}$ increases approximately linearly. This behavior reflects the gradual transfer of information advantage from the legitimate users to the eavesdropper as the interception rate grows. A particularly important result is observed at approximately $\boldsymbol{EIR \approx 0.59}$, where $\boldsymbol{(A:B) \approx I(A:E)}$. At this point, Eve acquires an amount of information comparable to that shared between Alice and Bob, indicating a significant reduction in protocol security. This observation reinforces the importance of parameter estimation and QBER monitoring as mechanisms for detecting eavesdropping and deciding whether the protocol should proceed or be aborted.

As shown in Figure 2, for $\boldsymbol{EIR = 1.0}$, the average QBER value is approximately $\boldsymbol{25\%}$, which corresponds to the theoretical value expected for an Intercept-Resend attack in an ideal quantum channel. For $\boldsymbol{EIR = 0.5}$, the average QBER is approximately $\boldsymbol{12.5\%}$, representing a warning region that is already close to the point where Eve's information becomes comparable to Bob's information about Alice's key.

In terms of performance, for the data obtained in Figure 2, the average execution times obtained for $\boldsymbol{EIR = 1.0}$ were $\boldsymbol{137.6\,ms}$, $\boldsymbol{423.3\,ms}$, and $\boldsymbol{24.67s}$ for RKL of 64 B, 0.25 kB, and 16 kB, respectively. For $\boldsymbol{EIR = 0.5}$, the average values obtained were $\boldsymbol{110.43\,ms}$, $\boldsymbol{349.4\,ms}$ and $\boldsymbol{19.7\,s}$, respectively, such that simulations with $\boldsymbol{EIR = 0.5}$ take on average approximately $\boldsymbol{81\%}$ of the execution time for cases with $\boldsymbol{EIR = 1.0}$ (values obtained with a notebook with an i7-9750H processor). These execution times demonstrate that the proposed framework can be efficiently executed on conventional personal computers, reinforcing its suitability for educational activities and introductory studies in quantum cryptography.

Conclusions

This work presented a QuTiP-based implementation of the BB84 protocol, enabling the investigation of key security metrics such as the Quantum Bit Error Rate (QBER) and mutual information under different eavesdropping scenarios. The results are consistent with the theoretical behavior of the BB84 protocol and demonstrate the effectiveness of QBER-based parameter estimation for detecting eavesdropping attempts. Furthermore, the mutual-information analysis revealed a progressive reduction in the information advantage shared between Alice and Bob as the Eve Interception Rate (EIR) increased. In particular, the point at which $\boldsymbol{I(A:B)}$ becomes comparable to $\boldsymbol{I(A:E)}$, observed at approximately

Figure 3. (Color online) Mutual information as a function of the Eve Interception Rate (EIR). As the interception rate increases, the mutual information shared between Alice and Bob, $I(A:B)$, decreases, while the mutual information available to Eve, $I(A:E)$, increases. The information advantage, ΔI, decreases accordingly and approaches zero at approximately $EIR \approx 0.59$, indicating the point at which Eve obtains an amount of information comparable to that shared between the legitimate users [2].

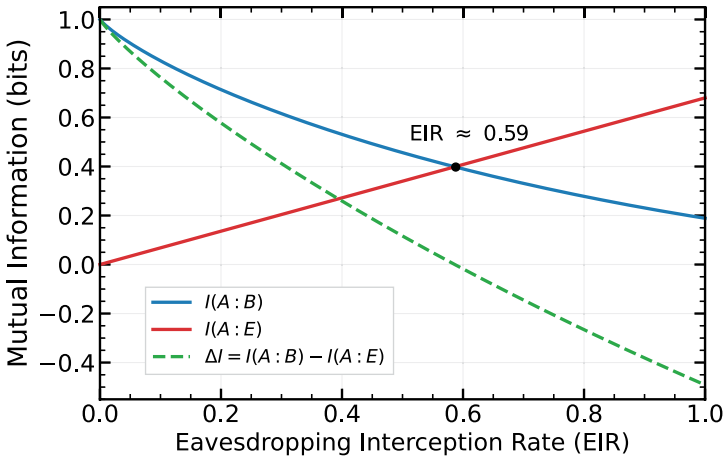

$EIR \approx 0.59$, highlights the security implications of the Intercept-Resend attack and reinforces the importance of protocol-abort criteria based on security monitoring. From a computational perspective, the measured execution times demonstrate that the proposed implementation can be efficiently executed on conventional personal computers, making it suitable for educational activities, classroom demonstrations, and introductory studies in quantum cryptography. The results obtained reinforce the value of simulation-based approaches for understanding and teaching quantum communication protocols while providing practical insights into the operation and security of BB84. Future work may extend the proposed framework by incorporating realistic quantum-channel impairments, detector non-idealities, and more advanced attack strategies, such as Photon Number Splitting (PNS) and detector-blinding attacks, enabling closer comparisons between simulated and experimental QKD implementations.

Acknowledgement

This work has been fully funded by the project "Circuito formativo em Tecnologias Quânticas-QIN-FCRH-2025-2-1-1" and was supported by QuIIN - Quantum Industrial Innovation, EMBRAPII CIMATEC Competence Center in Quantum Technologies, with financial resources from the PPI IoT/Manufatura 4.0 of the MCTI grant number 053/2023, signed with EMBRAPII.

References

1. Bennett CH, Brassard G. Quantum cryptography: public key distribution and coin tossing. Theor Comput Sci. 2014;560(7).
2. Wolf R. Quantum key distribution protocols. In: Wolf R. Quantum key distribution: an introduction with exercises. Cham: Springer Nature Switzerland; 2021. p. 93-98.
3. Nielsen MA, Chuang IL. Quantum computation and quantum information. Cambridge: Cambridge University Press; 2010. p. 587-589.
4. Johansson JR, Nation PD, Nori F. QuTiP: an open-source Python framework for the dynamics of open quantum systems. Comput Phys Commun. 2012;183(8):1760-1772. doi:10.1016/j.cpc.2012.02.021
5. Shor PW, Preskill J. Simple proof of security of the BB84 quantum key distribution protocol. Phys Rev Lett. 2000;85(2):441-444.
6. Cover TM, Thomas JA. Elements of information theory. 2nd ed. Hoboken: Wiley; 2006.
7. Scarani V, Bechmann-Pasquinucci H, Cerf NJ, Dušek M, Lütkenhaus N, Peev M. The security of practical quantum key distribution. Rev Mod Phys. 2009;81(3):1301-1350.

Biomethane Insertion in the Piped Natural Gas Network in the State of Bahia – Brazil

Paulo Roberto dos Santos[1]*, Hugo Saba[2], Marcio L.V. Araújo[3]
[1]Federal Institute of Bahia, Coordination of Natural Sciences and Mathematics; Simões Filho, Bahia; [2]Department of Sciences Exact and Earth Sciences, State University of Bahia—UNEB; [3]Center for Applied Research and Innovation (NPAI); Salvador, Bahia, Brazil

This study investigates the feasibility technical, economic and regulatory aspects of the introduction of biomethane in the headquarters energy of the state of Bahia, focusing in the distributor initiatives Bahiagás. The main objective is to assess whether the potential agricultural sector of the state estimated in more than 500 million Nm³/ year of biogas can be effectively converted in biomethane injectable in the natural gas network, considering you frames regulatory national and so-called public launched by the company. For this purpose, a revision systematics of literature scientific (Scielo, ScienceDirect, Scopus databases) and documents officers from the National Agency of Petroleum, Natural Gas and Biofuels (ANP), the Brazilian Association of Biogas and Biomethane (ABIOGÁS), the Ministry of Agriculture (MAPA), the Energy Research Company (EPE) and the companies themselves. Bahiagás notices (2022 and 2024). They were included only data with sources reliable, published between 2017 and 2025, with relevance direct to the context Brazilian and, preferably, to the Northeast region. The results point out that, although biomethane it is technically viable and have support normative robust (ANP Resolutions 886/2022 and 906/2022) and incentives financial via CBIOs (RenovaBio Law), the state of Bahia still no it has none unit producer operational according to ANP. The two calls Bahiagás public especially that of 2024, with a 10 - year contract and supply minimum of 5,000 m³/ day from 2027 onwards reveal a strong institutional interest, but also expose critical gaps: high investment costs (>R$ 15 million per average plant), absence of policies state support, logistics deficient waste collection and low training technique. The main conclusion is that, despite the enormous potential and conditions favorable, the implementation of biomethane in Bahia faces barriers institutional and structural that will beyond technology. To overcome them, it is essential to create a program state development, with lines of credit, assistance technique, centers collection regions. Without these measures, the 2027 commitment is at high risk of not being met.

Keywords: Bahiagás. Biomethane. Public Calls. Energy Policy. Energy Transition.

The energy transition to a sustainable and low-carbon matrix represents a major energy challenge for the 21st century. In this scenario, biomethane emerges as a relevant option with the capacity to replace, even partially, natural gas of fossil origin in several commercial, industrial and residential applications [1].

Biomethane can be obtained through the biogas purification process, increasing the percentage of methane (CH_4) to values close to that of natural gas sold by companies in the sector in their distribution networks or on road transport (Figure 1).

Received on 24 June 2026; revised 23 September 2026.
Address for correspondence: Paulo Roberto dos Santos. Via Universitária, s/n (R. Vital Brasil, 1394–1908), Pitanguinha, Simões Filho – BA, Brazil. ZIP code: 43700-000. E-mail: paulo.santos@ifba.edu.br.

J Bioeng. Tech. Health 2026;9(10):1047-1052
© 2026 by SENAI CIMATEC University. All rights reserved.

By inserting biomethane into the natural gas network, existing infrastructure can be used for distribution to end consumers [1]. The combustion of biomethane can be seen in Figure 2.

In Brazil, there are currently approximately 12 authorized biomethane producers, most of which are located in the Southeast and South regions of the country. In the Brazilian Northeast, only the state of Ceará has a biomethane production unit, according to the National Agency of Petroleum, Natural Gas and Biofuels (ANP) [2]. The current distribution is as follows: São Paulo (5 units), Rio de Janeiro (2 units), and the states of Mato Grosso do Sul, Minas Gerais, and Ceará with one unit each [2]. Biomethane production in 2025 has already exceeded 47 million Nm³, while in the whole of 2020 it did not exceed 40 million Nm³, demonstrating a significant increase in Brazilian production [2].

Figure 1. Process simplified biomethane insertion in the piped natural gas network.

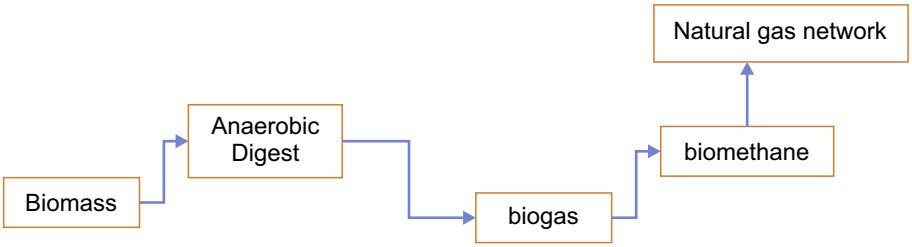

Figure 2. Flame of biomethane burning in the laboratory.



In the state of Bahia, which has enormous potential for biomethane production, due to its thriving agricultural sector and large urban centers such as Salvador and Feira de Santana with controlled landfills, there is still no large processing unit, but there is great potential for production [3].

According to the Brazilian Association of Biogas and Biomethane (ABIOGÁS), in the agricultural sector alone, the state has a production potential of over 500 million Nm^3/year of biogas [3]. A large portion of this biogas volume can be processed into biomethane, thus increasing its added value. The ANP (National Agency for the Promotion of Biomethane) is the federal government agency that regulates the sector; it has identified that in recent years, some states in the federation have taken the initiative to create laws that make biomethane more attractive, such as Mato Grosso do Sul, which supports projects in the production of biomethane with waste from ethanol production [3]. In 2022, the ANP issued two resolutions specifying biomethane's origin: Table 1 shows other sector resolutions.

- ANP Resolution No. 886/2022: Establishes the specifications and rules for approval of quality control of biomethane from landfills and sewage treatment plants intended for vehicular use and residential, industrial and commercial installations, to be marketed in the national territory [4].

- ANP Resolution No. 906/2022: Provides for the specifications of biomethane from agrosilvopastoral and commercial organic products and waste intended for vehicular use and residential and commercial installations to be marketed throughout the national territory [5].

Bahia Gas Company (Bahiagás), a mixed-capital company with the state government as the majority shareholder, is responsible for ensuring the distribution of natural gas in the Camaçari Petrochemical Complex and the Aratu Industrial Center [6]. In recent years, it has expanded its natural gas distribution potential, reaching the commercial, residential, automotive, and

Table 1. The main standards and resolutions on biomethane in Brazil.

Standard / Resolution	Organ Issuer	Year	Scope	Applicability
Resolution No. 886	ANP	2022	Biomethane specification from landfills toilets and ETEs	Vehicle, commercial, residential and industrial use
Resolution No. 906	ANP	2022	Biomethane specification originating from waste agrosilvopast oral and commercial	Vehicle, commercial, residential and industrial use
Resolution No. 685	ANP	2017	Authorization to commercializ e biomethane	Producers and distributors
Resolution No. 734	ANP	2018	Transportatio n rules biomethane road	Carriers bus stations
Law No. 13,576 (RenovaBio)	Federal Government	2017	National Biofuels Policy	Biomethane and CBIO producers

thermoelectric segments. Recent public calls for proposals in 2022 and 2024 demonstrate interest in expanding its network with biomethane. In 2022, a commercial proposal was launched for those interested in selling biomethane to the company, as well as projects for biomethane production. However, this public call was concluded without hiring any interested parties, on the grounds that the presented projects needed improvement.

Biomethane Public Call No. 01/2024, with supply scheduled to begin in 2027, a minimum supply of 5,000 cubic meters per day, and a ten-year contract. The published notices represent an important milestone for the sector, establishing clear marketing mechanisms, specific technical requirements, and contractual conditions that provide security for investors and developers of biomethane projects [7,8].

Materials and Methods

A decision was adopted approach qualitative and descriptive, based in revision systematic literature and documentary analysis. They were consulted you following databases and sources officials: Banks academics: Scielo, ScienceDirect and Scopus for articles scientists indexed. Government and institutional sources: National Agency of Petroleum, Natural Gas and Biofuels (ANP): resolutions, production reports and authorizations; Brazilian Association of Biogas and Biomethane (ABIOGÁS); diagnostics sectoral and statistical data; Ministry of Agriculture, Livestock and Supply (MAPA): waste inventories agricultural; Energy Research Company (EPE): reports on Energy and biofuels: Government of the State of Bahia: State Sustainable Energy Plan 2023-2030; Bahiagás: call for proposals public (2022 and 2024). The Inclusion criteria They were selected just you materials that served everyone you following criteria:

- Relevance direct: themes related to production, purification, injection, marketing or biomethane policy in Brazil;
- Frequency: published between 2017 (launch of the RenovaBio Law) and 2025;
- Reliability: origin in institutions recognized (governmental, academic) or research), with methodology clear and verifiable data;
- Geographical specificity: priority for data referring to the North East or to Bahia;
- Quantification: presence of values numerical (potentials, costs, emissions, volumes).

Results and Discussion

The results display important information found in the scientific materials researched, as well as on government websites.

Brazil holds great potential for biogas and biomethane production, estimated at 84.6 billion Nm^3/year and 44.7 billion Nm^3/year, respectively, with current production being around 1.5 to 2% of this value [3,7]. Most of the raw material for biogas comes from agricultural and urban waste, with a focus on agriculture in the Northeast [8,9]. The injection of biomethane into the natural gas network, already implemented in Ceará, has demonstrated technical feasibility and compatibility with the infrastructure of the local distributor (CEGÁS), including regulatory approval by the ANP [10]. Currently, biomethane represents approximately 15% of the company's distribution volume, positioning CEGÁS as reference national in solutions energetics sustainable [10]. Biogas purification must ensure strict control of impurities, such as siloxanes, volatile organic compounds, and metals, to meet the specifications defined by ANP Resolutions No. 886/2022 and 906/2022 [4,5]. The biomethane produced has an average calorific value of approximately 36 MJ/m^3, comparable to fossil natural gas, allowing its direct use in various applications [11-13].

Despite the promising outlook, the sector faces challenges such as high initial costs for purification plants, a lack of specific incentive policies, and the need to refine projects to meet the technical and financial requirements of public tenders [1,4]. Bahiagás's 2024 public tender provides for a 10-year supply contract for at least 5,000 m^3/day starting in 2027, representing a significant regulatory and commercial advance for the state. This was the second public tender, and the 2022 tender did not result in a contract [6]. Bahia has the potential to become a regional biomethane hub, given its agricultural vocation, but it requires coordination between public and private agents, as well as more robust state policies to encourage investment, technical training, and environmental certification [3,15]. The economic outlook for biomethane production depends directly on the scale of the project, the cost of collecting the raw material, the efficiency of the purification process, and the sales price guaranteed by long-term contracts. Studies indicate that medium and large plants (above 1,000 Nm^3/h of biomethane) can achieve competitiveness with fossil natural gas when carbon credits and tax incentives are used [16]. In Brazil, the Emissions Reduction Certificates (CBIOs) system, created by the RenovaBio Law (Law No. 13,576/2017), allows Biomethane producers can generate additional revenue from the sale of these certificates, improving project profitability [15]. Furthermore, partnership models between agricultural cooperatives and companies specializing in biogas engineering show promise, especially in regions with high concentrations of organic waste, such as the semi-arid region of Bahia [16,17]. Biomethane transportation and distribution infrastructure is still limited in Brazil, especially outside of large urban centers. In remote areas, such as the interior of Bahia, cryogenic (Liquefied Biomethane LBM) or high-pressure (Compressed Natural Gas CNG) truck transportation can be an alternative, but significantly increases operating costs [18]. Although direct injection into the natural gas network is a more efficient option, its viability depends on the production unit's proximity to the distribution network [19]. ANP Resolution No. 734/2018 establishes rules for the road transportation of biomethane, but there are still gaps in equipment standardization and operational safety. Investments in regasification terminals and regionalized supply centers can expand access to biomethane in areas not served by the pipeline network [20,21]. Biomethane production brings environmental benefits, such as reducing methane emissions from anaerobic waste loss and reducing the use of fossil fuels. Studies estimate that each Nm^3 of biomethane avoids between 1.8 and 2.5 kg of CO_2 equivalent when it replaces fossil natural gas [21]. Furthermore, the process generates biofertilizer as a byproduct, which can be used in agriculture, reducing dependence on synthetic

fertilizers and improving soil quality [22]. From a socioeconomic perspective, the biomethane chain can generate direct and indirect jobs in rural areas. Formalizing local cooperatives and training rural workers are essential strategies to ensure that the benefits are distributed equitably [23].

Conclusion

Biomethane represents a renewable energy solution with high potential for Bahia and Brazil. Large-scale production and injection into the natural gas grid are feasible, but depend on overcoming technical, economic, and regulatory barriers. Market expansion requires greater integration among industry players, regulatory alignment, and effective public policies that encourage the production, commercialization, and use of biomethane. Bahia, with its vast potential, is positioned to play a leading role in this energy transition.

This study confirmed that Bahia has all conditions natural, regulatory, and market requirements to become a national biomethane hub. The potential is real, the standards they are adequate, and Bahiagás' demand is clear. However, the absence of projects approved same after two calls public reveals one deep flaw in governance energetics state. Analysis of points raised in the search:

- Potential Technical-economic: Yes, it is viable, but only for medium / large projects. size with access to CBIOs and long- term contracts term.
- Policy adequacy nationals: They are adequate, but not they are translated in actions places.
- Barriers identified: High costs, logistics deficient, lack of training and absence of incentives state they are you main obstacles.
- Solutions proposals: A program state integrated is urgent.

The problem it is not technological nor resources. It is institutional. No there is an organ single in Bahia responsible put coordinate, guide and finance biomethane projects. Bahiagás is a distributor, not promoter. The ANP regulates, but does not help in an appropriate way because only regulates the sector. MAPA has data, but does not operate efficiently in the state. Biomethane in Bahia is arrested in a vacuum institutional. In view of this scenario we did some recommendations practices to overcome limitations.

- High investment cost: a biomethane investment fund could be created with the state and federal government through BNDES.
- Fragmented logistics: creation of 3 or 5 collection centers in cities with Vitória da Conquista and Feira de Santana.
- Low training: partnerships with universities and institutes federal.

Acknowledgments

To everyone who contributed directly and indirectly to this work.

References

1. International Energy Agency (IEA). Methane tracker 2023: biogas and biomethane. Paris: IEA; 2023.
2. National Agency of Petroleum, Natural Gas and Biofuels (ANP). Report on biomethane production in Brazil. Brasília: ANP; 2025.
3. Association of Biogas and Biomethane (ABIOGÁS). Biogas and biomethane potential in Brazil: sectorial diagnosis 2024. Brasília: ABIOGÁS; 2024.
4. National Agency of Petroleum, Natural Gas and Biofuels (ANP). ANP Resolution No. 886, of December 16, 2022: establishes biomethane specifications from sanitary landfills and wastewater treatment plants. Diário Oficial da União. 2022 Dec 19; Seção 1.
5. National Agency of Petroleum, Natural Gas and Biofuels (ANP). ANP Resolution No. 906, of December 23, 2022: biomethane specifications originating from agrosilvopastoral waste. Diário Oficial da União. 2022 Dec 26; Seção 1.
6. Bahiagás. Public Call for Biomethane No. 01/2024. Salvador: Bahiagás; 2024.
7. Biogas and biomethane production in Brazil: potential, policies and challenges. Renew Sustain Energy Rev. 2020;134:110316.
8. DM, et al. Potential for biogas production from livestock waste in Northeastern Brazil. J Clean Prod. 2022;331:130001.

9. Ministry of Agriculture, Livestock and Food Supply (MAPA). Agricultural waste and energy: perspectives for biomethane. Brasília: MAPA; 2023.
10. Cegás. Cegás presents pioneering experience with biomethane at national workshop on energy transition [Internet]. Available from: https://www.cegas.com.br/cegas-present-experiencia-pioneira-com-biometano-em-workshop-nacional-sobre-transicao-energetica/
11. Oliveira PV, Santos LM, Costa EF. Characterization of biomethane energy produced from anaerobic digestion. Sustainable Energy. 2022;10(3):112-125.
12. Sehnem S, et al. Barriers to the development of biomethane in Brazil: a multisectoral analysis. Energy Policy. 2021;158:112543.
13. Government of Bahia. State energy plan for sustainable development 2023-2030. Salvador: Secretariat of Economic Development; 2023.
14. Luz FC, et al. Economic viability of biomethane production in Brazil. Renew Energy. 2020;148:1039-1050.
15. National Agency of Petroleum, Natural Gas and Biofuels (ANP). CBIO market: annual report 2023. Brasília: ANP; 2024.
16. Almeida CM, et al. Cooperatives in the biogas chain: social and economic impacts on rural development in Brazil. Energy Sustain Dev. 2022;69:1-10.
17. Energy Research Company (EPE). National Energy Plan 2030 [Internet]. Available from: https://www.epe.gov.br
18. Brazilian Association of Piped Gas Distribution Companies (ABEGÁS). Biomethane transportation by CNG: technical study. São Paulo: ABEGÁS; 2023.
19. Bastos R, et al. Decentralized distribution of biomethane production in Brazil. J Nat Gas Sci Eng. 2023;110:104432.
20. K, et al. Quality of digestates from biogas plants and their potential as fertilizers. Waste Manag. 2022;140:1-15.
21. United Nations Development Programme (UNDP). Biomethane and sustainable development in Brazil. Brasília: UNDP; 2023.
22. Brazilian Institute of Geography and Statistics (IBGE). Rural labor statistics in the Northeast. Rio de Janeiro: IBGE; 2023.
23. Intergovernmental Panel on Climate Change (IPCC). Climate change 2023: mitigation of climate change. Geneva: IPCC; 2023.

Instructions for Authors

The Authors must indicate in a cover letter the address, telephone number and e-mail of the corresponding author. The corresponding author will be asked to make a statement confirming that the content of the manuscript represents the views of the co-authors, that neither the corresponding author nor the co-authors have submitted duplicate or overlapping manuscripts elsewhere, and that the items indicated as personal communications in the text are supported by the referenced person. Also, the protocol letter with the number should be included in the submission article, as well as the name of sponsors (if applicable).

Manuscripts may be submitted within designated categories of communication, including:

- Original basic or clinical investigation (original articles on topics of broad interest in the field of bioengineering and biotechnology applied to health). We particularly welcome papers that discuss epidemiological aspects of international health, clinical reports, clinical trials and reports of laboratory investigations.
- Case presentation and discussion (case reports must be carefully documented and must be of importance because they illustrate or describe unusual features or have important practice implications).
- Brief reports of new methods or observations (short communications brief reports of unusual or preliminary findings).
- State-of-the-art presentations (reviews on protocols of importance to readers in diverse geographic areas. These should be comprehensive and fully referenced).
- Review articles (reviews on topics of importance with a new approach in the discussion). However, review articles only will be accepted after an invitation of the Editors.
- Letters to the editor or editorials concerning previous publications (correspondence relating to papers recently published in the Journal, or containing brief reports of unusual or preliminary findings).
- Editor's corner, containing ideas, hypotheses and comments (papers that advance a hypothesis or represent an opinion relating to a topic of current interest).
- Innovative medical products (description of new biotechnology and innovative products applied to health).
- Health innovation initiatives articles (innovative articles of technological production in Brazil and worldwide, national policies and directives related to technology applied to health in our country and abroad).

The authors should checklist comparing the text with the template of the Journal.

Supplements to the JBTH include articles under a unifying theme, such as those summarizing presentations of symposia or focusing on a specific subject. These will be added to the regular publication of the Journal as appropriate, and will be peer reviewed in the same manner as submitted manuscripts.

Statement of Editorial Policy

The editors of the Journal reserve the right to edit manuscripts for clarity, grammar and style. Authors will have an opportunity to review these changes prior to creation of galley proofs. Changes in content after galley proofs will be sent for reviewing and could be required charges to the author. The JBTH does not accept articles which duplicate or overlap publications elsewhere.

Peer-Review Process

All manuscripts are assigned to an Associate Editor by the Editor-in-Chief and Deputy Editor, and sent to outside experts for peer review. The Associate Editor, aided by the reviewers' comments, makes a recommendation to the Editor-in-Chief regarding the merits of the manuscript. The Editor-in-Chief makes a final decision to accept, reject, or request revision of the manuscript. A request for revision does not guarantee ultimate acceptance of the revised manuscript.

Manuscripts may also be sent out for statistical review ou *ad hoc* reviewers. The average time from submission to first decision is three weeks.

Revisions

Manuscripts that are sent back to authors for revision must be returned to the editorial office by 15 days after the date of the revision request. Unless the decision letter specifically indicates otherwise, it is important not to increase the text length of the manuscript in responding to the comments. The cover letter must include a point-by-point response to the reviewers and Editors comments, and should indicate any additional changes made. Any alteration in authorship, including a change in order of authors, must be agreed upon by all authors, and a statement signed by all authors must be submitted to the editorial office.

Style

Manuscripts may be submitted only in electronic form by www.jbth.com.br. Each manuscript will be assigned a registration number, and the author notified that the manuscript is complete and appropriate to begin the review process. The submission file is in OpenOffice, Microsoft Word, or RTF document file format for texts and JPG (300dpi) for figures.

Authors must indicate in a cover letter the address, telephone number, fax number, and e-mail of the corresponding author. The corresponding author will be asked to make a statement confirming that the content of the manuscript represents the views of the co-authors, that neither the corresponding author nor the co-authors have submitted duplicate or overlapping manuscripts elsewhere, and that the items indicated as personal communications in the text are supported by the referenced person.

Manuscripts are to be typed as indicated in Guide for Authors, as well as text, tables, references, legends. All pages are to be numbered with the order of presentation as follows: title page, abstract, text, acknowledgements, references, tables, figure legends and figures. A running title of not more than 40 characters should be at the top of each page. References should be listed consecutively in the text and recorded as follows in the reference list, and must follow the format of the National Library of Medicine as in Index Medicus and "Uniform Requirements for Manuscripts Submitted to Biomedical Journals" or in "Vancouver Citation Style". Titles of journals not listed in Index Medicus should be spelled out in full.

Manuscript style will follow accepted standards. Please refer to the JBTH for guidance. The final style will be determined by the Editor-in-Chief as reviewed and accepted by the manuscript's corresponding author.

Approval of the Ethics Committee

The JBTH will only accept articles that are approved by the ethics committees of the respective institutions (protocol number and/or approval certification should be sent after the references). The protocol number should be included in the end of the Introduction section of the article.

Publication Ethics

Authors should observe high standards with respect to publication ethics as set out by the International Committee of Medical Journal Editors (ICMJE). Falsification or fabrication of data, plagiarism, including duplicate publication of the authors' own work without proper citation, and misappropriation of the work are all unacceptable practices. Any cases of ethical misconduct are treated very seriously and will be dealt with in accordance with the JBTH guidelines.

Conflicts of Interest

At the point of submission, each author should reveal any financial interests or connections, direct or indirect, or other situations that might raise the question of bias in the work reported or the conclusions, implications, or opinions stated - including pertinent commercial or other sources of funding for the individual author(s) or for the associated department(s) or organizations(s), and personal relationships. There is a potential conflict of interest when anyone involved in the publication process has a financial or other beneficial interest in

the products or concepts mentioned in a submitted manuscript or in competing products that might bias his or her judgment.

Material Disclaimer

The opinions expressed in JBTH are those of the authors and contributors, and do not necessarily reflect those of the SENAI CIMATEC, the editors, the editorial board, or the organization with which the authors are affiliated.

Privacy Statement

The names and email addresses entered in this Journal site will be used exclusively for the stated purposes of this journal and will not be made available for any other purpose or to any other party.

Brief Policies of Style

Manuscript	Original	Review	Birief Comunication	Case Report	Editorial ; Letter to the Editor; Editor' s Corner	Innovative Medical Products	State-of-the-Art	Health Innovation Initiatives
Font Type	Times or Arial	Times or Arial	Times or Arial	Times or Arial	Times or Arial	Times or Arial	Times or Arial	Times or Arial
Number of Words – Title	120	90	95	85	70	60	120	90
Font Size/Space-Title	12; double space	12; double space	12; double space	12; double space	12; double space	12; double space	12; double space	12; double space
Font Size/Space-Abstracts/Key Words and Abbreviations	10; single space	10; single space	10; single space	10; single space	-	-	10; single space	10; single space
Number of Words – Abstracts/Key Words	300/5	300/5	200/5	250/5	-	-	300/5	300/5
Font Size/Space-Text	12; Double space	12; Double space	12; Double space	12; Double space	12; Double space	12; Double space	12; Double space	12; Double space
Number of Words – Text	5,000 including spaces	5,500 including spaces	2,500 including spaces	1,000 including spaces	1,000 including spaces	550 including spaces	5,000 including spaces	5,500 including spaces
Number of Figures	8 (title font size 12, double space)	3 (title font size 12, double space)	2 (title font size 12, double space)	2 (title font size 12, double space)	-	2 (title font size 12, double space)	8 (title font size 12, double space)	8 (title font size 12, double space)
Number of Tables/Graphic	7 title font size 12, double space	2 title font size 12, double space	2(title font size 12, double space)	1(title font size 12, double space)	-	-	7 title font size 12, double space	4 title font size 12, double space
Number of Authors and Co-authors*	15	10	5	10	3	3	15	10
References	20 (font size 10,single space	30(font size 10,single space	15 (font size 10,single space)	10 (font size 10,single space)	10 (font size 10,single space	5(font size 10,single space	20 (font size 10,single space	20

*First and last name with a sequencing overwritten number. Corresponding author(s) should be identified with an asterisk; Type 10, Times or Arial, single space. Running title of not more than 40 characters should be at the top of each page. References should be listed consecutively in the text. References must be cited on (not above) the line of text and in brackets instead of parentheses, e.g., [7,8]. References must be numbered in the order in which they appear in the text. References not cited in the text cannot appear in the reference section. References only or first cited in a table or figures are numbered according to where the table or figure is cited in the text. For instance, if a table is placed after reference 8, a new reference cited in table 1 would be reference 9.1 would be reference 9.

Checklist for Submitted Manuscripts

❑1. Please provide a cover letter with your submission specifying the corresponding author as well as an address, telephone number and e-mail.

❑2. Submit your paper using our website www.jbth.com.br. Use Word Perfect/Word for Windows, each with a complete set of original illustrations.

❑3. The entire manuscript (including tables and references) must be typed according to the guidelines instructions.

❑4. The order of appearance of material in all manuscripts should be as follows: title page, abstract, text, acknowledgements, references, tables, figures/graphics/diagrams with the respective legends.

❑5. The title page must include a title of not more than three printed lines (please check the guidelines of each specific manuscript), authors (no titles or degrees), institutional affiliations, a running headline of not more than 40 letters with spaces.

❑6. Acknowledgements of persons who assisted the authors should be included on the page preceding the references.

❑7. References must begin on a separate page.

❑8. References must be cited on (not above) the line of text and in brackets instead of parentheses, e.g., [7,8].

❑9. References must be numbered in the order in which they appear in the text. References not cited in the text cannot appear in the reference section. References only or first cited in a table or figures are numbered according to where the table or figure is cited in the text. For instance, if a table is placed after reference 8, a new reference cited in table 1 would be reference 9.

❑10. Reference citations must follow the format established by the "Uniform Requirements for Manuscripts Submitted to Biomedical Journals" or in "Vancouver Citation Style".

❑11. If you reference your own unpublished work (i.e., an "in press" article) in the manuscript that you are submitting, you must attach a file of the "in press" article and an acceptance letter from the journal.

❑12. If you cite unpublished data that are not your own, you must provide a letter of permission from the author of that publication.

❑13. Please provide each figure in high quality (minimum 300 dpi: JPG or TIF). Figure must be on a separate file.

❑14. If the study received a financial support, the name of the sponsors must be included in the cover letter and in the text, after the author's affiliations.

❑15. Provide the number of the Ethics Committees (please check the guidelines for authors).